JETP Letters, Vol. 75, No. 9, 2002, pp. 441–444. Translated from Pis'ma v Zhurnal Éksperimental'noĭ i Teoreticheskoĭ Fiziki, Vol. 75, No. 9, 2002, pp. 531–534.

Photoproduction of Neutrinos on Nuclei in a Strong Magnetic Field

A. V. Kuznetsov* and N. V. Mikheev

Yaroslavl State University, ul. Sovetskaya 14, Yaroslavl, 150000 Russia

** e-mail: avkuzn@uniyar.ac.ru*

Received March 6, 2002

The photoproduction of a neutrino pair on a nucleus, $\gamma + Ze \longrightarrow Ze + \gamma + \nu + \bar{\nu}$, is investigated in a strong magnetic field. It is shown that taking account of the photon dispersion in a strong field reduces appreciably the catalyzing effect of the latter on the process. Therefore, at any field magnitude, neutrino photoproduction cannot compete with the Urca processes. This conclusion contradicts a recent statement in the literature. © *2002 MAIK "Nauka/Interperiodica".*

PACS numbers: 25.20.Lj; 13.10.+q; 13.15.+g; 95.30.Cq

Strong magnetic fields arising in astrophysical cataclysms such as supernova explosions or a coalescence of neutron stars have an active effect on the quantum processes by opening or considerably enhancing reactions which are kinematically forbidden or strongly suppressed in vacuum. However, this field effect is substantial only when the field is sufficiently strong. The so-called critical or Schwinger value $B_e = m_e^2/e \simeq 4.41 \times 10^{13}$ G serves as the natural scale of magnetic field intensity.[1] There are grounds to expect that fields on this and even larger scale can arise in astrophysical objects. For example, there is a class of stars, so-called magnetars, which are neutron stars with magnetic fields of $\sim 4 \times 10^{14}$ G [1, 2]. The models of astrophysical processes and objects with magnetic fields up to 10^{17}–10^{18} G are discussed in [3–6]. Thus, the physics of quantum processes in strong external fields is an interesting and important direction of investigations both from the fundamental viewpoint and in the light of possible astrophysical applications.

Of special interest are the loop quantum processes whose initial and final states involve only electrically neutral particles such as neutrinos and photons. The action of an external field on these processes is caused, first, by the sensitivity of charged virtual fermions to the field. In this case, an electron as a particle with the maximum specific charge e/m_e plays the dominant role. Second, a strong magnetic field gives rise to a considerable change in the dispersion properties of photons and, therefore, in their kinematics.

In recent work [7], the contribution of the loop process of neutrino-pair photoproduction on a nucleus

$$\gamma + Ze \longrightarrow Ze + \gamma + \nu + \bar{\nu} \qquad (1)$$

in a strong external magnetic field to the cooling of stars was studied and it was concluded that this contribution can compete with the contribution from Urca processes. Therefore, process (1), as one more channel of neutrino energy loss, would be taken into account when describing the cooling of strongly magnetized neutron stars.

In this paper, we reexamine the neutrino pair photoproduction on a nucleus and demonstrate that the catalyzing effect of a strong magnetic field on process (1) decreases considerably if the photon dispersion in the field is taken into account. Since this effect was ignored in [7], the contribution of the loop process was overestimated by many orders of magnitude.

The amplitude of neutrino pair photoproduction on a nucleus, Eq. (1), can be derived from the amplitude of interaction between three photons and a neutrino pair, e.g.,

$$\gamma + \gamma + \gamma \longrightarrow \nu + \bar{\nu}, \qquad (2)$$

whose Feynman diagram is shown in Fig. 1. As is known (see, e.g., [8]), three-photon processes (2) in a strong magnetic field are more intense than the corresponding two-photon processes, because the amplitude

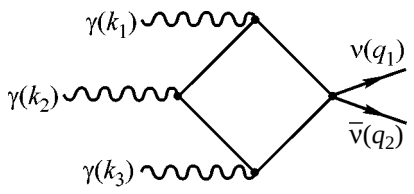

Fig. 1. Feynman diagram for the $\gamma + \gamma + \gamma \longrightarrow \nu + \bar{\nu}$ process.

[1] We use the natural system of units $c = \hbar = 1$, and $e > 0$ is the elementary charge.

of processes (2) with the vector-axial neutrino current increases linearly with the field, whereas the amplitude of the $\gamma\gamma \longrightarrow \nu\bar{\nu}$ processes with such a neutrino current is independent of the field. In [9], we analyzed the nonstandard case of effective scalar neutrino current in the $\gamma\gamma \longrightarrow \nu\bar{\nu}$ process, where the amplitude also increases linearly with the field.

The amplitude of process (2) in a strong magnetic field can be represented in the covariant form [8]

$$\mathcal{M} = -\frac{8e^3 G_F eBm_e^2}{\sqrt{2}\pi^2}(\varepsilon_1\tilde{\varphi}k_1)(\varepsilon_2\tilde{\varphi}k_2)(\varepsilon_3\tilde{\varphi}k_3) \times [C_V(j\tilde{\varphi}k_4) + C_A(j\tilde{\varphi}\tilde{\varphi}k_4)]I(k_1, k_2, k_3). \quad (3)$$

Here, $C_V = \pm 1/2 + 2\sin^2\theta_W$ and $C_A = \pm 1/2$ are the vector and axial constants of the effective $\nu\nu ee$ Lagrangian, respectively (the upper signs correspond to electron neutrino and the lower signs correspond to muon and tan neutrinos); $\varepsilon_{1,2,3}$ and $k_{1,2,3}$ are the polarization 4-vectors and photon 4-momenta, respectively; $j_\alpha = [\bar{\nu}(q_1)\gamma_\alpha(1+\gamma_5)\nu(-q_2)]$ is the Fourier transform of the neutrino current; $k_4 = q_1 + q_2$ is the 4-momentum of a neutrino pair; $\tilde{\varphi}_{\alpha\beta} = \tilde{F}_{\alpha\beta}/B$ is the dimensionless dual tensor of the external magnetic field, where $\tilde{F}_{\alpha\beta} = \frac{1}{2}\varepsilon_{\alpha\beta\mu\nu}F_{\mu\nu}$; and the tensor subscripts of 4-vectors and tensors in the parentheses are supposed to be sequentially contracted, e.g., $(a\tilde{\varphi}b) = a_\alpha\tilde{\varphi}_{\alpha\beta}b_\beta$.

The form factor $I(k_1, k_2, k_3)$ has the form of the following triple integral with respect to the Feynman variables:

$$I(k_1, k_2, k_3) = \frac{1}{D}\int_0^1 dx\int_0^x dy\int_0^y dz \times\left\{\frac{a(k_1, k_2, k_3)}{[m_e^2 - b(k_1, k_2, k_3)]^3} + \{k_1 \longleftrightarrow k_2\} + \{k_2 \longleftrightarrow k_3\}\right\}. \quad (4)$$

Here,

$$D = k_1^2(k_2k_3) + k_2^2(k_1k_3) + k_3^2(k_1k_2) + 2(k_1k_2)(k_1k_3) + 2(k_1k_2)(k_2k_3) + 2(k_1k_3)(k_2k_3), \quad (5)$$

$$a(k_1, k_2, k_3) = k_1^2(1-x)^2 - k_2^2y(1-y) + k_3^2z^2 + (k_1k_2)(1-2x)(1-y) + (k_1k_3)[1-x-z(1-2x)] - (k_2k_3)y(1-2z), \quad (6)$$

$$b(k_1, k_2, k_3) = k_1^2x(1-x) + k_2^2y(1-y) + k_3^2z(1-z) + 2(k_1k_2)(1-x)y + 2(k_1k_3)(1-x)z + 2(k_2k_3)(1-y)z, \quad (7)$$

where the scalar products (k_ik_j) are the contractions $(k_i\tilde{\varphi}\tilde{\varphi}k_j)$.

For low photon energies, i.e., for $\omega_{1,2,3} \ll m_e$, integral (4) is easily calculated to give

$$I(k_1, k_2, k_3) \simeq \frac{1}{60m_e^8}. \quad (8)$$

In this case, amplitude (3), in view of Eq. (8), corresponds to the effective local $\gamma\gamma\gamma\nu\bar{\nu}$ Lagrangian

$$\mathcal{L}_{\text{eff}} = -\frac{e^3 G_F eB}{45\sqrt{2}\pi^2 m_e^6}\left(\frac{\partial A^\alpha}{\partial x_\beta}\tilde{\varphi}_{\alpha\beta}\right)^3 \times\frac{\partial}{\partial x_\sigma}[\bar{\nu}\gamma^\rho(1+\gamma_5)\nu][C_V\tilde{\varphi}_{\rho\sigma} + C_A(\tilde{\varphi}\tilde{\varphi})_{\rho\sigma}]. \quad (9)$$

The $\gamma\gamma\gamma\nu\bar{\nu}$ interaction at low energies was previously studied in [8], where the Lagrangian was overestimated by a factor of two.

An analysis of the dimensionality of amplitude (3) for the limiting values of the characteristic photon energy $|k_1| \sim |k_2| \sim |k_3| \sim \omega$ indicates that the amplitude increases as $\sim\omega^5$ at low energies and decreases as $\sim\omega^{-3}$ at high energies.

When calculating the amplitude of process (1) on a nucleus in the local limit of effective $\gamma\gamma\gamma\nu\bar{\nu}$ interaction (9), it is necessary to take into account the effect of strong magnetic field on the dispersion properties of real and virtual photons. We will demonstrate that this effect is of crucial importance. We recall that process (1) in a strong magnetic field involves photons of only one of the two possible polarizations. According to Adler [10], this polarization is "transverse."

For a virtual photon, it is necessary to use, instead of the vacuum propagator $\sim q^{-2}$, the propagator including vacuum polarization in a magnetic field:

$$D^{(B)}(q_\parallel^2, q_\perp^2) = \frac{1}{q^2 - P(q_\parallel^2)}, \quad (10)$$

where, $q_\parallel^2 = q_0^2 - q_z^2$, $q_\perp^2 = q_x^2 + q_y^2$, $q^2 = q_\parallel^2 - q_\perp^2$ (the magnetic field is directed along the z axis), and $P(q_\parallel^2)$ is the photon polarization operator in the field. For the strong field $B \gg B_e$ and in the approximation $|q_\parallel^2| \ll m_e^2$, this operator takes the simple form [11]

$$P(q_\parallel^2) \simeq -\frac{\alpha}{3\pi}\frac{B}{B_e}q_\parallel^2. \quad (11)$$

It is convenient to introduce the following dimensionless parameter that specifies the field effect in all subsequent expressions:

$$\beta = \frac{\alpha}{3\pi}\frac{B}{B_e}. \quad (12)$$

The parameter β is equal to 0.77 and 7.7 for fields $10^3 B_e$ and $10^4 B_e$, respectively; i.e., it is not small. Taking into account Eqs. (11) and (12) and that $q_0 = 0$ for the virtual photon connected with a fixed nucleus, we can represent propagator (10) in the form

$$D^{(B)} \simeq -\frac{1}{q_\perp^2 + (1+\beta)q_z^2}. \quad (13)$$

At the same time, the strong magnetic field also acts on the real photons involved in process (1) and, hence, renormalizes the wave functions:

$$\varepsilon_\alpha \longrightarrow \sqrt{\mathscr{L}}\varepsilon_\alpha. \quad (14)$$

In view of Eq. (11), the renormalization factor $\mathscr{L}$ takes the form

$$\mathscr{L} = \left(1 - \frac{dP(q_\parallel^2)}{dq_\parallel^2}\right)^{-1} = \frac{1}{1+\beta}. \quad (15)$$

In addition, the kinematic properties of photons change substantially. Taking into account Eqs. (11) and (12), one can represent the photon dispersion relation $k^2 - P(k_\parallel^2) = 0$ as $\omega^2 = \mathbf{k}^2(1 + \beta\cos^2\theta)/(1+\beta)$ and the element of the momentum space in the form

$$d^3k = (1+\beta)\omega^2 d\omega dy d\varphi,$$

$$y = \cos\theta\sqrt{1+\beta}/\sqrt{1+\beta\cos^2\theta},$$

where θ and φ are the polar and azimuthal angles, respectively.

Using effective Lagrangian (9), taking into account the effect of the magnetic field on photon properties (10)–(15), and substituting the polarization vectors of real photons

$$\varepsilon_\alpha^{(\perp)} = \frac{(\tilde{\varphi}k)_\alpha}{\sqrt{k_\parallel^2}}, \quad (16)$$

we represent the amplitude of process (1) in the form

$$\mathcal{M} = \frac{32\pi\alpha Z G_F}{5\sqrt{2}m_e^4}\frac{\beta}{1+\beta} \times \frac{2m_N q_z\sqrt{k_{1\parallel}^2 k_{2\parallel}^2}}{q_\perp^2 + (1+\beta)q_z^2}[C_V(j\tilde{\varphi}k_4) + C_A(j\tilde{\varphi}\tilde{\varphi}k_4)], \quad (17)$$

where m_N is the nuclear mass, q is the momentum transfer to the nucleus, and $q^\alpha = (0, \mathbf{q})$. This expression for the amplitude differs considerably from that obtained in [7], where the effect of a strong magnetic field on the dispersion properties of photons was ignored.

The energy carried away by neutrinos from the star volume unit per time unit is an important quantity in astrophysical applications. It is defined in terms of the amplitude of process (1) as

$$Q_\nu = \frac{(2\pi)^4 n_N}{2m_N}\int |\mathcal{M}|^2(\varepsilon_1 + \varepsilon_2) \times \delta^4(k_1 - k_2 - q_1 - q_2 - q)\frac{d^3k_1}{(2\pi)^3 2\omega_1} f(\omega_1) \quad (18)$$
$$\times \frac{d^3k_2}{(2\pi)^3 2\omega_2}[1 + f(\omega_2)]\frac{d^3q_1}{(2\pi)^3 2\varepsilon_1}\frac{d^3q_2}{(2\pi)^3 2\varepsilon_2}\frac{d^3q}{(2\pi)^3 2m_N},$$

where n_N is the nuclear concentration, ε_1 and ε_2 are the energies of neutrino and antineutrino, respectively, and $f(\omega) = [\exp(\omega/T) - 1]^{-1}$ is the distribution function for the equilibrium photon gas at temperature T.

Substitution of amplitude (17) into Eq. (18) leads to the following expression for the volume density of radiation power:

$$Q_\nu = \frac{8(2\pi)^9}{225}Z^2\alpha^2 G_F^2 m_e^6 n_N\left(\frac{T}{m_e}\right)^{14} J(\beta). \quad (19)$$

The dependence on field parameter (12) is determined by the integral

$$J(\beta) = \beta^2\int_{-1}^{1} du(1-u^2)\int_{-1}^{1} dv(1-v^2) \times \int_0^1 ds s^3(1-s)^8\int_0^1 dr r^2\int_{-1}^{1} dx[u - sv - (1-s)rx]^2 \times (1 - r^2x^2)[\overline{C_V^2}(1-r^2) + \overline{C_A^2}r^2(1-x^2)] \times \int_0^{2\pi}\frac{d\varphi_1}{2\pi}\int_0^{2\pi}\frac{d\varphi_2}{2\pi}\frac{1}{[F(\beta)]^2}, \quad (20)$$

where

$$F(\beta) = (1+\beta)\{1 - u^2 + s^2(1-v^2) - 2s\sqrt{1-u^2}\sqrt{1-v^2}\cos\varphi_1 + [u - sv - (1-s)rx]^2\} - 2\sqrt{1+\beta}(1-s)r\sqrt{1-x^2} \times [\sqrt{1-u^2}\cos\varphi_2 - s\sqrt{1-v^2}\cos(\varphi_2 - \varphi_1)] + (1-s^2)r^2(1-x^2), \quad (21)$$

and the constants $\overline{C_V^2} = 0.93$ and $\overline{C_A^2} = 0.75$ are obtained by summing over all neutrino production channels for the ν_e, ν_μ, and ν_τ neutrinos.

The numerically calculated integral (20) is shown in Fig. 2. It is seen that taking account of the effect of a strong magnetic field on photon dispersion changes fundamentally the dependence of the neutrino energy loss power on the field magnitude: the quadratic dependence gives way to a constant. Taking this behavior into

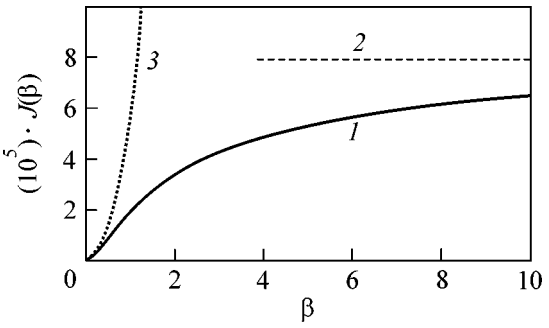

Fig. 2. (*1*) Function $J(\beta)$ [Eq. (20)] vs. field parameter β; (*2*) asymptotic behavior of $J(\beta) \longrightarrow 8 \times 10^{-5}$ at large β; (*3*) $\sim\beta^2$ dependence obtained disregarding the magnetic field effect on the photon dispersion.

account, we obtain an upper limit for Q_ν in the asymptotically strong field:

$$Q_\nu \lesssim 2.3 \times 10^{27} \left(\frac{T}{m_e}\right)^{14} \left\langle \frac{Z^2}{A} \right\rangle \left(\frac{\rho}{\rho_0}\right) \text{erg/(cm}^3\,\text{s)}, \quad (22)$$

where Z and A are the charge and mass numbers of the nucleus, the averaging goes over all nuclei, $\rho_0 = 2.8 \times 10^{14}$ g/cm^3 is the characteristic nuclear density, and ρ is the average density of the star. An analysis of Eq. (22) indicates that the conclusion made in [7] about the competition of process (1) with the Urca processes at magnetic fields $B \sim 10^3 B_e - 10^4 B_e$ is erroneous. The cause is that the large numerical factor arising in Eq. (19) and similar formulas in [7] originates from the integral with respect to the energy ω_1 ($x = \omega_1/T$) of the initial photon:

$$\int_0^\infty \frac{dx x^{13}}{e^x - 1} = 13!\zeta(14) = \frac{(2\pi)^{14}}{24} \simeq 6.2 \times 10^9. \quad (23)$$

The main contribution to integral (23) comes from $x \sim$ 10–20 (i.e., $\omega_1 \sim (10\text{–}20)T$). Therefore, since amplitude (17) of the process is obtained in the approximation $\omega \lesssim m_e$, the corresponding expression for the neutrino energy loss power is valid for the photon gas temperatures $T \lesssim (1/10)m_e$ and is inapplicable at temperatures $T \sim m_e$. Thus, the assumption made in [7] that the factor $(T/m_e)^{14}$ can be taken to be on the order of unity is erroneous. Taking into account the above applicability range, we obtain $(T/m_e)^{14} \lesssim 10^{-14}$.

In summary, the neutrino photoproduction on nuclei cannot compete with Urca processes in strong magnetic fields.

This work was supported by the Russian Foundation for Basic Research (project no. 01-02-17334) and the Ministry of Education of the Russian Federation (project no. E00-11.0-5).

REFERENCES

1. C. Kouveliotou *et al.*, Astrophys. J. **510**, L115 (1999).
2. K. Hurley *et al.*, Nature **397**, 41 (1999).
3. G. S. Bisnovatyĭ-Kogan, Astron. Zh. **47**, 813 (1970) [Sov. Astron. **14**, 652 (1971)].
4. R. C. Duncan and C. Thompson, Astrophys. J. **392**, L9 (1992).
5. P. Bocquet *et al.*, Astron. Astrophys. **301**, 757 (1995).
6. C. Y. Cardall, M. Prakash, and J. M. Lattimer, Astrophys. J. **554**, 322 (2001).
7. V. V. Skobelev, Zh. Éksp. Teor. Fiz. **120**, 786 (2001) [JETP **93**, 685 (2001)].
8. Yu. M. Loskutov and V. V. Skobelev, Teor. Mat. Fiz. **70**, 303 (1987).
9. A. V. Kuznetsov, N. V. Mikheev, and D. A. Rumyantsev, Yad. Fiz. **65** (2002) (in press).
10. S. L. Adler, Ann. Phys. (N. Y.) **67**, 599 (1971).
11. A. E. Shabad, Tr. Fiz. Inst. Akad. Nauk SSSR **192**, 5 (1988).

Translated by R. Tyapaev

JETP Letters, Vol. 75, No. 9, 2002, pp. 445–448. Translated from Pis'ma v Zhurnal Éksperimental'noĭ i Teoreticheskoĭ Fiziki, Vol. 75, No. 9, 2002, pp. 535–538.

Resonance Phase and Signs of *P*-Odd and *P*-Even Effects Observed in Neutron Reactions

L. M. Smotritsky

St. Petersburg Nuclear Physics Institute, Russian Academy of Sciences, Gatchina, Leningrad region, 188350 Russia

e-mail: smotrits@mail.pnpi.spb.ru

Received March 7, 2002; in final form, April 9, 2002

It is shown that the introduction of the resonance phase for two quasistationary states with the same spin and opposite parities allows one to gain agreement between the theory and the observed signs of *P*-odd and *P*-even effects in neutron reactions. The joint description of these effects makes it possible to determine the unknown (free) parameters of the theory from the experimental data. © *2002 MAIK "Nauka/Interperiodica".*

PACS numbers: 25.40.Lw; 25.40.Ny

As was shown in [1], the introduction of the resonance phase for two quasistationary states (*s* and *p* resonances) with the same spin and opposite parities provides agreement between the theory and the observed signs of *P*-odd effects (parity violating effects) in neutron reactions. It was also pointed out that taking account of the resonance phase enables one to remove the discrepancy in the joint description of *P*-even effects (conserving parity) in the *p*-wave resonances of the ^{113}Cd and ^{117}Sn nuclei [2–5].

Recall that *P*-odd effects (correlations) arise because weak interaction mixes *s* and *p* resonances, i.e., nuclear levels situated in continuum (compound resonances) near the binding energy of a neutron in the nucleus. The *P*-even effects are due to the overlap of the wave functions of the same *s* and *p* resonances (*P*-even mixing). As will be demonstrated below, the joint description of *P*-odd and *P*-even correlations [6] makes it possible to determine or refine certain unknown (free) parameters of the theory.

Angular and polarization correlations in the interactions of neutrons with nuclei were considered in [7]. Among the 17 possible correlations, we will consider only 4 correlations, for which experimental data are available. The angular distribution of γ-ray photons from the (n, γ) reactions on nuclei is written as

$$W(\theta, \varphi) \sim 1 + A_\gamma \sigma_n \cdot \mathbf{k}_\gamma + P_{tot} \sigma_n \cdot \mathbf{k}_n + FB \mathbf{k}_n \cdot \mathbf{k}_\gamma + LR \sigma_n \cdot [\mathbf{k}_n \times \mathbf{k}_\gamma], \quad (1)$$

where σ_n and $\mathbf{k}_n$ are the neutron spin and momentum, respectively, and $\mathbf{k}_\gamma$ is the momentum of emitted γ-ray photon. The coefficients A_γ and P_{tot} are due to the weak interaction and describe, respectively, the *P*-odd angular asymmetry of photons and the asymmetry arising in the total cross section upon passing longitudinally polarized neutrons with opposite helicities through a sample. The coefficients *FB* and *LR* are due to the *P*-even mixing and describe the forward-backward and left-right asymmetries of photons, respectively.

The coefficients of correlations in Eq. (1) can be expressed in terms of three basic reaction amplitudes [7]. The amplitude f_1 describes neutron capture to an *s* compound state of nucleus *A* and the decay of this state into an $A + 1$ nucleus with the emission of, e.g., an $M1$ photon. The amplitude f_2 describes neutron capture to a *p* state with the emission of an $E1$ photon. The amplitude f_3 describes neutron capture into the *s* state, population of the *p* state owing to weak interaction, and its decay with the emission of an $E1$ photon. In this case, the correlation coefficients in Eq. (1) are expressed as[1]

$$A_\gamma \sim 2\mathrm{Re}(f_1 \cdot f_3^*), \quad (2)$$

$$P_{tot} \sim -2x\mathrm{Re}(f_2 \cdot f_3^*), \quad (3)$$

$$FB \sim 2(-x + y/\sqrt{2})\mathrm{Re}(f_1 \cdot f_2^*), \quad (4)$$

$$LR \sim 2(x + y/\sqrt{2^3})\mathrm{Im}(f_1 \cdot f_2^*). \quad (5)$$

Here, $x = \sqrt{\Gamma^n_{p1/2}/\Gamma^n_p}$, $y = \sqrt{\Gamma^n_{p3/2}/\Gamma^n_p}$, and $(x^2 + y^2 = 1)$ are the channel-mixing parameters, where $\Gamma^n_{p1/2}$ and $\Gamma^n_{p3/2}$ are the partial neutron widths of the *p* resonance in the channels with the neutron total angular momenta $j = 1/2$ and $3/2$, respectively, and Γ^n_p is the total neutron width of the *p* resonance.

As was mentioned in [1], to describe the signs of correlations consistent with the experimental data, one should include the resonance phase in Eqs. (2)–(5).

[1] The amplitude f_4 is ignored because it is small compared to f_3.

0021-3640/02/7509-0445$22.00

According to [8, 9], the resonance phase ϕ_{res} arises as a result of the diagonalization of the Green's function for the compound nuclear state. We introduce ϕ_{res} in the general form $\phi_{res} = \arg(b/a)$, where the parameters b and a are defined below. In this case,

$$\phi_{res} = \arctan[\mathrm{Im}(b/a)/\mathrm{Re}(b/a)], \quad (6)$$

where the resonance phase is defined on the interval $-\pi/2 \le \phi_{res} \le +\pi/2$. However, one can introduce the resonance phase

$$\phi'_{res} = \mathrm{arccot}[\mathrm{Re}(b/a)/\mathrm{Im}(b/a)] \quad (7)$$

defined on the interval $0 \le \phi'_{res} \le \pi$. Substituting the parameters $b = E - E_s + i\Gamma_s/2$ and $a = E - E_p + i\Gamma_p/2$ from [8] into Eq. (7), one obtains the following expression for the resonance phase in terms of the *s*- and *p*-resonance parameters:

$$\phi'_{res}(E) = \mathrm{arccot}\frac{(E-E_s)(E-E_p) + \Gamma_s\Gamma_p/4}{(E-E_p)\Gamma_s/2 - (E-E_s)\Gamma_p/2}. \quad (8)$$

Here, $E_{s,p}$ and $\Gamma_{s,p}$ are the energies and total widths of the *s* and *p* resonance, respectively.

Let us take into account the resonance phase for each of correlations (2)–(5) by introducing the total phase ϕ_Σ. Consider the A_γ correlation. The amplitude f_3 involves the phase shift $-\pi/2$ ($e^{-i\pi/2} = -i$) of the *p*-wave free motion relative to the *s* wave, which is compensated by the purely imaginary matrix element of weak interaction. The same is true for the amplitude f_3^* entering into Eq. (2). Therefore, $\phi_\Sigma = \phi'_{res}$ for A_γ.

As compared to Eq. (2), Eq. (3) for the P_{tot} correlation involves an extra *p* wave associated with f_2. For this reason, the phase difference for the capture to *p* and *s* resonances must be taken into account along with the phase of the *p*-wave free motion. According to [8], this difference is $\phi_p - \phi_s = m\pi$. Taking $m = 1$, we obtain the total phase shift $\phi_\Sigma = \phi'_{res} - \pi/2 + \pi$ for the P_{tot} correlation.

Formulas (4) and (5) involve the complex conjugate amplitude f_2^*. Therefore, the total phase shift is $\phi_\Sigma = \phi'_{res} + \pi/2 - \pi$ for the *FB* correlation and $\phi_\Sigma = \phi_{res} + \pi/2 - \pi$ for the *LR* correlation.

The expressions for the total phase shift can be simplified by introducing the phase dependence for each correlation. Taking into account that the first three correlations depend on the real part of the product of amplitudes, whereas the fourth correlation depends on the corresponding imaginary part, one obtains

$$A_{\gamma\phi} = \cos\phi'_{res}, \quad P_{tot\phi} = -\sin\phi'_{res}, \quad (9)$$

$$FB_\phi = \sin\phi'_{res}, \quad LR_\phi = -\cos\phi_{res}. \quad (10)$$

In fact, one additional parameter (resonance phase) is introduced in Eqs. (9) and (10). As will be shown below, this parameter allows the reproduction of the experimental signs of correlations (2)–(5). The problem of correct introduction of the resonance phase into Eqs. (2)–(5) still remains to be solved.

Let us discuss the experimental data. The *P*-even correlations *FB* and *LR* in *p* resonances were investigated for the ^{113}Cd [2, 3] and ^{117}Sn [3–5] nuclei primarily with the aim of determining the channel-mixing parameters *x* and *y* appearing in Eqs. (4) and (5).

Let us consider the ^{113}Cd$(n, \gamma)^{114}$Cd reaction in more detail. The spin and parity of the ground state of the ^{113}Cd nucleus are $J^\pi = 1/2^+$. The neutron capture is accompanied by the excitation of the *s* resonance with $E_s = 0.18$ eV and $J^\pi = 1^+$ and the *p* resonance with $E_p = 7$ eV $J^\pi = 1^-$. Experimentally, the asymmetry in the angular distribution of the $M1$ and $E1$ γ-ray photons from the decay of resonances to the 0^+ ground state of the ^{114}Cd nucleus is detected. Using Eq. (4) and data on the *FB* correlation, the authors of [2] obtained the following two sets of parameters *x* and *y*:

$$x = 0.975, \quad y = 0.222, \quad (11)$$

$$x = 0.100, \quad y = -0.995. \quad (12)$$

Both sets were used to describe the measurements of *LR* correlation and did not provide agreement with the experiments. Set (11) reproduced the positive *LR* sign but overestimated the magnitude of the effect. Set (12) reproduced the magnitude but gave the opposite sign. Let us take set (12). In this case, the channel-mixing coefficients are determined as $FB_{ch} = -x + y/\sqrt{2} = -0.8$ and $LR_{ch} = x + y/2\sqrt{2} = -0.25$. With allowance for phase dependence (10), the sign of the *FB* correlation is determined by the product

$$FB = FB_e \cdot FB_{ch} \cdot FB_\phi. \quad (13)$$

Here, FB_e is the energy dependence of the correlation presented in an explicit form in [10]. Let us consider the signs of factors in Eq. (13) for the neutron energy slightly below the 7-eV *p* resonance. Then, the *FB* and *LR* signs are determined as (–)(–)(+) = (+) and (+)(–)(–) = (+), respectively. Both signs agree with the experiment [2, 3].

The addition of the resonance phase only slightly changes the energy dependence of correlations (2)–(4) near the resonance, but leads to a more rapid decrease in the effect outside the resonances. Nevertheless, the introduction of this resonance phase is of fundamental importance, because it removes divergences caused by the contributions from far *s* resonances.[2]

[2] I am grateful to Prof. V. V. Flambaum who, at the workshop at ECT* (Trento, June 5–16, 2000), pointed out that the divergence problem is important for the explanation of the P_{tot} sign in the ^{232}Th nucleus [11].

For correlation (5), inclusion of the resonance phase changes considerably the energy dependence and splits the peak of left-right asymmetry in the resonance. The figure shows the energy dependence of the *LR* correlation for the ^{113}Cd(n, γ) reaction. The calculation was carried out using the formula

$$LR(E) = \frac{10^{-2}[(E-E_s)\Gamma_p - (E-E_p)\Gamma_s]\cos\phi_{\rm res}}{(E-E_p)^2 + \Gamma_p^2/4}. \quad (14)$$

This splitting of the *LR* peak does not contradict the existing experimental data [2, 3] and can be observed experimentally. The magnitude of *LR* correlation near the *p* resonance is close to unity. However, its measurement is a difficult experimental problem, because it is necessary to ensure good energy resolution both in the time-of-flight measurement of neutron energy and in the detection of the direct γ transition to the nuclear ground state. The pulsed source of polarized neutrons and the experimental setup at LANSCE satisfy these requirements. The observation of the splitting of the *LR* peak would be direct evidence of the correctness of the above approach.

Let us analyze the ^{117}Sn(n, γ)^{118}Sn reaction, whose spin structure is similar to that for the reaction discussed above. The correlations in this reaction arise due to the mixing of the 1.3-eV *p* resonance and the subthreshold *s* resonance with energy $E_s = -29.2$ eV. In this case, the following two sets of parameters x and y were obtained from the *LR* measurements [3–5]:

$$x = 0.53 \pm 0.04, \quad y = -0.81 \pm 0.03, \quad (15)$$

$$x = 0.01 \pm 0.01, \quad y = 1.00 \pm 0.02. \quad (16)$$

Both sets were used to describe the measurements of the *FB* correlation. Set (15) properly reproduced the correlation sign, but overestimated the magnitude of the effect, especially near the *p* resonance. Set (16) properly reproduced the *FB* magnitude but gave the opposite sign. Let us choose set (16). In this case, the channel-mixing coefficients are determined as $FB_{\rm ch} = 0.7$ and $LR_{\rm ch} = 0.36$ for the ^{117}Sn nucleus. Then, the *FB* and *LR* signs are determined, according to Eq. (13), as (–)(+)(+) = (–) and (+)(+)(–) = (–), respectively. The negative signs of *FB* and *LR* are inconsistent with the experiments [4, 5]. This is due to the fact that the mixing in the ^{117}Sn(n, γ) reaction involves the subthreshold *s* resonance.

The problem of reproducing signs of the *P*-odd effects in the presence of a subthreshold *s* resonance is well known [11] and can be illustrated by the example of the $P_{\rm tot}$ correlation. The inclusion of resonance phase (9) leads to the following simple sign rule that is consistent with the experiment. The sign of the effect is positive (negative) for the nuclei whose *s* resonance is situated above (below) the *p* resonance. However, for the subthreshold *s* resonance lying below the latter, the sign of the effect is positive (see figure in [11]). In other words, according to the sign of the effect, the subthreshold *s* resonance behaves as the above-threshold *s* resonance lying above the *p* resonance at a distance of $E_p + |E_s|$. This model of subthreshold *s* resonance can be used to describe the experiment.

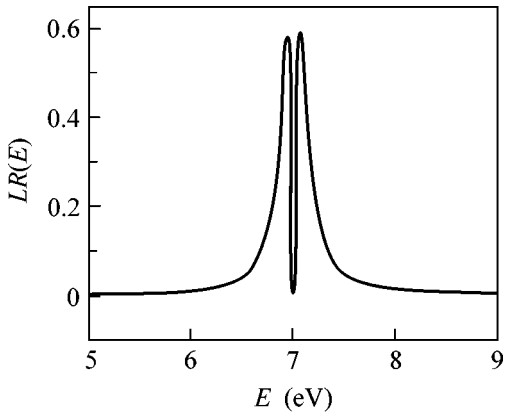

Energy dependence of the *LR* correlation for the ^{113}Cd(n, γ) reaction near the 7-eV *p* resonance, as calculated by Eq. (14) with the parameters $E_s = 0.18$ eV, $\Gamma_s = 0.11$ eV, $g\Gamma_s^n = 3.1 \times 10^{-3}$ eV, $\Gamma_s^{\gamma_1} = 2.8 \times 10^{-4}$ eV, $E_p = 7$ eV, $\Gamma_p = 0.18$ eV, $g\Gamma_p^n = 3.1 \times 10^{-7}$ eV, and $\Gamma_p^{\gamma_1} = 4.5 \times 10^{-3}$ eV.

It is physically more reasonable to assign the subthreshold *s* resonance the capture phase shift different from that for the usual *s* resonance. Let us take $\phi_p - \phi_s = 0$ for the subthreshold *s* resonance. In this case, all signs in the last three phase dependences in Eqs. (9) and (10) must be altered.

The inclusion of the subthreshold *s* resonance in the ^{117}Sn(n, γ) reaction brings about coincidence of the signs of the *FB* and *LR* correlations with the experimental data.

Above, the dependence of the signs of correlations on nuclear properties such as the position, spin, and parity of resonances, resonance phase, etc., is considered in rather close detail. However, correlations (2)–(5) depend also on the amplitudes of neutron capture to *s* and *p* resonances and their decay to the final state. In notation [7], these correlations are expressed as

$$A_{\gamma w} = \frac{\langle p|H_w|s\rangle\langle f,\gamma|H_{\rm em}|p\rangle}{\langle f,\gamma|H_{\rm em}|s\rangle}, \quad (17)$$

$$P_{{\rm tot}w} = \frac{\langle p|H_w|s\rangle\langle s|H_s|n\rangle}{\langle p|H_s|n\rangle}, \quad (18)$$

$$P_{\rm even} = \frac{\langle f,\gamma|H_{\rm em}|p\rangle\langle p|H_s|n\rangle}{\langle f,\gamma|H_{\rm em}|s\rangle\langle s|H_s|n\rangle}. \quad (19)$$

Recall that the difference in the phases of neutron capture to *s* and *p* resonances is explicitly taken into account in Eqs. (18) and (19) by including them in the

total phase. Taking this fact into account, one can conclude that the experimental data testify to the negative sign of expressions (17) and (18) for all nuclei.[3] This fact was confirmed for many nuclei, e.g., considered in [11]. Expression (19) for *P*-even correlations has a positive sign and does not contradict the above-discussed experimental data for the ^{113}Cd and ^{117}Sn nuclei.

A perfect correlation of the signs of amplitudes in Eqs. (17)–(19) is a surprising experimental fact, which has to be explained within the framework of nuclear theory.

Let us discuss (and not prove) this regularity. The following symmetry of Eqs. (17)–(19) is noteworthy: each quantity—wave functions of the $|s\rangle$, $|p\rangle$, and $|f, \gamma\rangle$ states, as well as the operators of the strong H_s and electromagnetic H_{em} interactions—always enters in duplicate. Only the operator H_w of weak interaction is alone. Therefore, the negative sign in Eqs. (17) and (18) must, apparently, be assigned to its contribution.

Recall that the same (negative) sign was observed for the P_{tot} correlation in the semileptonic weak processes of interaction of the longitudinally polarized electrons with deuterium [12]. Such processes, in contrast to the above-discussed nonleptonic weak processes without changing strangeness, are directly calculated in the parton model. In our case, the transition from the quark level of describing the weak interaction to the nucleon level and, then, to the nuclear level is a serious theoretical problem [13], which cannot be correctly solved at present. The above results solve this problem in part.

I am grateful to V.M. Lobashev, V.A. Nazarenko, and A.N. Pirozhkov for their stimulating interest and support of this direction of research. This work was supported by the State Program “Fundamental Nuclear Physics” (project no. 134-08).

[3] The sign of expressions (17) and (18) is negative if the matrix element of weak interaction is defined as $W_{sp} \equiv \langle p^- | H_w | s^+ \rangle$, where $\pm$ are the parities of resonances.

REFERENCES

1. L. M. Smotritskiĭ, Pis’ma Zh. Éksp. Teor. Fiz. **74**, 53 (2001) [JETP Lett. **74**, 51 (2001)].
2. V. P. Alfimenkov, S. B. Borzakov, Yu. D. Mareev, *et al.*, Yad. Fiz. **52**, 927 (1990) [Sov. J. Nucl. Phys. **52**, 589 (1990)].
3. V. P. Skoĭ and É. I. Sharapov, Fiz. Élem. Chastits At. Yadra **22**, 1400 (1991) [Sov. J. Part. Nucl. **22**, 681 (1991)].
4. V. P. Alfimenkov, S. B. Borzakov, Vo Vang Thuan, *et al.*, Pis’ma Zh. Éksp. Teor. Fiz. **39**, 346 (1984) [JETP Lett. **39**, 416 (1984)].
5. D. I. Lyapin, I. M. Salamatin, A. P. Sirotin, *et al.*, Preprint OIYaI R3-90-125 (Joint Institute for Nuclear Research, Dubna, 1990).
6. L. M. Smotritskiĭ, Preprint PIYaF-2466 (Gatchina, 2002).
7. V. V. Flambaum and O. P. Sushkov, Nucl. Phys. A **435**, 352 (1985).
8. O. P. Sushkov and V. V. Flambaum, Usp. Fiz. Nauk **136**, 3 (1982) [Sov. Phys. Usp. **25**, 1 (1982)].
9. V. V. Flambaum and O. P. Sushkov, Nucl. Phys. A **412**, 13 (1984).
10. V. E. Bunakov and V. P. Gudkov, Nucl. Phys. A **401**, 93 (1983).
11. L. M. Smotritskiĭ, Yad. Fiz. **64**, 1501 (2001) [Phys. At. Nucl. **64**, 1424 (2001)].
12. C. Y. Prescott, W. B. Atwood, R. L. A. Cottrell, *et al.*, Phys. Lett. B **77**, 347 (1978).
13. G. A. Lobov, Nucl. Phys. A **577**, 449 (1994).

Translated by R. Tyapaev

JETP Letters, Vol. 75, No. 9, 2002, pp. 449–451. Translated from Pis'ma v Zhurnal Éksperimental'noĭ i Teoreticheskoĭ Fiziki, Vol. 75, No. 9, 2002, pp. 539–541.

Measurement of the $\phi \longrightarrow \pi^0 e^+ e^-$ Decay Probability

M. N. Achasov, K. I. Beloborodov, A. V. Berdyugin, A. G. Bogdanchikov, A. V. Bozhenok, A. D. Bukin, D. A. Bukin, S. V. Burdin, A. A. Valishev, A. V. Vasil'ev, V. B. Golubev, T. V. Dimova,* V. P. Druzhinin, P. M. Ivanov, V. N. Ivanchenko, A. A. Korol', S. V. Koshuba, A. A. Mamutkin, A. V. Otboev, E. V. Pakhtusova, A. A. Sal'nikov, S. I. Serednyakov, V. A. Sidorov, Z. K. Silagadze, A. N. Skrinskiĭ, A. G. Skripkin, V. V. Sharyĭ, and Yu. M. Shatunov

Budker Institute of Nuclear Physics, Siberian Division, Russian Academy of Sciences, pr. Akademika Lavrent'eva 11, Novosibirsk, 630090 Russia

Novosibirsk State University, ul. Pirogova 2, Novosibirsk, 630090 Russia

** e-mail: baiert@inp.nsk.su*

Received March 20, 2002

The measurement of the $\phi \longrightarrow \pi^0 e^+ e^-$ conversion decay probability on the SND detector at the VEPP-2M e^+e^- collider gave the value $\mathrm{Br}(\phi \longrightarrow \pi^0 e^+ e^-) = (1.01 \pm 0.28 \pm 0.29) \times 10^{-5}$. © *2002 MAIK "Nauka/Interperiodica".*

PACS numbers: 13.25.Jx; 14.40.Cs

1. Since the conversion decays $V \longrightarrow Pe^+e^-$ of vector mesons (V) into pseudoscalar mesons (P) proceed through an intermediate state $P\gamma^*$ with a virtual photon γ^*, they are closely related to the corresponding radiative decays $V \longrightarrow P\gamma$. The probability of emission of a virtual photon with 4-momentum q is determined by the structure of electromagnetic V–P transition, which is described by the corresponding electromagnetic transition form factor. The effect of the transition form factor is primarily manifested in the hard part of the spectrum of e^+e^- invariant masses, whereas the total decay probability is determined by the invariant mass region near the threshold $q^2 = 4m_e^2$ (m_e is electron mass), where the transition form factor differs negligibly from unity. The probability of conversion decay is on the order of $\sim 10^{-2}$ of the probability of the corresponding radiative decay.

In this paper, we study the decay

$$\phi \longrightarrow \pi^0 e^+ e^-, \quad \pi^0 \longrightarrow \gamma\gamma, \tag{1}$$

whose branching ratio should be equal to 1.3×10^{-5}, according to formulas given in [1]. This decay probability was measured on a KMD-2 detector [2].

2. The SND detector [3] is a universal nonmagnetic detector, whose basic unit is a three-layer electromagnetic calorimeter consisting of 1632 NaI(Tl) crystals. The calorimeter provides energy resolution for photons $\sigma_E/E = 4.2\%/\sqrt[4]{E(\mathrm{GeV})}$ and an angular resolution of about 1.5°. The solid angle of the calorimeter is 90% of 4π. The angles of charged particles are measured by a system of two drift chambers. The accuracy of measurements of the azimuthal and polar angles is about 0.5° and 2°, respectively. The solid angle of the drift chamber system is 95% of 4π.

In this paper, we used the statistics accumulated in the experiments on scanning the region of ϕ-meson resonance in 1996 and 1998 [4]. The data recorded in the c.m. energy range $2E_0 = 1016$–1024 MeV with an integrated luminosity of 8.8 pb^{-1} corresponding to 2.0×10^7 ϕ-meson decays were processed.

3. Most events of the process in question are characterized by a small diverging angle of the electron–positron pair. Since the SND detector has no magnetic field, such a e^+e^- pair is detected in drift chambers as a single charged particle.

We sampled the events satisfying the following conditions:

One charged track and two photons with energies above 50 MeV are found in an event.

A track is spaced from the beam axis in the R–ϕ plane by $R < 0.5$ cm, and the z coordinate of the point closest to the axis of beams is limited by $|Z| < 10$ cm.

The polar angle of all particles lies in the range $36° < \theta < 144°$.

The total normalized energy release in the calorimeter is limited by the condition $E_{\mathrm{tot}}/2E_0 > 0.8$.

The total normalized momentum is limited by the constraint $P_{\mathrm{tot}}/E_{\mathrm{tot}} < 0.15$.

The kinematic reconstruction parameter describing the accuracy of energy and momentum conservation in an event is $\chi^2 < 15$.

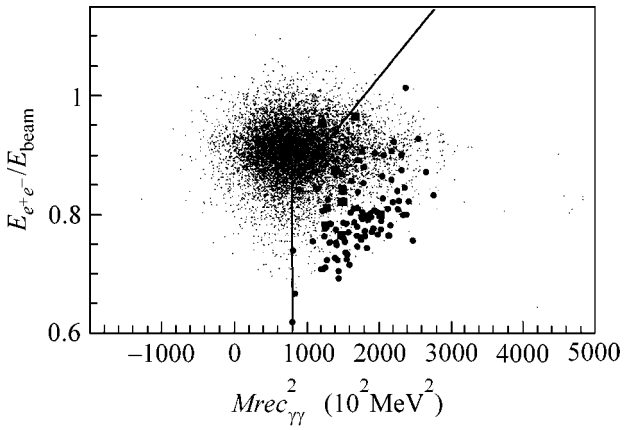

Fig. 1. Distribution of the simulated events in the squared photon-pair recoil mass, $Mrec^2_{\gamma\gamma}$, and the e^+e^--pair energy release, $E_{e^+e^-}/E_{\text{beam}}$, normalized to the beam energy: the process in question (gray points) and the background from the $e^+e^- \longrightarrow \pi^+\pi^-\pi^0$ process (squares) with the use of all sampling conditions (circles) with weaker sampling conditions ($\chi^2 < 50$). The line shows the chosen sampling condition.

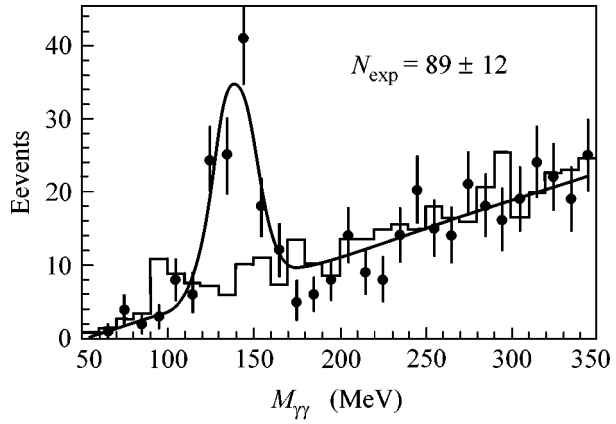

Fig. 2. Photon-pair invariant mass distribution: (points) experimental data, (histogram) calculated background from the $\phi \longrightarrow \eta\gamma$, $\eta \longrightarrow e^+e^-\gamma$ decay and QED processes, and (line) the approximation of the experimental points by the sum of Gaussian and linear functions. In this case, the number of events in the peak was one of the approximation parameters.

However, among events satisfying the above sampling conditions, there are events not only of process (1) but also of the background processes

$$e^+e^- \longrightarrow \pi^+\pi^-\pi^0, \tag{2}$$

$$e^+e^- \longrightarrow \pi^0\gamma, \quad \pi^0 \longrightarrow 2\gamma \tag{3}$$

(the latter with photon conversion on a substance).

To suppress the background coming from process (2), a two-dimensional distribution of simulated events was plotted against the squared photon-pair recoil mass and the e^+e^--pair energy release (Fig. 1). As a result, we introduced an additional sampling condition shown in Fig. 1. After the use of this condition, the number of background events of process (2) was calculated by simulation to obtain $N_{3\pi} = 1 \pm 1$. To estimate the error of simulating nuclear interaction of pions, the experimental spectra of energy release by charged pions were compared with the corresponding simulated spectra. It was concluded that the experimental background from process (2) differed from the simulated background by no more than a factor of 3. For this reason, the value $N_{3\pi} = 3 \pm 3$ was used as an estimate for the background.

For the events satisfying all sampling conditions, the distribution of photon-pair invariant mass was constructed (Fig. 2). The spectrum has a peak near the π^0 mass. The number of events in the peak was determined through approximating the spectrum by the sum of a Gaussian and a linear function and was found to be equal to $N_{\text{exp}} = 89 \pm 12$.

The events of process (3) can satisfy the sampling conditions because of the conversion of photons on a substance ahead of the drift chamber. The conversion of photons in the detector substance was studied in [5], where it was demonstrated that the simulation of conversion closely reproduced the experimental data. For this reason, the number of background events of process (3) was determined by simulation and found to be $N_{\text{con}} = 34 \pm 6$.

The analysis of the energy dependence of the cross section for the $e^+e^- \longrightarrow \pi^0\gamma$ process similar to the process under consideration, indicates that the amplitudes of the $e^+e^- \longrightarrow \pi^0\gamma$ transition through ρ and ω mesons contribute to the cross section in the ϕ-meson region. However, it is impossible to obtain the energy dependence for the $e^+e^- \longrightarrow \pi^0e^+e^-$ process because of low statistics. For this reason, the probability of the $\phi \longrightarrow \pi^0e^+e^-$ process was calculated by using the coefficient K which took into account the transition amplitudes through the ρ and ω mesons. This coefficient was calculated on the basis of the measured cross section for the $e^+e^- \longrightarrow \pi^0\gamma$ process [6]:

$$K = \frac{\sum_i \sigma(E_i)\delta(E_i)L(E_i)}{N_\phi \text{Br}(\phi \longrightarrow \pi^0\gamma)}, \tag{4}$$

where $\sigma(E_i)$ is the Born cross section for the $e^+e^- \longrightarrow \pi^0\gamma$ process at each energy point E_i, $\delta(E_i)$ is the radiative correction, $L(E_i)$ is the integrated luminosity, and N_ϕ is the number of ϕ mesons detected on this interval. The resulting correction coefficient is $K = 1.42 \pm 0.12$. The error is primarily determined by the accuracy of the cross section measured for the $e^+e^- \longrightarrow \pi^0\gamma$ process.

The detection efficiency was determined by simulation and found to be $\epsilon = (17.8 \pm 0.2)\%$ (statistical error). The branching ratio of decay (1) was calculated by the formula

$$\mathrm{Br}(\gamma \longrightarrow \pi^0 e^+ e^-) = \frac{(N_{\exp} - N_{3pi})/K - N_{\mathrm{con}}}{N_\phi \epsilon \mathrm{Br}(\pi^0 \longrightarrow 2\gamma)}, \quad (5)$$

yielding $\mathrm{Br}(\phi \longrightarrow \pi^0 e^+ e^-) = (1.01 \pm 0.28 \pm 0.29) \times 10^{-5}$. The error is statistical and includes the errors of $N_{\exp}$ and N_{3pi}.

The systematic error was calculated by taking into account the following sources: error in the number of ϕ mesons (3%); limited statistics of simulating process (1) (1%); errors in the determination of detection efficiency (5%); error in the determination of the correction coefficient K (10%); statistical error in the number of photons converted on the substance ahead of the drift chamber (17%); error in the amount of the substance ahead of the drift chamber (5%); and errors in the $\phi \longrightarrow \pi^0\gamma$ decay probabilities (8%). The resulting error was equal to 27%.

4. Within two standard deviations, the measured branching ratio $\mathrm{B}(\phi \longrightarrow \pi^0 e^+ e^-) = (1.01 \pm 0.28 \pm 0.29) \times 10^{-5}$ agrees with the calculation (1.3×10^{-5} [1]) and with the previous experiment on the SMD-2 detector, $\mathrm{B}(\phi \longrightarrow \pi^0 e^+ e^-) = (1.22 \pm 0.34 \pm 0.21) \times 10^{-5}$ [2].

REFERENCES

1. L. G. Landsberg, Phys. Rep. **128**, 301 (1985).
2. R. R. Akhmetshin, E. V. Anashkin, M. Arpagaus, *et al.*, Phys. Lett. B **503**, 237 (2001).
3. M. N. Achasov, V. M. Aulchenko, S. E. Baru, *et al.*, Nucl. Instrum. Methods Phys. Res. A **449**, 125 (2000).
4. M. N. Achasov, V. M. Aulchenko, S. E. Baru, *et al.*, Preprint Budker INP 98-65 (Budker Institute of Nuclear Physics, Novosibirsk, 1998).
5. M. N. Achasov, V. M. Aulchenko, K. I. Beloborodov, *et al.*, Phys. Lett. B **504**, 275 (2001).
6. M. N. Achasov, A. V. Berdyugin, A. V. Bozhenok, *et al.*, Eur. Phys. J. C **12**, 25 (2000).

Translated by R. Tyapaev

JETP Letters, Vol. 75, No. 9, 2002, pp. 452–456. From Pis'ma v Zhurnal Éksperimental'noĭ i Teoreticheskoĭ Fiziki, Vol. 75, No. 9, 2002, pp. 542–546.

Polarized Triplet Production by Circularly Polarized Photons[1]

V. V. Bytev[1], E. A. Kuraev[1,*], M. V. Galynskii[2], and A. P. Potylitsyn[3]

[1] *Joint Institute for Nuclear Research, Dubna, Moscow region, 141980 Russia*

**e-mail: kuraev@thsun1.jinr.ru*

[2] *Institute of Physics, Belarussian Academy of Sciences, Minsk, 220072 Belarus*

[3] *Tomsk Polytechnic University, Tomsk, 634050 Russia*

Received March 20, 2002

A process of pair production by a circularly polarized photon in the field of an unpolarized atomic electron was considered in the Weizaecker–Williams approximation. The degree of longitudinal polarization of a positron and an electron was calculated. An exclusive cross section, as well as a spectral distribution, were obtained. We estimate the accuracy of our calculations at the level of a few percent. We show the identity of the positron polarization for the considered process and for the process of pair production in the screened Coulomb field of a nucleus. © *2002 MAIK "Nauka/Interperiodica".*

PACS numbers: 13.40.-f; 13.88.+e; 14.60.Cd

In this paper, we consider the process $\gamma(k) + e^-(p) \longrightarrow e^-(q_-) + e^+(q_+) + e^-(p')$ in the high-energy limit where the polarization states of initial photon and production particles e^+, e^- are helical. The differential cross section for an electron–positron pair photoproduction on a free electron in the Born approximation is described by eight Feynman diagrams (FD) [1], which are shown in Fig. 1 and Fig. 2. In the high-energy limit (for a photon energy of 54 MeV in lab system), only the subsets of the two Bethe–Heitler (BH) diagrams (see Fig. 1) are relevant for the level of accuracy $m^2/s \sim 10^{-2}$; m is the electron mass, and s is $s = 2kp = 2m\omega$, where ω is the photon energy at the laboratory frame, whereas the contributions we examine are on the order of $s/m^2 \sim 200 \gg 1$. We also do not consider nonlogarithmic terms because of their smallness, $\sim 10^{-1}$, in comparison with logarithmic terms, $2\ln(s/m^2) \sim 10$. Further calculations will be performed in the Weizaecker–Williams (WW) approximation [2].

The differential cross section for triplet photoproduction in the Born approximation for the nonpolarized case was calculated numerically in [3, 4] by Monte Carlo simulation of all eight FD contribution. The closed analytic expression is very cumbersome and was first obtained in a complete form in works [5]. A detailed analysis of the expressions of Haug's work reveals that the interference terms of the BH matrix elements with the other three gauge-invariant subsets (which take into account the bremsstrahlung mechanism of pair creation and Fermi statistics for fermions) turn out to be on the order of a few percent for $s > 50$–60 m^2.

The differential cross section for electron–positron pair production by linearly polarized photons was derived in a series of papers [6–8] (see also [9] and references therein). In [10], Monte Carlo simulation was performed for the process under consideration, in which all eight lowest order diagrams can be numerically treated without approximation. There, it was shown that one might consider only the two leading graphs in a wide range of photon energies from 50 to 550 MeV. Note that this observation was made earlier for the nonpolarized case in the works of Kopylov *et al.* [3] and Haug [5] (who presented his results in explicit analytic form).

The process of the polarized pair production by a polarized photon in the screened Coulomb field of a nucleus was considered in the high-energy limit in works [11, 12]. Here, the degree of longitudinal polarization of an electron was calculated.

From papers [3, 5] it follows that (1) the contribution of FD (see Fig. 2), as well as interference of its amplitude with the amplitude of (see Fig. 1), can be neglected within an accuracy of 3% as compared with the contribution of (see Fig. 1), starting with photon energies of $\omega > 30$ MeV in laboratory frame; (2) one can use the asymptotic formulas at a very high photon-energy contribution of Bethe–Heitler FD (see Fig. 1) within an accuracy of 5% starting with energies on the order of $\omega > 100$ MeV. Taking into account that the nonpolarized cross section dominates those depending on particle polarization, we estimate the accuracy of WW (logarithmical approximation) at the level of 10%.

Our paper is organized as follows. Using the Sudakov technique, we calculate the differential cross section and the degree of longitudinal polarization of an electron and positron in the process of pair production by a circularly polarized photon on electron. In conclusion, we discuss different schemes of production of lon-

[1] This article was submitted by the authors in English.

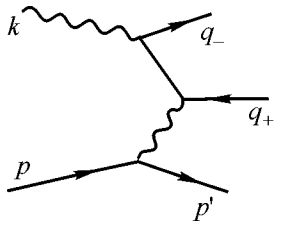

Fig. 1. Types of relevant Feynman diagrams.

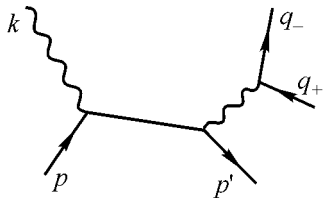

Fig. 2. Types of irrelevant Feynman diagrams.

gitudinally polarized positrons in experimental setups. The method described here is one of the most promising ones. It is our motivation for investigation. In the Appendix, we give, in the Born approximation, the differential cross section for the triplet production process for the case where polarization states of all particles are helical by using the crossing transformation of the corresponding differential cross section for the Möller bremsstrahlung process in the ultrarelativistic (massless) limit. The corresponding formulas for the degree of longitudinal polarization of the positron in terms of the kinematical invariant and helicity of the initial photon are given for the case of high-energy large-angle scattering.

The cross section for the process. The cross section for the process is proved in the following form:

$$d\sigma = \frac{(4\pi\alpha)^3}{4(2\pi)^5 s}\Sigma M^2 \frac{d^3q_-}{2\varepsilon_-}\frac{d^3q_+}{2\varepsilon_+}\frac{d^3p'}{2\varepsilon'} \times \delta^4(p+k-q_+-q_--p'), \quad (1)$$

where p', ε' is four-momentum and energy of a scattered electron; $q_\pm$ and $\varepsilon_\pm$ are four-momentum and the energy of an electron and positron, correspondingly. We accept here the Sudakov form [2] of the peripheric process. Let us determine the basis vectors in the Sudakov representation of kinematics: the vector of momentum transfer $q = p - p'$ and the light-like vector $\tilde{p} = p - k\frac{m^2}{s}$, a $\tilde{p}^2 = 0$ (k is the 4-momentum of impact photon). The Sudakov representation of four-momenta are

$$q = \alpha\tilde{p} + \beta k + q_\perp, \quad q_\pm = \alpha_\pm\tilde{p} + \beta_\pm k + q_{\perp\pm}, \quad a_\perp k = a_\perp\tilde{p} = 0. \quad (2)$$

The quantities $\beta_\pm$ can be interpreted as the energy fraction of pair components of photon energy, $\beta_+ + \beta_- = 1$. The conservation law of transverse momenta is $q_\perp = q_{\perp+} + q_{\perp-}$. Momentum components along $\tilde{p}$ are small. Using the mass-shell conditions of pair components and the scattered electron leads to

$$s\alpha_\pm = \rho_\pm/\beta_\pm, \quad (3)$$

$$s\beta(1-\alpha) = -\mathbf{q}^2 - m^2\alpha, \quad (4)$$

$$\rho_\pm = \mathbf{q}_\pm^2 + m^2, \quad (5)$$

where we use the two-dimensional Euclidean vectors $q_\perp^2 = -\mathbf{q}^2$, $q_{\perp\pm}^2 = -\mathbf{q}_\pm^2$. The Sudakov parameter α can be related to the invariant mass of the created pair

$$s_1 = (q_+ + q_-)^2, \quad s\alpha = s_1 + \mathbf{q}^2. \quad (6)$$

Using conditions of mass-shell and smallness of Sudakov parameter α, the momentum transfer to the target square can be written in the following form:

$$q^2 = -\mathbf{q}^2 - m^2(s_1/s)^2. \quad (7)$$

We see that $q^2 < 0$ is negative and has nonzero magnitude. Using the Sudakov representation of the momentum phase volume of the particle

$$d^4q = \frac{s}{2}d\alpha d\beta a^2 q_\perp, \quad (8)$$

we perform the phase volume of the final state:

$$d\Gamma = \frac{d^3q_-}{2\varepsilon_-}\frac{d^3q_+}{2\varepsilon_+}\frac{d^3p'}{2\varepsilon'}\delta^4(p+k-q_+-q_--p') = \frac{1}{2s}\frac{d\beta_-}{\beta_-\beta_+}d^2q_-d^2q. \quad (9)$$

Let us now consider the matrix element

$$M = \bar{u}(p')\gamma^\mu u(p)\frac{1}{q^2}e_\rho(k)\bar{u}(q_-)O^{\rho\nu}v(q_+)g_{\mu\nu}.$$

By using the Gribov decomposition of the metric tensor and omitting the terms of the order m^2/s compared to the terms of the order of unity

$$g_{\mu\nu} = g_{\mu\nu}^\perp + \frac{2}{s}(\tilde{p}_\mu k_\nu + \tilde{p}_\nu k_\mu) \approx \frac{2}{s}\tilde{p}_\nu k_\mu, \quad (10)$$

one can obtain the matrix element in the following form:

$$M = \frac{-2sN_p}{\mathbf{q}^2 + m^2(s_1/s)^2}e_\rho(k)\bar{u}(q_-)V^\rho v(q_+), \quad V^\rho = \frac{1}{s}O^{\rho\nu}\tilde{p}_\nu, \quad N_p = \frac{1}{s}\bar{u}(p')\hat{k}u(p), \quad |N_p| = 1. \quad (11)$$

Using the mass-shell conditions we can express the matrix 4-vector V_ρ as

$$V_\rho = \beta_+\beta_-\left(\frac{1}{\rho_-}-\frac{1}{\rho_+}\right)\gamma_\rho + \frac{\beta_+}{\rho_+}\hat{\tilde{p}}\hat{q}\gamma_\rho - \frac{\beta_-}{\rho_-}\gamma_\rho\hat{q}\hat{\tilde{p}}. \quad (12)$$

One can see that the quantity V_ρ is proportional to $|q_\perp|$ at small $|q_\perp|$. The WW approximation corresponds to the logarithmical enhancement factor:

$$\int\frac{d\mathbf{q}^2\mathbf{q}^2}{(\mathbf{q}^2+m^2(s_1/s)^2)^2} \approx 2\ln\frac{s}{s_1}. \quad (13)$$

The polarization matrix of density $\tau_\pm^{\delta_\pm}$ for $e^\pm$ particles have the following form:

$$\tau_\pm^{\delta_\pm} = \frac{1}{2}(\hat{q}_\pm \mp m)(1-\delta_\pm\gamma^5\hat{s}_\pm),$$
$$\gamma^5\hat{s}_\pm\tau_\pm^{\delta_\pm} = \delta_\pm\tau_\pm^{\delta_\pm}. \quad (14)$$

We will express the particle spin vectors $s_\pm$ in terms of the 4-momenta $q_\pm$ and $\tilde{p}$,

$$s_\pm = \frac{\mp q_\pm}{m} \pm \frac{2m\tilde{p}}{s\beta_\pm}, \quad s_\pm q_\pm = 0, \quad s_\pm^2 = -1. \quad (15)$$

The circular polarization vector e^λ of a photon with 4-momentum k is conveniently defined by using the 4-vectors q_+, q^-, and k [13]:

$$e_\mu^\lambda = \frac{(q_-k)(q_+)_\mu - (q_+k)(q_-)_\mu + i\lambda\varepsilon_{\mu\nu\rho\sigma}q_+^\nu q_-^\rho k^\sigma}{\sqrt{2z}},$$

$$z = -((q_-k)q_+ + (q_+k)q_-)^2 = \frac{\rho^2(\rho-m^2)}{4\beta_+^2\beta_-^2}.$$

Performing the angular averaging on d^2q and extracting the WW factor, we write down the differential cross sections in the form (in the WW approximation, we can put $\rho_+ = \rho_- = \rho$):

$$\frac{d\sigma}{d\mathbf{q}_-^2 d\beta_-} = \frac{2\alpha^3}{\rho^2}\ln\frac{s}{m^2}\Big[1-2\beta_+\beta_- + \frac{4m^2}{\rho^2}(\rho-m^2)\beta_+\beta_-$$
$$+\lambda\delta_+\left(\beta_+-\beta_- + \frac{4m^2}{\rho^2}(\rho-m^2)\beta_-\right)$$
$$+\lambda\delta_-\left(\beta_+-\beta_- + \frac{4m^2}{\rho^2}(\rho-m^2)\beta_+\right) \quad (16)$$
$$+\delta_+\delta_-\left(-6\beta_+\beta_- + \frac{\rho-m^2}{m^2} - \frac{4m^2}{\rho^2}(\rho-m^2)(1-3\beta_+\beta_-)\right)\Big].$$

In the case where the initial electron is polarized, the formula given above is not changed. The corresponding effects are on the order m^2/s. Performing the summation over the polarization of the electron in Eq. (16), we get the differential cross sections for creating a polarized positron,

$$\frac{d\sigma^+}{d\mathbf{q}_-^2 d\beta_-} = \frac{4\alpha^3}{\rho^2}\ln\frac{s}{m^2}$$
$$\times\Big[1-2\beta_+\beta_- + \frac{4m^2}{\rho^2}(\rho-m^2)\beta_+\beta_- \quad (17)$$
$$+\lambda\delta_+\left(\beta_+-\beta_- + \frac{4m^2}{\rho^2}(\rho-m^2)\beta_-\right)\Big],$$

and an analogous expression for the cross section for creating a polarized electron,

$$\frac{d\sigma^-}{d\mathbf{q}_-^2 d\beta_-} = \frac{4\alpha^3}{\rho^2}\ln\frac{s}{m^2}$$
$$\times\Big[1-2\beta_+\beta_- + \frac{4m^2}{\rho^2}(\rho-m^2)\beta_+\beta_- \quad (18)$$
$$+\lambda\delta_-\left(\beta_+-\beta_- + \frac{4m^2}{\rho^2}(\rho-m^2)\beta_+\right)\Big].$$

From Eqs. (17) and (18) we have the degree of longitudinal polarization of the electron (positron) when the polarization of the positron (electron) is not registered:

$$\delta_\pm^f = \lambda\frac{\beta_+-\beta_- \pm (4m^2/\rho^2)(\rho-m^2)\beta_\mp}{1-2\beta_+\beta_- + (4m^2/\rho^2)(\rho-m^2)\beta_+\beta_-}. \quad (19)$$

The result (21) is in agreement with the one given in more general form in [12] [see Eq. (19.8)]. Performing the integration over transverse momenta of the pair, we obtain for the spectral distribution

$$\frac{d\sigma^+}{d\beta_-} = 4\alpha r_0^2\ln\frac{s}{m^2}\Big[1-\frac{4}{3}\beta_+\beta_- + \lambda\delta_+\left(1-\frac{4}{3}\beta_-\right)\Big]. \quad (20)$$

Here, we use, in the WW approximation, $|\mathbf{q}_+| = |\mathbf{q}_-|$; $\rho = \rho_+ = \rho_- = \mathbf{q}_-^2 + m^2$; and λ is the degree of circular polarization of the initial photon. The degree of longitudinal polarization of the created $e^\pm$ particles has the form

$$\delta_\pm^f = \lambda\left(1-\frac{4}{3}\beta_\mp\right)\Big/\left(1-\frac{4}{3}\beta_+\beta_-\right). \quad (21)$$

We see from Eq. (21) that, in the limit $\beta_+ \longrightarrow 1 (\beta_- \longrightarrow 1)$, the degree of longitudinal polarization of the positron (electron) equals the degree of circular polarization of the initial photon (see Fig. 3).

Let us compare the result obtained with the calculations of longitudinal positron polarization from the pair-production process in the screened Coulomb field

of a nucleus [11]. With the same accuracy as before, we can write (see [14])

$$\delta_+^f \approx \frac{\frac{4}{3}\beta_+ - \frac{1}{3}}{(\beta_+^2 + \beta_-^2) + \frac{2}{3}\beta_+\beta_-}\lambda. \qquad (22)$$

Keeping in mind that $\beta_- = 1 - \beta_+$, one can obtain the same result from (21).

Several schemes of creating polarized positrons for electron-positron colliders were proposed in [15]. Longitudinally polarized positrons are produced in the pair-production process by a circularly polarized photon with energy an >10 MeV. A circularly polarized γ beam is formed due to undulator radiation of electrons with energy $E \sim 10^2$ GeV in a helical undulator [16] or due to the Compton backscattering process of the circularly polarized laser photons by an electron beam with energy >1 GeV [17]. In both cases, only the process of pair production in the screened Coulomb field of the nucleus was considered as a source of polarized positrons. The process of triplet production was considered as a background process [14]. The obtained results allow one to develop a correct Monte Carlo code for receiving positron polarization in the real experimental situation with allowance for both processes of pair production in an amorphous target [18].

In recent experiment [19], the authors measured the circular polarization of γ-ray quanta with energy >20 MeV using the magnetized iron polarimeter. The thickness of the iron substance was too large (7 cm), so the correct estimate of the analyzing power should have been done using the Monte Carlo technique. In this case, the polarization characteristics of all reaction particles should be taken into account, and our results cover the existing deficiency.

APPENDIX

The differential cross section for the triplet production process can easily be calculated with the help of the crossing transformation of the expression for squared amplitudes of the Möller bremsstrahlung process

$$e^-(p_1) + e^-(p_2) \longrightarrow e^-(p_3) + e^-(p_4) + \gamma(k), \qquad (23)$$

which corresponds to eight Feynman diagrams. In [13], the differential cross section for this reaction was calculated in the case where all fermions were massless ($p_i^2 = 0$, where $i = 1, 2, 3, 4$), taking into account the polarization of initial electrons and the emitted photon. Let us introduce invariant variables:

$$\begin{aligned} s_1 &= (p_1 + p_2)^2, \quad t_1 = (p_1 - p_3)^2, \\ u_1 &= (p_1 - p_4)^2, \\ s_2 &= (p_3 + p_4)^2, \quad t_2 = (p_2 - p_4)^2, \\ u_2 &= (p_2 - p_3)^2, \end{aligned} \qquad (24)$$

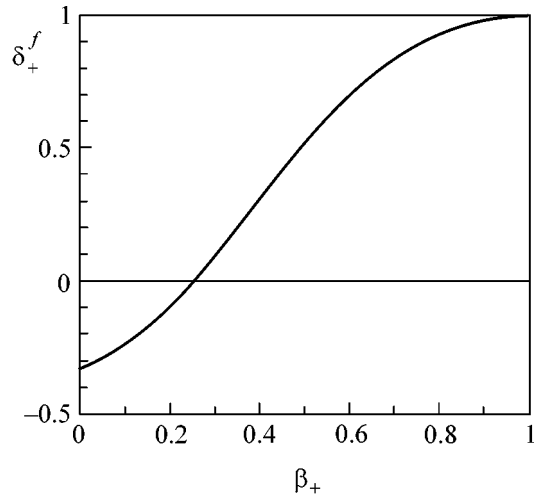

Fig. 3. The degree of longitudinal polarization of positron δ_+^f (21) versus β_+.

helicities δ_1 and δ_2 for initial electrons with momenta p_1 and p_2 respectively, and λ for the helicity of the emitted photon. The differential cross section for reaction (23) in the case of helically polarized initial electrons and a photon has the following form [13]:

$$\begin{aligned} d\sigma_M &= \frac{\alpha^3}{2\pi^2 s} A_M W_M d\Gamma_M, \quad A_M = \frac{A_{MB}}{t_1 t_2 u_1 u_2}, \\ d\Gamma_M &= \frac{d^3\mathbf{p}_3}{2p_{30}}\frac{d^3\mathbf{p}_4}{2p_{40}}\frac{d^3\mathbf{k}}{2\omega}\delta(p_1 + p_2 - p_3 - p_4 - k). \end{aligned} \qquad (25)$$

Expressions for A_{MB} and W_M are [13]

$$\begin{aligned} A_{MB} = {} & (1 + \delta_1\delta_2)[(1 + \delta_1\lambda)s_1 s_2 s_2^2 + (1 - \delta_1\lambda)s_1 s_2 s_1^2] \\ & + (1 - \delta_1\delta_2)[(1 + \delta_2\lambda)(t_1 t_2 t_1^2 + u_1 u_2 u_1^2) \\ & + (1 - \delta_2\lambda)(t_1 t_2 t_2^2 + u_1 u_2 u_2^2)], \end{aligned} \qquad (26)$$

$$W_M = -\left(\frac{p_1}{p_1 k} + \frac{p_2}{p_2 k} - \frac{p_3}{p_3 k} - \frac{p_4}{p_4 k}\right)^2. \qquad (27)$$

Photoproduction diagrams for the triplet

$$\gamma(k) + e^-(p) \longrightarrow e^-(q_-) + e^+(q_+) + e^-(p') \qquad (28)$$

are different from the ones for the Möller bremsstrahlung process (23) with the exchange

$$\begin{aligned} & p_1 \longrightarrow p, \quad p_2 \longrightarrow -q_+, \quad p_3 \longrightarrow p', \quad p_4 \longrightarrow q_-, \\ & k \longrightarrow -k, \quad \lambda \longrightarrow -\lambda, \quad \delta_1 \longrightarrow \delta_1, \quad \delta_2 \longrightarrow -\delta_+. \end{aligned} \qquad (29)$$

Both processes (23) and (28) are two crossing channels with the same (generalized) reaction. After the

change (29) of invariant variables (24), they take the from

$$s_1 = (p - q_+)^2, \quad t_1 = (p - p')^2, \quad u_1 = (p - q_-)^2,$$
$$s_2 = (p' + q_-)^2, \quad t_2 = (q_+ + q_-)^2, \quad u_2 = (p' + q_+)^2. \tag{30}$$

Since the squared amplitude for process (28) after the change of variables (29) is similar to the one for process (23), one can then obtain, after summing the initial electron polarization in reaction (28) from (25), the following formula for triplet production taking into account the polarization of the initial photon and the scattered positron:

$$d\sigma_{\rm tr} = \frac{\alpha^3}{2\pi^2 s} A_{\rm tr} W_{\rm tr} d\Gamma, \tag{31}$$

$$A_{\rm tr} = \frac{A^{\rm tr}_{MB}}{t_1 t_2 u_1 u_2}, \quad A^{\rm tr}_{MB} = A^0_{\rm tr} + \delta_+ \lambda A^1_{\rm tr},$$

$$A^0_{\rm tr} = s_1 s_2 (s_1^2 + s_2^2) + t_1 t_2 (t_1^2 + t_2^2) + u_1 u_2 (u_1^2 + u_2^2),$$
$$A^1_{\rm tr} = -s_1 s_2 (s_1^2 - s_2^2) + t_1 t_2 (t_1^2 - t_2^2) + u_1 u_2 (u_1^2 - u_2^2), \tag{32}$$

$$W_{\rm tr} = -\left(\frac{p}{pk} + \frac{q_+}{q_+ k} - \frac{p'}{p'k} - \frac{q_-}{q_- k}\right)^2,$$

where $s = (p + k)^2$ and $d\Gamma$ are defined by Eq. (9). Then, for the degree of longitudinal polarization of the produced positron $\delta^f_+ = A^1_{\rm tr}/A^0_{\rm tr}$, we have the expression

$$\delta^f_+ = \lambda \frac{-s_1 s_2 (s_1^2 - s_2^2) + t_1 t_2 (t_1^2 - t_2^2) + u_1 u_2 (u_1^2 - u_2^2)}{s_1 s_2 (s_1^2 + s_2^2) + t_1 t_2 (t_1^2 + t_2^2) + u_1 u_2 (u_1^2 + u_2^2)}.$$

This formula is valid only when the squared invariant mass of any particle pair is greater than the squared electron mass.

REFERENCES

1. A. I. Akhiezer and V. B. Berestetskii, *Quantum Electrodynamics* (Nauka, Moscow, 1981; Wiley, New York, 1965).
2. V. N. Baier, V. S. Fadin, V. A. Khoze, and E. A. Kuraev, Phys. Rep. **78**, 293 (1981).
3. G. Kopylov, L. Kuliukina, and I. Polubarinov, Zh. Éksp. Teor. Fiz. **46**, 1715 (1964) [Sov. Phys. JETP **19**, 1158 (1964)].
4. K. J. Mork, Phys. Rev. **160**, 1065 (1967).
5. E. Haug, Z. Naturforsch. A **30**, 1099 (1975); Phys. Rev. D **31**, 2120 (1985); **32**, 1594 (1985).
6. V. F. Boldyshev and Yu. P. Peresun'ko, Yad. Fiz. **13**, 588 (1971) [Sov. J. Nucl. Phys. **13**, 333 (1971)].
7. E. A. Vinokurov and E. A. Kuraev, Zh. Éksp. Teor. Fiz. **63**, 1142 (1972) [Sov. Phys. JETP **36**, 602 (1973)].
8. I. V. Akushevich, H. Anlauf, E. A. Kuraev, *et al.*, Phys. Rev. A **61**, 032703 (2000).
9. V. F. Boldyshev, E. A. Vinokurov, N. P. Merenkov, *et al.*, Fiz. Élem. Chastits At. Yadra **25**, 696 (1994) [Phys. Part. Nucl. **25**, 292 (1994)].
10. I. Endo and T. Kobayashi, Nucl. Instrum. Methods Phys. Res. A **328**, 517 (1993).
11. H. Olsen and L. C. Maximon, Phys. Rev. **114**, 887 (1959).
12. V. N. Baier, V. S. Fadin, and V. M. Katkov, *Emission of Relativistic Electrons* (Atomizdat, Moscow, 1973).
13. M. V. Galynskiĭ, L. F. Zhirkov, S. M. Sikach, *et al.*, Zh. Éksp. Teor. Fiz. **95**, 1921 (1989) [Sov. Phys. JETP **68**, 1111 (1989)]; M. V. Galynskiĭ and S. M. Sikach, Fiz. Élem. Chastits At. Yadra **29**, 1133 (1998) [Phys. Part. Nucl. **29**, 469 (1998)].
14. A. P. Potylitsyn, Nucl. Instrum. Methods Phys. Res. A **398**, 395 (1997).
15. J. Clendenin, *Recent Advances in Electron and Positron Sources*, SLAC-PUB-8465, 2000.
16. V. Balakin and A. A. Mikhailichenko, Preprint INP 79-85 (Institute of Nuclear Physics, Novosibirsk, 1979).
17. K. Dobashi *et al.*, Nucl. Instrum. Methods Phys. Res. A **437**, 169 (1999).
18. T. Kotseroglon, V. Bharadwaj, J. E. Clendenin, *et al.*, in *Proceedings of the 1999 PAC, New York, 1999*, p. 3450.
19. I. Sakai, T. Hirose, K. Dobaski, *et al.*, in *Proceedings of the 21st ICFA Workshop, Stony Brook, 2001*.

JETP Letters, Vol. 75, No. 9, 2002, pp. 457–460. Translated from Pis'ma v Zhurnal Éksperimental'noĭ i Teoreticheskoĭ Fiziki, Vol. 75, No. 9, 2002, pp. 547–550.

Influence of Striction Effects on the Multicritical Behavior of Homogeneous Systems

S. V. Belim

Omsk State University, Omsk, 644077 Russia

e-mail: belim@univer.omsk.su

Received March 20, 2002

A field-theoretical description of the behavior of homogeneous, elastically isotropic, compressible systems characterized by two order parameters at the bicritical and tetracritical points is presented. For three-dimensional Ising-like systems, a similar description is performed in the two-loop approximation in three dimensions with the use of the Padé–Borel summation technique. The renormalization group equations are analyzed, and fixed points corresponding to different types of multicritical behavior are determined. It is shown that the effect of elastic strains causes a change from a bicritical behavior to a tetracritical one and leads to the appearance of a wide variety of multicritical points. © *2002 MAIK "Nauka/Interperiodica".*

PACS numbers: 64.60.Kw; 64.60.Ak

Earlier, it was shown [1] that, because of striction effects, elastic strains lead to the appearance of multicritical points that are absent in the phase diagrams of corresponding incompressible substances.

The subject of this paper is the study of the influence of striction effects on systems whose phase diagrams already contain multicritical points of the bicritical or tricritical type. In the first case, a multicritical point corresponds to the intersection of two lines of second-order phase transitions and one line of first-order phase transitions, and in the second case, it corresponds to the intersection of four lines of second-order phase transitions. In the immediate vicinity of a multicritical point, the system exhibits a specific critical behavior characterized by the competition between different types of ordering. As a result, at a bicritical point, one critical parameter is displaced by another. A tetracritical point allows the existence of a mixed phase with the coexistence of different types of ordering. Such systems [2] can be described by introducing two order parameters that are transformed according to two irreducible representations.

In structural phase transitions that occur in the absence of the piezoelectric effect in the paraphase, elastic strains act as a secondary order parameter whose fluctuations are not critical in most cases [3]. Since, in the critical region, the main contribution to the striction effects comes from the dependence of the exchange integral on the distance, only elastically isotropic systems are considered in this paper.

The model Hamiltonian of the system has the form

$$H_0 = \int d^D x \Big[\frac{1}{2}(\tau_1 + \nabla^2)\Phi(x)^2 + \frac{1}{2}(\tau_1 + \nabla^2)\Psi(x)^2 + \frac{u_{10}}{4!}(\Phi(x)^2)^2 + \frac{u_{20}}{4!}(\Psi(x)^2)^2 + \frac{2u_{30}}{4!}(\Phi(x)\Psi(x))^2 + g_1 y(x)\Phi(x)^2 + g_2 y(x)\Psi(x)^2 + \beta y(x)^2 \Big]. \quad (1)$$

Here, $\Phi(x)$ and $\Psi(x)$ are the fluctuating order parameters; u_{01} and u_{02} are positive constants; $\tau_1 \sim |T - T_{c1}|/T_{c1}$ and $\tau_2 \sim |T - T_{c2}|/T_{c2}$, where T_{c1} and T_{c2} are the phase transition temperatures for the first- and second-order parameters, respectively; $y(x) = \sum_{\alpha=1}^{3} u_{\alpha\alpha}(x)$, where $u_{\alpha\beta}$ is the strain tensor; g_1 and g_2 are the quadratic striction parameters; β is a constant characterizing the elastic properties of the crystal; and D is the space dimension. In this Hamiltonian, integration with respect to the components that depend on the nonfluctuating variables, which do not interact with the order parameters, has already been already performed.

Changing to the Fourier transforms of the variables in Eq. (1), one obtains the Hamiltonian of the system in the form

$$H_0 = \frac{1}{2}\int d^D q(\tau_1 + q^2)\Phi_q \Phi_{-q} + \frac{1}{2}\int d^D q(\tau_2 + q^2)\Psi_q \Psi_{-q} + \frac{u_{01}}{4!}\int d^D q_i (\Phi_{q1}\Phi_{q2})(\Phi_{q3}\Phi_{-q1-q2-q3})$$

0021-3640/02/7509-0457$22.00

$$+\frac{u_{02}}{4!}\int d^D q_i(\Psi_{q1}\Psi_{q2})(\Psi_{q3}\Psi_{-q1-q2-q3})$$
$$+\frac{2u_{03}}{4!}\int d^D q_i(\Phi_{q1}\Phi_{q2})(\Psi_{q3}\Psi_{-q1-q2-q3})$$
$$+g_1\int d^D q y_{q1}\Phi_{q2}\Phi_{-q1-q2}$$
$$+g_2\int d^D q y_{q1}\Psi_{q2}\Psi_{-q1-q2}+\frac{g_1^2}{\Omega}y_0\int d^D q\Phi_q\Phi_{-q}$$
$$+\frac{g_2^0}{\Omega}y_0\int d^D q\Psi_q\Psi_{-q}+2\beta\int d^D q y_q y_{-q}+2\frac{\beta_0}{\Omega}y_0^2. \quad (2)$$

Here, the components y_0 describing uniform strains are separated. According to [1], such a separation is necessary, because the nonuniform strains y_q are responsible for the acoustic phonon exchange and lead to long-range interactions, which are absent for uniform strains.

Let us determine the effective Hamiltonian that depends on only the strongly fluctuating order parameters Φ and Ψ of the system as follows:

$$\exp\{-H[\Phi,\Psi]\} = B\int\exp\{-H_0[\Phi,\Psi,y]\}\prod dy_q. \quad (3)$$

If the experiment is performed at constant volume, the quantity y_0 is a constant, and the integration in Eq. (3) only goes over the nonuniform strains, while the uniform strains do not contribute to the effective Hamiltonian. In an experiment at constant pressure, the term $P\Omega$ is added to the Hamiltonian, with the volume being represented in terms of the strain tensor components in the form

$$\Omega = \Omega_0\left[1+\sum_{\alpha=1}u_{\alpha\alpha}+\sum_{\alpha\neq\beta}u_{\alpha\alpha}u_{\beta\beta}+O(u^3)\right] \quad (4)$$

and the integration in Eq. (3) also performed over the uniform strains. According to [4], the inclusion of quadratic terms in Eq. (4) may be important at high pressures and for crystals with strong striction effects. As a result, one obtains

$$H=\frac{1}{2}\int d^D q(\tau_1+q^2)\Phi_q\Phi_{-q}$$
$$+\frac{1}{2}\int d^D q(\tau_2+q^2)\Psi_q\Psi_{-q}$$
$$+\frac{v_{01}}{4!}\int d^D q_i(\Phi_{q1}\Phi_{q2})(\Phi_{q3}\Phi_{-q1-q2-q3})$$
$$+\frac{v_{02}}{4!}\int d^D q_i(\Psi_{q1}\Psi_{q2})(\Psi_{q3}\Psi_{-q1-q2-q3})$$
$$+\frac{2v_{03}}{4!}\int d^D q_i(\Phi_{q1}\Phi_{q2})(\Psi_{q3}\Psi_{-q1-q2-q3})$$
$$+\frac{z_1^2-w_1^2}{2}\int d^D q_i(\Phi_{q1}\Phi_{-q1})(\Phi_{q2}\Phi_{-q2})$$
$$+\frac{z_2^2-w_2^2}{2}\int d^D q_i(\Psi_{q1}\Psi_{-q1})(\Psi_{q2}\Psi_{-q2})$$
$$+(z_1z_2-w_1w_2)\int d^D q_i(\Phi_{q1}\Phi_{-q1})(\Psi_{q2}\Psi_{-q2}), \quad (5)$$

$$v_{01}=u_{01}-12z_1^2,\quad v_{02}=u_{02}-12z_2^2,$$
$$v_{03}=u_{03}-12z_1z_2,$$
$$z_1=\frac{g_1}{\sqrt{\beta}},\quad z_2=\frac{g_2}{\sqrt{\beta}},\quad w_1=\frac{g_1^0}{\sqrt{\beta_0}},\quad w_2=\frac{g_2^0}{\sqrt{\beta_0}}.$$

This Hamiltonian leads to a wide variety of multicritical points. As for incompressible systems, both tetracritical

$$(v_3+12(z_1z_2-w_1w_2))^2 < (v_1+12(z_1^2-w_1^2))(v_2+12(z_2^2-w_2^2))$$

and bicritical

$$(v_3+12(z_1z_2-w_1w_2))^2 \geq (v_1+12(z_1^2-w_1^2))(v_2+12(z_2^2-w_2^2))$$

behaviors are possible. In addition, the striction effects may give rise to multicritical points of higher orders.

In the framework of the field-theoretical approach [5], the asymptotic critical behavior and the structure of the phase diagram in the fluctuation region are determined by the Callan–Symanzik renormalization group equation for the vertex parts of the irreducible Green's functions. To calculate the β and γ functions as functions involved in the Callan–Symanzik equation for renormalized interaction vertices u_1, u_2, u_3, g_1, g_2, $g_1^{(0)}$, and $g_2^{(0)}$ or complex vertices z_1, z_2, w_1, w_2, v_1, v_2, and v_3, which are more convenient for the determination of the multicritical behavior, a standard method based on the Feynman diagram technique and on the renormalization procedure was used [6]. As a result, the following expressions were obtained for the β functions in the two-loop approximation:

$$\beta_{v1}=-v_1+\frac{n+8}{6}v_1^2+\frac{m}{6}v_3^2$$
$$-\frac{41n+190}{243}v_1^3-\frac{23m}{243}v_1v_3^2-\frac{2m}{27}v_3^3,$$
$$\beta_{v2}=-v_2+\frac{m+8}{6}v_2^2+\frac{n}{6}v_3^2$$

$$-\frac{41m+190}{243}v_2^3-\frac{23n}{243}v_2v_3^2-\frac{2n}{27}v_3^3,$$

$$\beta_{v3} = -v_1+\frac{2}{3}v_3^2+\frac{(n+2)}{6}v_1v_3+\frac{m+2}{6}v_2v_3$$
$$-\frac{5(n+m)+72}{486}v_3^3-\frac{23(n+1)}{486}v_1^2v_3$$
$$-\frac{23(m+2)}{486}v_2^2v_3-\frac{n+2}{9}v_1v_3^2-\frac{m+2}{9}v_2v_3^2,$$

$$\beta_{z1} = -z_1+\frac{n+2}{3}v_1z_1+2nz_1^3+2mz_1z_2^2+\frac{m}{3}v_3z_2$$
$$-\frac{23(n+2)}{243}v_1^2z_1-\frac{7m}{243}v_3^2z_1-\frac{2m}{27}v_3^2z_2, \qquad (6)$$

$$\beta_{z2} = -z_2+\frac{m+2}{3}v_2^2z_2+2mz_2^3+2nz_1^2z_2$$
$$+\frac{n}{3}v_3z_1-\frac{23(m+2)}{243}v_2^2z_2-\frac{7n}{243}v_3^2z_2-\frac{2n}{27}v_3^2z_1,$$

$$\beta_{w1} = -w_1+\frac{n+2}{3}v_1w_1+4nz_1^2w_1-2mw_1^3$$
$$+4mz_1z_2w_2-2mw_1w_2^2+\frac{m}{3}v_3w_2$$
$$-\frac{23(n+2)}{243}v_1^2w_1-\frac{7m}{243}v_3^2w_1-\frac{2m}{27}v_3^2w_2,$$

$$\beta_{w2} = -w_2+\frac{m+2}{3}v_2w_2+4mz_2^2w_2-2nw_2^3$$
$$+4nz_1z_2w_1-2nw_1^2w_2+\frac{n}{3}v_3w_1$$
$$-\frac{23(m+2)}{243}v_2^2w_2-\frac{7n}{243}v_3^2w_2-\frac{2n}{27}v_3^2w_1.$$

It is well known that the perturbative series expansions are asymptotic and the vertices of the interactions of the order parameter fluctuations in the fluctuation region are sufficiently large for Eqs. (6) to be directly applied. Therefore, to extract the necessary physical information from the expressions derived above, the Padé–Borel method generalized to the multiparameter case was used. The corresponding direct and inverse Borel transformations have the form

$$f(v1, v2, v3, z1, z2, w1, w2)$$
$$= \sum_{i_1,\ldots,i_7} c_{i_1\ldots i_7} v_1^{i_1}v_2^{i_2}v_3^{i_3}z_1^{i_4}z_2^{i_5}w_1^{i_6}w_2^{i_7} \qquad (7)$$
$$= \int_0^\infty e^{-t}F(v_1t, v_2t, v_3t, z_1t, z_2, w_1t, w_2t)dt,$$

$$F(v1, v2, v3, z1, z2, w1, w2)$$
$$= \sum_{i_1,\ldots,i_7} \frac{c_{i_1\ldots i_7}}{(i_1+\ldots+i_7)!}v_1^{i_1}v_2^{i_2}v_3^{i_3}z_1^{i_4}z_2^{i_5}w_1^{i_6}w_2^{i_7}. \qquad (8)$$

For the analytic continuation of the Borel transform of a function, a series in an auxiliary variable θ is introduced:

$$\tilde{F}(v_1, v_2, v_3, z_1, z_2, w_1, w_2, \theta)$$
$$= \sum_{k=0}^{\infty}\theta^k\sum_{i_1,\ldots,i_7}\frac{c_{i_1\ldots i_7}}{k!}v_1^{i_1}v_2^{i_2}v_3^{i_3}z_1^{i_4}z_2^{i_5}w_1^{i_6}w_2^{i_7}\delta_{i_1+\ldots+i_7,k}, \qquad (9)$$

and the [*L*/*M*] Padé approximation is applied to this series at the point θ = 1. This approach was proposed and tested in [7] for describing the critical behavior of systems characterized by several vertices of interaction of the order-parameter fluctuations. The property of the system retaining its symmetry when using the Padé approximants in variable θ is essential for the description of multivertex models.

In the two-loop approximation, the β functions were calculated using the [2/1] approximant. The character of critical behavior is determined by the existence of a stable fixed point satisfying the set of equations

$$\beta_i(v_1^*, v_2^*, v_3^*, z_1^*, z_2^*, w_1^*, w_2^*) = 0$$
$$(i = 1, \ldots, 7). \qquad (10)$$

The requirement that the fixed point be stable is reduced to the condition that the eigenvalues b_i of the matrix

$$\beta_{i,j} = \frac{\partial\beta_i(v_1^*, v_2^*, v_3^*, z_1^*, z_2^*, w_1^*, w_2^*)}{\partial v_j}$$
$$(v_i, v_j \equiv v_1^*, v_2^*, v_3^*, z_1^*, z_2^*, w_1^*, w_2^*) \qquad (11)$$

lie in the right complex half-plane.

The resulting set of resummed β functions contains a wide variety of fixed points lying in the physical region of the vertex values with $v_i \geq 0$.

A complete analysis of the fixed points, each of them corresponding to the critical behavior of a single order parameter, was presented in our recent publication [8]. Now, I consider the combined critical behavior of two order parameters.

The analysis of the values and stability of the fixed points offers a number of conclusions. The bicritical fixed point of an incompressible system (v_1 = 0.934982, v_2 = 0.934982, v_3 = 0.934982, z_1 = 0, z_2 = 0, w_1 = 0, w_2 = 0) is unstable under the effect of uniform strains (b_1 = 0.090, b_2 = 0.523, b_3 = 0.667, b_4 = 0.521, b_5 = 0.002, b_6 = 0.521, b_7 = 0.002). The striction effects lead to the stabilization of the tetracritical fixed point of a compressible system (v_1 = 0.934982, v_2 = 0.934982, v_3 = 0.934982, z_1 = 0, z_2 = 0, w_1 = 0, w_2 = 0, b_1 = 0.090,

$b_2 = 0.523$, $b_3 = 0.667$, $b_4 = 2.144$, $b_5 = 0.267$, $b_6 = 5.223$, $b_7 = 0.882$).

The stability of other multicritical points cannot be investigated in terms of the described model, because the calculations lead to a degenerate set of equations. The degeneracy is eliminated by considering the Hamiltonian with allowance for the terms of higher orders in both the strain tensor components and the fluctuating order parameters.

Thus, the striction-caused interaction of the fluctuating order parameters with elastic strains leads to the transition from the bicritical behavior to the tetracritical one and also to the appearance of new multicritical points with their own types of critical behavior in the phase diagram of the substance.

REFERENCES

1. A. I. Larkin and S. A. Pikin, Zh. Éksp. Teor. Fiz. **56**, 1664 (1969) [Sov. Phys. JETP **29**, 891 (1969)].
2. V. V. Prudnikov, P. V. Prudnikov, and A. A. Fedorenko, Fiz. Tverd. Tela (St. Petersburg) **42**, 158 (2000) [Phys. Solid State **42**, 165 (2000)].
3. Y. Imry, Phys. Rev. Lett. **33** (21), 1304 (1974).
4. D. J. Bergman and B. I. Halperin, Phys. Rev. B **13**, 2145 (1976).
5. D. Amit, *Field Theory the Renormalization Group and Critical Phenomena* (McGraw-Hill, New York, 1976).
6. J. Zinn-Justin, *Quantum Field Theory and Critical Phenomena* (Clarendon, Oxford, 1989).
7. S. A. Antonenko and A. I. Sokolov, Phys. Rev. B **49**, 15901 (1994); K. B. Varnashev and A. I. Sokolov, Fiz. Tverd. Tela (St. Petersburg) **38**, 3665 (1996) [Phys. Solid State **38**, 1996 (1996)]; A. I. Sokolov, K. B. Varnashev, and A. I. Mudrov, Int. J. Mod. Phys. B **12** (12/13), 1365 (1998); A. I. Sokolov and K. B. Varnashev, Phys. Rev. B **59** (13), 8363 (1999).
8. S. V. Belim and V. V. Prudnikov, Fiz. Tverd. Tela (St. Petersburg) **45**, 1299 (2001) [Phys. Solid State **43**, 1353 (2001)].

Translated by E. Golyamina

JETP Letters, Vol. 75, No. 9, 2002, pp. 461–464. From Pis'ma v Zhurnal Éksperimental'noĭ i Teoreticheskoĭ Fiziki, Vol. 75, No. 9, 2002, pp. 551–554.

Time-Resolved Nonlinear Surface Plasmon Optics[1]

Yu. E. Lozovik[1]*, S. P. Merkulova[1], M. M. Nazarov[2], A. P. Shkurinov[2], and P. Masselin[3]*****

[1] *Institute of Spectroscopy, Russian Academy of Sciences, Troitsk, Moscow region, 142190 Russia*
**e-mail: lozovik@isan.troitsk.ru*

[2] *Department of Physics and International Laser Center, Moscow State University, Moscow, 119899 Russia*
***e-mail: nazarov@sapphire.phys.msu.su*

[3] *Laboratoire de PhysicoChimie de l'Atmosphere, CNRS UMR 8101, Universite du Littoral, 59140 Dunkerque, France*
****e-mail: masselin@univ-littoral.fr*

Received March 27, 2002

A new surface-sensitive method of time-resolved optical studies is proposed. The method consists in the independent excitation of several surface electromagnetic waves (SEW) by two laser femtosecond pulse beams with varied time delay $\Delta\tau$ and distance Δr between corresponding excitation regions on the surface. To fulfill the phase-matching condition for plasmon–photon coupling, metal grating is used. Due to nonlinear plasmon interaction, the optical radiation with $\omega_1 + \omega_2$ and $2\omega_1 - \omega_2$ (where ω_1, ω_2 are corresponding laser beam frequencies) is generated. The intensity of this nonlinear response versus $\Delta\tau$ and Δr are studied. The direct measurements of the SEW temporal properties are presented. Experiments of this type are important for the development of femtosecond surface plasmon optics. © *2002 MAIK "Nauka/Interperiodica".*

PACS numbers: 42.65.Ky; 42.65.Hw; 73.20.Mf

The surface electromagnetic wave (SEW) is an effective tool for interface studies [1–4]. SEWs have various applications in matter diagnostics, nonlinear optics and spectroscopy. Many optical effects are difficult to observe, because of a weak nonlinear response or small amount of substance. To avoid this difficulty, one can concentrate laser radiation energy in space and time. The advantage of using SEW is the concentration of light energy near the interface. Special experimental geometry can be used to fulfill phase-matching condition for effective SEW excitation [1]. We use metal grating for this purpose. It is essential for nonlinear processes to have a high peak intensity, but the average field must be moderated, otherwise the sample will be damaged. Femtosecond laser pulses fit these requirements.

In this work, we suggest a new surface-sensitive method of time-resolved studies based on the use of an interacting SEW excited by two femtosecond laser beams with varying time delay and distance between corresponding excitation regions on the surface. This interaction leads to the generation of optical waves at a frequency equal to the second harmonic or the sum of frequencies of the incoming beams. The four-wave mixing (FWM) process $2\omega_1 - \omega_2$ is also investigated. We are mainly interested in the temporal behavior to demonstrate that time-resolved studies on a grating surface can potentially have temporal resolution of up to a few femtosecond. The sensitivity and selectivity to the properties of the surface are achieved with the second-harmonic (SHG) and sum-frequency generation (SFG) processes, because these processes are forbidden in the bulk of the isotropic medium [5, 6]. The results show that our method, based on the interaction of a noncollinear SEW, has femtosecond time resolution and many more possibilities for experimental realization in comparison with other surface-sensitive optical techniques [7–11].

We carried out experiments in the different geometries of incoming beams. A collinear scheme was used in the case of degenerate SFG. We demonstrated the possibility of noncollinear experiments by the example of degenerate and nondegenerate SFG and FWM.

The SEW is generated according to the relation $\mathbf{k}^{\omega}_{t,i} + n_i\mathbf{q} = \mathbf{K}^{\omega}_{\mathrm{SEW},i}$, where $i = 1, 2$ denote the beam number, $\mathbf{q} = 2\pi/d$ is the reciprocal lattice vector, d is the grating period, $\mathbf{k}_{t,i} = \mathbf{k}_i \sin\theta_i$ is the laser radiation wavevector projection on the grating plane, θ_i is the angle of incidence of the laser beam relative to the normal of the grating, and n_i is the diffraction order. $\mathbf{K}^{\omega}_{\mathrm{SEW},i}$ is the SEW wave vector (see Fig. 1).

The generated SEW waves radiate waves at the combination optical frequency if phase-matching conditions for optical waves at frequencies ω_1 and ω_2 are satisfied simultaneously with the relation between the interacting SEW wave vectors: $\mathbf{K}^{\omega_1}_{\mathrm{SEW},1} + \mathbf{K}^{\omega_1}_{\mathrm{SEW},2} + n_3\mathbf{q} = \mathbf{k}^{\omega_1+\omega_2}_{t,3}$ for nondegenerate SFG and $2\mathbf{K}^{\omega_1}_{\mathrm{SEW},1} - \mathbf{K}^{\omega_1}_{\mathrm{SEW},2} \pm \mathbf{q} = \mathbf{k}^{2\omega_1-\omega_2}_{t,3}$ for the FWM process. Figure 1

[1] This article was submitted by the authors in English.

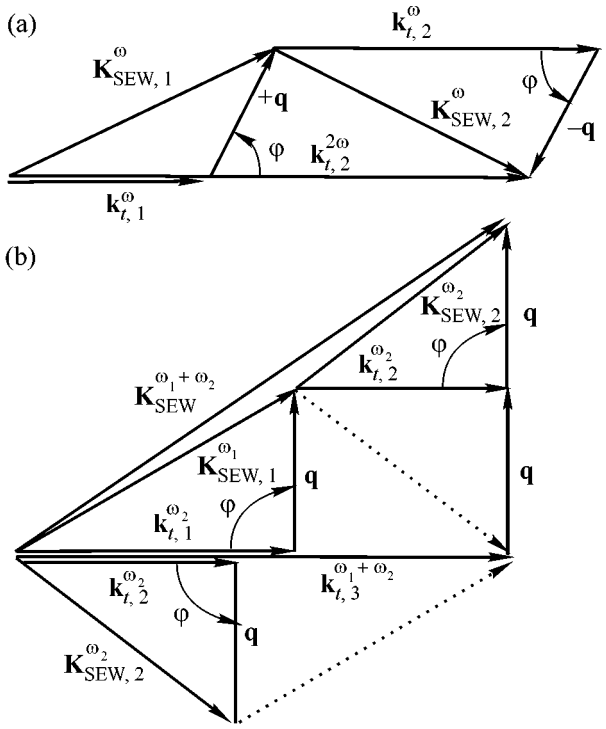

Fig. 1. (a) Wave vector arrangement at grating surface for SFG. Simultaneous excitation of two SEWs of one frequency (degenerate) in different directions (noncollinear). The sets of angles are $\varphi = 83°$, $\theta_1 = 42°$, $\theta_1 = 59°$. (b) Arrangement of wave vectors at grating surface. Simultaneous excitation of several SEWs of two frequencies (nondegenerate) in symmetric geometry in different directions (noncollinear). Angle values are $\varphi = \pm 90°$, $\theta_1 = 66°$, $\theta_1 = 52°$.

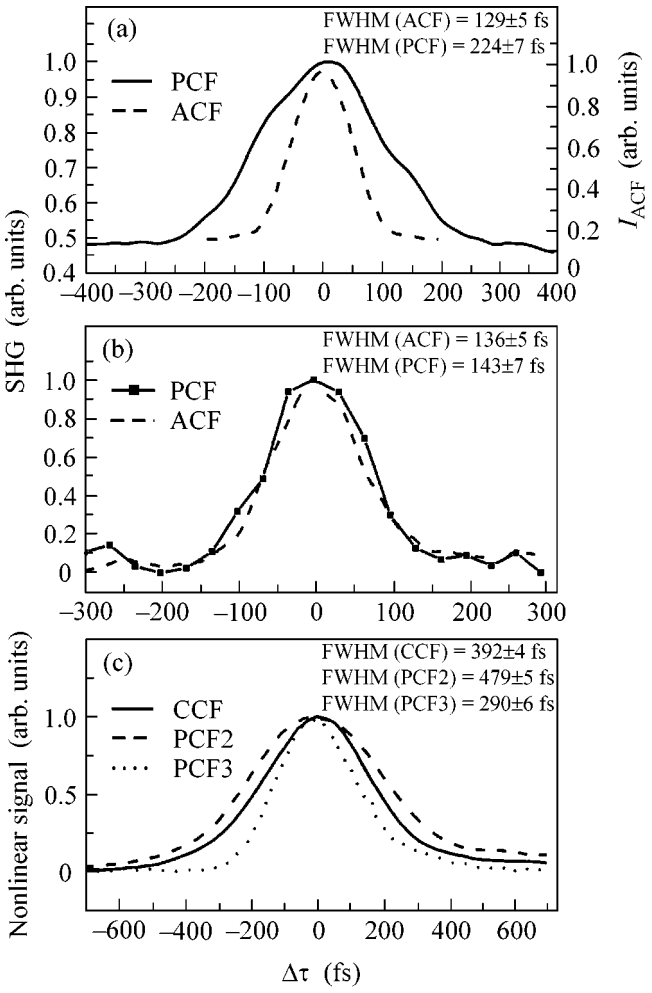

Fig. 2. Correlation functions of SFG enhanced by SEW. (a) Autocorrelation function for laser radiation ACF (λ = 760 nm) and plasmon correlation function PCF for the degenerate symmetric case. (b) The same as (a) for the degenerate noncollinear nonsymmetrical case. (c) Cross-correlation function for laser radiations CCF (λ_1 = 690 nm and λ_2 = 812 nm) and plasmon correlation function for the SFG PCF2 and FWM-PCF nondegenerate symmetric case: $\varphi = \pm 90°$, $\theta_1 = 66°$, $\theta_1 = 52°$.

depicts the vectorial layout for degenerate noncollinear (Fig. 1a) and nondegenerate collinear SFG (Fig. 1b). Note that in Fig. 1 the angle φ represents the angle between the optical wave vector and the reciprocal lattice vector of grating. Figure 1b demonstrates that proper choice of angles φ and θ leads to simultaneous satisfaction of the phase-matching condition of surface plasmon excitation and the nonlinear process. We highlight that, when φ is equal to 90 degrees (symmetric case), excitation of two SEWs with wave vectors $\mathbf{k}^{\omega}_{t} + \mathbf{q}$ and $\mathbf{k}^{\omega}_{t} - \mathbf{q}$, respectively, takes place simultaneously.

First, we describe the case of interaction of a two collinear plasmon in the symmetric scheme ($\varphi = 90°$) with $\omega_1 = \omega_2 = \omega$. We measure the emission of the signal at frequency 2ω and compare it with the autocorrelation function (ACF) of the fundamental beams. The results are presented in Fig. 2a. Each beam at the fundamental frequency radiates at the frequency 2ω via the SHG process and, as a consequence, the recorded signal is nonzero for large delay between pulses. When spatial and temporal overlap of the pulses occurs, the degenerate collinear SFG wave is radiated in the specular direction. The SFG is recorded as a function of delay (plasmon correlation function PCF). This experimental scheme is the same as for an autocorrelator.

We performed the same experiment in a noncollinear geometry, and the results are presented in Fig. 2b. In this geometry, the SHG from each beam and the degenerate SFG occur. SFG wave-vector projection on the surface is $\mathbf{k}^{2\omega}_{t,3} = \mathbf{K}^{\omega}_{\mathrm{SEW},1} + \mathbf{K}^{\omega}_{\mathrm{SEW},2}$, and then the SFG signal emission occurs in the direction $\theta_3 \approx (\theta_1 + \theta_2)/2$ [10] different from θ_1 and θ_2. The recorded signal is then background-free. The angles of the grating groove orientation are chosen to be the same for both beams, $\varphi_1 = \varphi_2 = 83°$, and all incident and reflected

beams lie in the incidence plane. The value of θ_1 and θ_2 are set in such a way so as to excite simultaneously two SEWs according to our grating parameters (Fig. 1a).

We also realized noncollinear nondegenerate SFG and FWM with two synchronized femtosecond laser beams with different frequencies. The symmetric scheme was used for both beams with frequencies ω_1 and ω_2, as in the degenerate collinear scheme. Beams had different incidence angles, as in the degenerate noncollinear scheme. To characterize laser pulses, we used the cross-correlation function (CCF) of beam 1 and beam 2 pulses.

Note that, for the described experiments, the characteristic length of the SEW path is of the same order as radii of the excitation spot (15 μm) on the surface. The SEW propagation length l_{pl} and lifetime τ_{pl} are coupled through plasmon velocity $v = 0.9c$, where c is the speed of light.

For SEW excitation, we observe four nonlinear signals $2\omega_1$, $2\omega_2$, $\omega_1 + \omega_2$, $2\omega_1 - \omega_2$ separated in frequencies and in the radiation emission angle (see Fig. 3). Note that the $2\omega_1 - \omega_2$ process is of a different nature; it is a third-order nonlinear process, and its efficiency is determined by $\chi^{(3)}$ and not by $\chi^{(2)}$, where $\chi^{(2)}$ and $\chi^{(3)}$ are the corresponding nonlinear susceptibility tensors. The properties such as the spectral width, pulse duration, and the polarization direction for FWM proved to be different from the second-order processes—SHG, SFG—under our experimental conditions. Frequency combination is the same as in the well-known CARS (coherent anti-stokes Raman scattering) process. Although we do not have resonance with media at the frequency $\omega_1 - \omega_2$ in our case, the signal intensity is rather high. Indeed, the absolute FWM intensity is higher than for SFG or SHG. This can occur because the $\chi^{(3)}$ electric-dipole tensor has nonzero components in the bulk, in contrast to $\chi^{(2)}$. The results of measurements are shown in Fig. 2c as PCF 2 for SFG and PCF 3 for FWM process. Note that the duration of ACF is $\sqrt{2}$ times larger than the pulse duration. For the FWM process, however, the duration of PCF 3 is $\sqrt{3/2}$ times less than the pulse duration, because of the difference in the order of the process. The PCF signal is the cross correlation of SEW_1 and SEW_2 fields. In turn, the SEW field is a convolution of the plasmon lifetime τ_{pl} and laser pulse duration. From the comparison of ACF and PCF duration, it is possible to obtain the plasmon lifetime. In the symmetric (collinear and degenerate) SFG case (Fig. 2a), the measured SEW lifetime was found to be 70 fs. For the nonsymmetrical case (noncollinear and degenerate) (Fig. 2b), this lifetime decreases to 20 fs. For the nondegenerate symmetric noncollinear case, the SEW lifetime (60 fs) is smaller than in the degenerate symmetric case, due to higher SEW absorption at frequency ω_2. However, it is greater than in the nonsymmetrical case. As seen from Fig. 2b, the traces

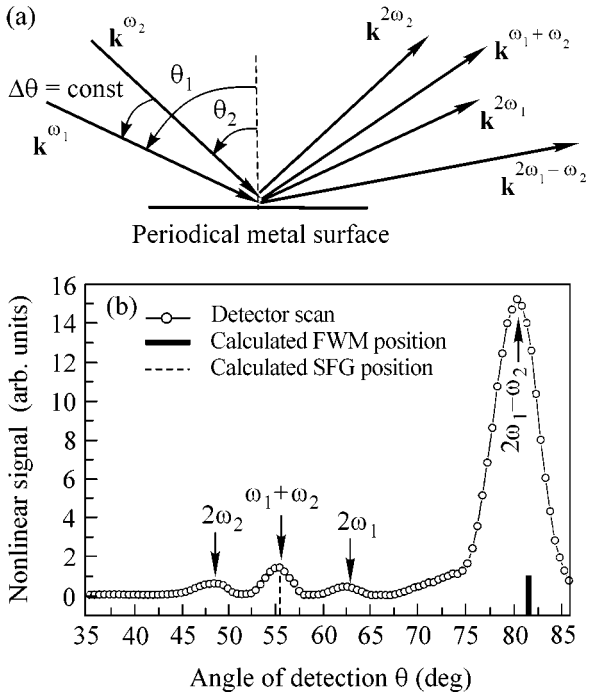

Fig. 3. (a) Wave-vector arrangement in the incidence plane for the nondegenerate symmetric case. (b) Angle distribution of nonlinear signal radiation in the incidence plane.

overlap in the case of noncollinear and degenerated SFG, demonstrating that the lifetime is much shorter than in the other case of interaction. This increase in the SEW lifetime in the symmetric case can be connected with the modification of SEW properties due to the Bragg reflection of SEW from the grating grooves.

The nonlinear signal intensity distribution vs. reflection angle θ is presented in Fig. 3b for the nondegenerate geometry. All beams lie in the incidence plane. The angle of nonlinear signal radiation defined by the phase-matching condition agrees well with the experimental data.

As plasmon propagates on the metal surface, it exponentially decays (in time and space) through several channels: ohmic losses, radiation damping, and Landau damping.

Besides the fact that the metal is also in the nonequilibrium state after SEW excitation and absorption, the electron relaxation can manifest itself in measured values [11–13].

In principle, in time-resolved SEW experiments it is possible to observe not only the SEW lifetime, but also the interface relaxation time through the processes described above if a parameter of the nonlinear process depends essentially on the temperature or distribution of metal electrons. With our experimental conditions, we did not observe the influence of medium temperature on $\chi^{(2)}$ within a relative accuracy of 5%.

For the wavelength of 780 nm in gold, the SEW maximal propagation length restricted by ohmic losses is only 40 μm, which would correspond to a SEW lifetime of 130 fs. At the sum frequency, the same parameters are, accordingly, 1.3 μm and 3 fs. However, for the difference frequency generation (DFG) (mid and far IR), the propagation length can be much larger (500 μm for $\lambda = 10$ μm). The suggested method allows the DFG enhancement by SEW, which can be useful for IR surface time-resolved spectroscopy.

In conclusion, the method of femtosecond surface-plasmon spectroscopy has been suggested and experimentally demonstrated. It is based on the resonance excitation of several surface SEWs by femtosecond synchronized laser beams. These SEWs interact at the surface, allowing one to enhance various nonlinear optical effects sensitive to the surface properties. This was demonstrated in this work by the sum-frequency generation and four-wave mixing process. The nonlinear optical response originating from the interacting SEWs reflects the spatial and temporal behavior of these SEWs. As an example, we measured the SEW lifetime at the surface of gold grating, which proved to be 60 fs for the symmetric case and less than 20 fs for the nonsymmetrical case. For the first time, we observed simultaneously SHG, SFG, and FWM enhanced by the SEW on grating. The described experiments open up the practical possibility for the development of time-resolved femtosecond surface plasmon optics and spectroscopy.

We thank Yu.P. Strelnikov for the fabrication of gratings and A.V. Balakin and I.O. Ozherelov for assistance in the experiments. The work was supported by the Russian Foundation for Basic Research.

REFERENCES

1. V. M. Agranovich and D. L. Mills: *Surface Polaritons: Electromagnetic Waves at Surfaces and Interfaces*, Ed. by V. M. Agranovich and D. L. Mills (North-Holland, Amsterdam, 1982; Nauka, Moscow, 1985).
2. Yu. E. Lozovik and A. V. Klyuchnik, in *Dielectric Susceptibility*, Ed. by L. V. Keldysh, D. A. Kirzhnits, and A. A. Maradudin (North-Holland, Amsterdam, 1987).
3. A. V. Balakin, A. A. Goncharov, N. I. Koroteev, *et al.*, Nonlinear Opt. **23**, 331 (2000).
4. S. I. Bojevolnyi, I. I. Smolianinov, and A. V. Zayatz, Phys. Rev. B **51**, 17916 (1995).
5. R. Reinisch, M. Niviere, H. Akhouayri, *et al.*, Opt. Eng. **27**, 961 (1988).
6. A. A. Angeluts, A. A. Goncharov, N. I. Koroteev, *et al.*, Quantum Electron. **24**, 67 (1997).
7. E. W. M. van der Ham, Q. H. F Vrehen, E. R. Eliel, *et al.*, J. Opt. Soc. Am. B **16**, 1146 (1999).
8. C. K. Chen, A. R. B. de Castro, Y. R. Shen, *et al.*, Phys. Rev. Lett. **43**, 946 (1979).
9. K. Katayama, T. Sawada, Q. Shen, *et al.*, Phys. Rev. B **58**, 8428 (1998).
10. Yu. E. Lozovik, S. P. Merkulova, M. M. Nazarov, *et al.*, Phys. Lett. A **276**, 127 (2000).
11. R. H. M. Groeneveld, R. Sprik, and A. Lagendijk, Phys. Rev. B **51**, 11433 (1995).
12. V. F. Gantmakher and Y. B. Levinson, *Carrier Scattering in Metals and Semiconductors* (Nauka, Moscow, 1984; North-Holland, New York, 1987).
13. Yu. E. Lozovik, S. A. Kovalenko, A. L. Dobryakov, *et al.*, Laser Phys. **9**, 557 (1999).

JETP Letters, Vol. 75, No. 9, 2002, pp. 465–469. Translated from Pis'ma v Zhurnal Éksperimental'noĭ i Teoreticheskoĭ Fiziki, Vol. 75, No. 9, 2002, pp. 555–559.

Induction Kinetics in 2D Electron Systems at the Hall Plateaus

V. B. Shikin

Institute of Solid State Physics, Russian Academy of Sciences, Chernogolovka, Moscow region, 142432 Russia

Received March 18, 2002; in final form, March 28, 2002

Specific features of the induction excitation of 2D electron systems at the Hall plateaus are discussed. The corresponding kinetics is shown to have several frequency regimes. In the region $\omega \gg \omega_D$, where ω_D is the frequency characteristic of the kinetics at the Hall plateaus, an induction-caused variation of electron density follows the magnetic-field variation with time. For the frequencies $\omega \leq \omega_D$, a noticeable relaxation of the electron disturbance appears, and the induction polarization of 2D samples at the Hall plateaus noticeably decreases as compared to the maximum possible polarization. Finally, in the limit $\omega \leq \omega_{slow}$, where ω_{slow} corresponds to another characteristic time of the quantum Hall effect, the so-called adiabatic approximation takes place with the 2D system responding to the derivative of magnetic field dH/dt rather than to the magnetic field itself $H(t)$. The results of calculations are compared with the experimental data reported in the literature. © *2002 MAIK "Nauka/Interperiodica".*

PACS numbers: 71.10.Pm; 73.43.Cd

Induction effects in an alternating magnetic field oriented normally to the plane of a 2D electron system are usually parasitic and require considerable (and not always successful) efforts for their elimination. However, recently, the induction effects were found to be useful for testing some fundamental concepts of the theory of the quantum Hall effect (QHE). It has been shown [1–3] that the QHE can also occur without the participation of the edge states. In the cited papers, it was also noted that, as in the case of the resistivity in the QHE regime, the magnetic-field dependence of the conductivity tensor exhibits characteristic quantum plateaus. Experiments [4] were carried out to test the Laughlin adiabatic hypothesis [5]. The problem of the induction states at the Hall plateaus is of interest by itself, because practically all measurements connected with the determination of the behavior of 2D systems in a magnetic field deal with the induction-caused excitation of the 2D system, while no comprehensive description of the consequences of this excitation is yet available. Below, this problem is considered for a single, infinitely long strip of width $2w$ in a magnetic field. Besides being interesting by itself (as was mentioned above), the model under consideration gives insight into the properties of a Corbino ring in the conditions

$$R_2 - R_1/(R_2 + R_1) \ll 1, \quad R_2 - R_1 = 2w, \qquad (1)$$

where R_2 and R_1 are the outer and inner radii of the ring.

1. Let us first consider the auxiliary problem of a 2D heterostructure in the form of a strip of width $2w$ with the separation $2d$ between the conducting system and the donor layer of density n_d in the absence of a magnetic field. The electron density in this system has the form

$$n(x) = n_d + \delta n(x), \qquad (2)$$

$$\delta n(x) = \frac{n_d}{\sqrt{w^2 - x^2}} \int_{-w}^{+w} \frac{\sqrt{w^2 - s^2}}{x - s} \Phi(s) ds + \frac{C}{\sqrt{w^2 - x^2}}, \qquad (3)$$

$$\Phi(x) = \ln\frac{w + x}{w - x} - \ln\sqrt{\frac{(w + x)^2 + 4d^2}{(w - x)^2 + 4d^2}},$$

$$\int_{-w}^{+\infty} \delta n(s) ds = 0. \qquad (4)$$

The constant C is determined from condition (4). The general form of $\delta n(x)$ is shown in the figure.

The profile of $\delta n(x)$ varies as a function of the magnetic field oriented normally to the plane of the heterostructure and remains symmetric about the plate center under the condition that the average density of the 2D system is assumed to be equilibrium. The sensitivity to the magnetic field grows with decreasing ratio $T/\hbar\omega_c$ (where T is the temperature and ω_c is the cyclotron frequency), while the diagonal conductivity along the 2D system simultaneously decreases exponentially. As a result, the electron density distortion due to the induction effect (which is always present in conducting systems with a time-dependent magnetic field) ceases being compensated by the diagonal component of the

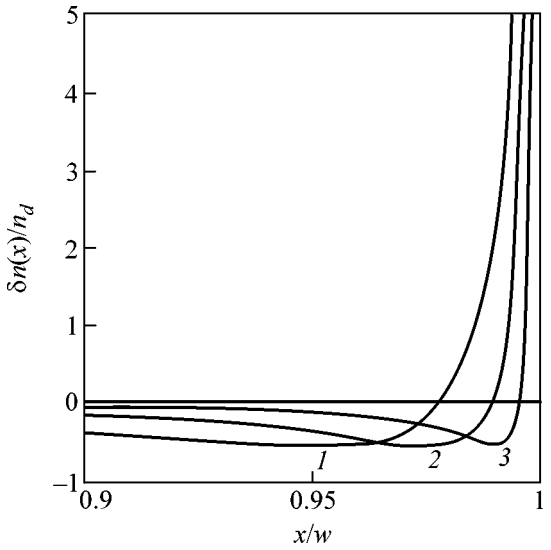

Distribution $\delta n(x)$ from Eq. (2) near one of the edges of a heterostructure with d/w = (*1*) 0.05, (*2*) 0.25, and (*3*) 0.01.

current, and the aforementioned symmetry of the 2D system is violated. In practice, attempts are usually undertaken to avoid this parasitic effect, e.g., by reducing the size of the 2D samples (see [6]) or by using an additional tunneling channel to provide the relaxation of the perturbed density at its equilibrium value [7, 8]. However, in recent years, a trend has been shown toward special studies of the induction phenomena at the Hall plateaus [1–4, 9].

2. For definiteness, let us consider the interesting publication [9], where a weak periodic induction-caused perturbation of an unscreened Corbino ring, together with a constant magnetic-field component that provides the appearance of quantum states give rise to a measurable oscillating charge between the ring edges at the Hall plateau. The presence of this charge is not unexpected. For example, a successful attempt to excite inductively the transverse magnetoplasmons in a system of parallel strips was reported in [10]. However, the experiment [9] mentioned above deserves special attention for the following reasons. Firstly, in a wide range of low (compared to the plasma) frequencies, the voltage measured between the ring edges does not depend on the induction excitation frequency. In addition, in the region $\omega \le \omega_D$ [$\omega_D \sim 100$ Hz, and the formal definition of ω_D is given below; see Eq. (13)], this voltage monotonically decreases with decreasing excitation frequency. Both these facts require a self-consistent interpretation.

The first effect can be explained within the framework of the phenomenological approach proposed by the authors of the cited publication [9] if we assume that the voltage between the ring edges is proportional to the degree of its charge polarization (Coulomb dipole moment) under the effect of induction forces {see Eq. (3) in [9]}. These authors correctly assume (as in [1–5]) that, at the plateau, the dipole moment of the ring is formed by the induction component of the radial current excited by the alternating magnetic field and does not contain a dissipative part of this component, which partially restores the homogeneity of the 2D system. Taking into account the explicit form of ac magnetic-field-induced electron-density variation $\delta n_i(t)$ along the integer part of the plate under the conditions $\sigma_{xx} \longrightarrow 0$ (see [1–4]),

$$\delta n_i(t) = -\sigma_{xy}\delta H(t)/ec = -el\delta H(t)/hc, \quad l = 1, 2, 3, \ldots, \tag{5}$$

and the necessity of retaining the total number of "shifted" electrons [see condition (4)], the total distribution of δn_o in our model should be chosen to have a Γ shape:

$$\delta n_o(x) = \begin{cases} -\delta n_i, & -w < x < +w - a \\ +\delta n_i w - a/a, & +w - a < x < +w, \end{cases} \tag{6}$$

where the edge width a has a characteristic scale d and varies within narrow limits about its own geometric value (see figure). For definiteness, we assume that the maximum of δn_o is at the right end of the plate. In Eq. (5), l is an integer and $\delta H(t)$ is the magnetic-field variation measured from the onset of the cutoff situation $\sigma_{xx} \longrightarrow 0$. We also assume that the conductivity σ_{xy}, whose explicit form is used in Eq. (5), remains constant over the whole interval of magnetic-field variation within the Hall plateau region.

Evidently, the charge distribution defined by Eq. (6) (as well as the voltage measured between the ring edges) possesses a dipole moment that is independent of the frequency of the exciting signal. This property of distribution (6) accounts for the absence of sensitivity to the frequency of measured signal [9] over a wide frequency range (10^2–10^4 Hz).

It is worthy of note that the density variation given by Eq. (5) does not disturb the filling factor $\delta\nu$ in the main part of the ring (plate). This follows from the definition of ν:

$$\nu = \pi(n_o + \delta n_i)l_H^2, \quad l_H^2 = 2c\hbar/e(H_o + \delta H),$$
$$\nu = \nu_l(1 + \delta H/H_o)(1 + \delta H/H_o)^{-1} \equiv \nu_l, \tag{7}$$
$$\nu_l = \frac{n_o ch}{eH_o} = l \quad (l = 1, 2, 3).$$

Thus, the induction-caused perturbation of the 2D system does not affect its integer state (in its main part away from the boundaries).

3. The induction density disturbance (6) constructed "by hand" inevitably contains a spatial inhomogeneity, and the 2D system tends to smooth it out in all possible ways. One of these possibilities is associated with vor-

tex currents generating their own magnetic field. Knowing the vortex electric field produced by the field $\dot{H}$, the value of σ_{xy}, and the inductance of the ring, one can easily estimate the scale of the additional magnetic flux Φ_J through the disk opening. Divided by the initial flux Φ_o, this flux has the scale

$$\Phi_s/\Phi_o = \alpha\frac{i\omega w}{2\pi c} \ll 1, \quad \alpha = e^2/(\hbar c) = 1/137.$$

Clearly, this channel of "smoothing out" the density gradients is insignificant, at least, for the parameters $2w \le 1$ cm and $\omega \le 10^4$ Hz used in [9].

The electric potential $\varphi(x)$ is absent in distribution (6). To estimate its role in the behavior of $\delta n(x)$, it is necessary to analyze the continuity equation with the boundary condition of no current through the boundaries of the strip.

In the equation itself, it is convenient to separate the vortex part:

$$\begin{gathered} e\partial n/\partial t - \sigma_{xy}c^{-1}\partial H/\partial t + \partial j_x/\partial x = 0, \\ ej_x = \sigma_{xx}\partial\mu/\partial x, \\ \sigma_{xx} \simeq \sigma_{xx}^{\text{peak}}\exp(-\hbar\omega_c/2T), \quad \sigma_{xx}^{\text{peak}} = e^2/2\pi\hbar. \end{gathered} \tag{8}$$

Here, μ is the electrochemical potential of the 2D electron gas in a magnetic field

$$\mu(x) = e\varphi(x) - T\ln S(H, T, \nu(x)), \tag{9}$$

where

$$\begin{gathered} 2S(H, T, \nu) = \left(\frac{1}{\nu} - 1\right) + \left[\left(\frac{1}{\nu} - 1\right)^2 + 4\epsilon\left(\frac{2}{\nu} - 1\right)\right]^{1/2}, \\ \epsilon = \exp(-\hbar\omega_c/T) \ll 1, \\ \nu < 2, \quad \nu(x) = \pi l_H^2 n(x), \quad l_H^2 = 2c\hbar/eH, \end{gathered} \tag{10}$$

and $\varphi(x)$ is the electric potential. Expressions (9) and (10) originate from the common relation between the electron density and the electrochemical potential μ (see, e.g., [11]) for a spinless ideal 2D electron system in a magnetic field at nonzero temperatures (to avoid the problems with a fractional QHE). If, in this case, the general formula involving the summation over all Landau levels is restricted to the two first terms (the ground level and the first excited level), it will be possible to invert the expression of the form

$$\nu(x) = \sum_{l=0}^{+\infty} f(\epsilon_l + e\varphi(x) - \mu(x))$$

[$f(z)$ is the Fermi function] with respect to the function $\mu(x)$, as is accomplished in definitions (9) and (10). The expression $-T\ln S(H, T, \nu)$ as a function of ν contains a jump $\hbar\omega_c$ in the vicinity of $\nu = 1$, and the sharpness of this jump increases with decreasing temperature.

In view of the aforesaid, one can conclude that, near the integer filling factors (specifically, near $\nu = 1$), the major contribution to $\nabla\mu$ comes from the "chemical component" $T\ln S(\nu)$. In fact, one has

$$\frac{\partial\mu}{\partial x} = e\frac{\partial\varphi}{\partial x} - \frac{T}{S}\frac{\partial S}{\partial\nu}\frac{\partial\nu}{\partial x}. \tag{11}$$

In the vicinity of $\nu \longrightarrow 1$, with allowance for relation (10), Eq. (11) is reduced to

$$\frac{\partial\mu}{\partial x} = e\frac{\partial\varphi}{\partial x} + \frac{T}{2\epsilon^{1/2}}\frac{\partial\nu}{\partial x}. \tag{11a}$$

According to Eq. (11a), at the Hall plateaus the second (diffusion) term exponentially (when $\epsilon \longrightarrow 0$) predominates over the first term. In view of this fact, Eq. (8) can be recast as follows:

$$\begin{gathered} e\partial n/\partial t - \sigma_{xy}c^{-1}\partial H/\partial t = +eD\partial^2 n/\partial x^2, \\ D = \pi l_H^2 T\sigma_{xx}^{\text{peak}}/e^2, \quad \sigma_{xx}^{\text{peak}} \simeq e^2/2\pi\hbar \end{gathered} \tag{12}$$

or

$$D \simeq l_H^2 T/\hbar. \tag{12a}$$

In Eq. (12), not only is the field term ignored [by virtue of Eq. (11a)], but also the exponents are cancelled; one of them, $\exp(-\hbar\omega_c/2T)$, is involved in the definition of σ_{xx} at the Hall plateaus and the other appears in calculations (11), (11a) of the derivative $\partial\ln S/\partial\nu$. As a result of the exponent cancellation, the diffusion coefficient (12a) proves to depend on T according to a power law.

For a strip of width $2w \sim 0.1$ cm at the temperature $T \le 0.3$ K in a magnetic field ~10 T, the characteristic time is

$$\tau_D \sim w^2/D \simeq 0.1 \text{ s}. \tag{13}$$

This time correlates with the characteristic scales of the transition region observed in [9] (see the discussion below).

The analysis of Eq. (12), in combination with the boundary condition of no current through the strip boundaries, allows one to determine more precisely the situation near the boundary with an increased electron density. Pursuing only qualitative inferences, we limit our consideration to one (e.g., right) edge of the ring. It is also convenient to separate the inhomogeneous part $\delta n_i(t)$ in the general solution:

$$n(x, t) - n_d = \delta n_i(t) + \delta n(x, t). \tag{14}$$

The remaining problem is reduced to the determination of $\delta n(x, t)$ from the equation

$$\begin{gathered} ie\omega\delta n = eDd^2\delta n/dx^2, \\ \delta n(x, t) = \delta n(x)\exp(i\omega t), \end{gathered} \tag{15}$$

with the boundary conditions

$$\begin{gathered} \delta n(-\infty, t) \longrightarrow 0, \\ \sigma_{xy}E_y - D\delta n'(0, t) = 0, \quad E_y = 2i\omega Hw/c. \end{gathered} \tag{16}$$

The solution to the problem given by Eqs. (15) and (16) has the form

$$\delta n(x) = \delta n_o \exp(x/\lambda), \quad \lambda^2 = i\omega/D, \tag{17}$$

$$\delta n_o = \sigma_{xy} E_y/(\lambda D) \simeq \delta n_i \lambda w, \tag{18}$$

where δn_i is determined by Eq. (5) and $-\infty < x \le 0$.

Expression (18) yields the level of Coulomb polarization of the sample in the transition region. As the frequency increases, when $\lambda^{-1} \le a$, asymptotic behavior of (18) takes the form of Eq. (6).

4. Definitions (18), (13), and (12a) do not exhaust the specific features of kinetics of a 2D system at the Hall plateaus. When $\omega \longrightarrow 0$, one more transition region is formed with the characteristic time τ_{slow}, in which the response of the 2D system is proportional to H/t rather than to $H(t)$. Its presence is easily revealed in the induction kinetics of the normal 2D state and is transferred, by analogy, to the case of QHE.

In the "normal" region in the presence of an induction-caused perturbation, Eq. (8) takes the form

$$e\partial n/\partial t - \sigma_{xy} c^{-1} \partial H/\partial t = +\sigma_{xx}^{peak} \partial^2 \varphi(x)/\partial x^2. \tag{19}$$

Let us first assume that the induction perturbation is stationary ($\partial H/\partial t$ = const; this type of excitation is used in [1–4]). In this case, Eq. (19) has a stationary solution, which follows from the relation

$$\sigma_{xy} c^{-1} \partial H/\partial t = -\sigma_{xx}^{peak} \partial^2 \varphi(x)/\partial x^2, \quad \partial n/\partial t = 0, \tag{20}$$

and means that the 2D system, while being distorted, completely shunts the induction effect (div$\mathbf{j} = 0$).

Relation (20) is (with allowance for the Poisson equation) an integral equation with respect to the distribution δn_{stat} providing the stationary character of the problem. Clearly, this distribution is proportional to $\partial H/\partial t \equiv \dot{H}$ rather than to $H(t)$:

$$\delta n_{stat} = \frac{\kappa w}{2\pi e c} \frac{\sigma_{xy}}{\sigma_{xx}} \frac{\dot{H}}{\sqrt{1-\xi^2}} [\xi^2 - (\xi + 1)/2], \quad \xi = x/w. \tag{21}$$

At finite but relatively low frequencies $\omega \ll \omega_{fast}$, the distribution δn_{stat} adiabatically retains its meaning of main density disturbance. Indeed, assuming that

$$\delta n = \delta n_{stat} + \delta n_1 + \ldots \tag{22}$$

and substituting this series in Eq. (19), one obtains the following relations for δn_1:

$$\frac{e\partial n_{stat}}{\partial t} = +\frac{\sigma_{xx}^{peak} \partial \varphi_1'(x)}{\partial x}, \quad \varphi_1'(x) = \frac{2e}{\kappa} \int_{-w}^{+w} \frac{\delta n_1(s) ds}{s - x}. \tag{23}$$

For the addition δn_1, one has $\delta n_1 \ll \delta n_{stat}$ if

$$\omega \ll \omega_{fast}, \quad \omega_{fast} \sim \tau_{fast}^{-1}, \quad \tau_{fast} \sim w/\sigma_{xx}^{peak}, \quad \sigma_{xx}^{peak} = e^2/(2\pi\hbar). \tag{24}$$

Similar considerations are valid for the Hall plateaus. In this case, the steady-state adiabatic solution is determined by the equation

$$\sigma_{xy} c^{-1} \dot{H} = \sigma_{xx} [\partial^2 \varphi(x)/\partial x^2 - T\partial^2 \ln S/\partial x^2], \quad \sigma_{xx} = \sigma_{xx} \exp -(\hbar\omega_c/2T). \tag{25}$$

It is established at frequencies

$$\omega \ll \omega_{slow}, \quad \omega_{slow} \sim \tau_{slow}^{-1}, \quad \tau_{slow} \sim \tau_{fast} \exp(+\hbar\omega_c/2T). \tag{26}$$

The time τ_{slow} corresponds to the interpretation of the low-frequency boundary in [9] and has the characteristic scale $\tau_{slow} \sim w/\sigma_{xx}$, where $\sigma_{xx} \simeq \sigma_{xx}^{peak} \exp(-\hbar\omega_c/2T)$. When $\hbar\omega_c/2T \le 100$, this time is $\tau_{slow} \gg \tau_D$.

Thus, the induction dynamics of 2D systems at the Hall plateaus under the conditions $\sigma_{xx} \longrightarrow 0$ is accompanied by the relaxation processes that smooth out the induction-caused spatial inhomogeneity of the 2D system. The specific diffusion kinetics that occurs at frequencies $\omega_{slow} \ll \omega \le \omega_D$, for which the oscillating charge is proportional to $\propto H(t)$, is characterized by the relaxation time τ_D (13) depending on T according to the power law. The scale of this time qualitatively correlates with the transition frequency region observed in the experiment [9]. In the region $\omega \le \omega_{slow}$, the behavior of a 2D electron system perturbed by induction forces follows the adiabatic scenario. In this case, the measured signal is proportional to $\propto \dot{H}$, and the quantity ω_{slow}, being inversely proportional to the relaxation time according to Eqs. (26), is exponentially small. Such a regime at the Hall plateaus has not yet been observed. However, for a normal 2D system, the corresponding adiabatic induction kinetics with the characteristic time τ_{fast} given by Eqs. (24) manifests itself in the experiment [1–4].

I am grateful to V. Dolgopolov and V. Gantmakher for discussing the results of this study and for useful comments. The work was supported by the Russian Foundation for Basic Research, project no. 02-02-17082.

REFERENCES

1. V. Dolgopolov, N. Zhitenev, and A. Shashkin, Pis'ma Zh. Éksp. Teor. Fiz. **52**, 826 (1990) [JETP Lett. **52**, 196 (1990)].
2. V. Dolgopolov, N. Zhitenev, and A. Shashkin, Europhys. Lett. **14**, 255 (1991).

3. V. Dolgopolov, A. Shashkin, N. Zhitenev, *et al.*, Phys. Rev. B **46**, 12560 (1992).
4. V. Dolgopolov, A. Shashkin, J. Broto, *et al.*, Phys. Rev. Lett. **86**, 5566 (2001).
5. R. Laughlin, Phys. Rev. B **23**, 5632 (1981).
6. F. I. B. Williams, E. Andrei, *et al.*, in *Springer Series in Solid-State Sciences*, Ed. by F. Kuchar, H. Heinrich, and G. Bauer (Springer-Verlag, Berlin, 1990), Vol. 97, p. 192.
7. R. Ashori, J. Lebens, N. Bigelow, and R. Silsbee, Phys. Rev. B **48**, 4616 (1993).
8. V. Dolgopolov, H. Drexler, W. Hanzen, *et al.*, Phys. Rev. B **51**, 7958 (1995).
9. B. Jeanneret, B. Hall, H. Buhlmann, *et al.*, Phys. Rev. B **51**, 9752 (1995).
10. T. Demel, D. Heitmann, P. Grambow, and K. Ploog, Phys. Rev. B **38**, 12732 (1988).
11. L. D. Landau and E. M. Lifshitz, *Course of Theoretical Physics*, Vol. 5: *Statistical Physics* (Nauka, Moscow, 1964; Pergamon, Oxford, 1980).

Translated by E. Golyamina

JETP Letters, Vol. 75, No. 9, 2002, pp. 470–473. Translated from Pis'ma v Zhurnal Éksperimental'noĭ i Teoreticheskoĭ Fiziki, Vol. 75, No. 9, 2002, pp. 560–564.

Friedel Oscillations of a Magnetic Field Penetrating into a Normal Metal and a Size-Quantized System

L. I. Magarill, M. M. Mahmoodian, and M. V. Éntin

Institute of Semiconductor Physics, Siberian Division, Russian Academy of Sciences, Novosibirsk, 630090 Russia

e-mail: entin@isp.nsc.ru

Received March 27, 2002; in final form, April 8, 2002

A magnetic field applied to a size-quantized system causes persistent equilibrium currents nonuniformly distributed across this system. For a quantum film and a two-dimensional strip, the distributions of the dia- and paramagnetic currents and magnetic field are determined. The possibility of observing field distribution by NMR is discussed. © *2002 MAIK "Nauka/Interperiodica".*

PACS numbers: 75.70.Ak; 75.20.En

The magnetization of a normal metal in a magnetic field is associated with the dia- and paramagnetic currents flowing at its surface. These currents are distributed within the surface layer, where the magnetic field is inhomogeneous. Since the diamagnetism is rather weak, the corrections to the magnetic field are small and, hence, are usually ignored in considering the kinetic phenomena.

However, even very small magnetic-field variations can be significant in quantum systems. For example, a magnetic field acting on an atomic nucleus is partially screened by the electron shells [1]. As a result, the NMR frequency shifts and becomes too dependent on the chemical environment of the atom. This shift can be measured experimentally, because the NMR line is rather narrow as compared to the typical inverse electron relaxation time.

In an artificial size-quantized system, diamagnetic electron currents also screen the external magnetic field and cause changes in the magnetic field acting on the nuclei. The state of the electron subsystem affects the magnetic field strength. In particular, an electric modulation of electrons by a field-effect electrode provides a possibility to electrically act on the nuclei. The characteristic scale of inhomogeneity of the diamagnetic current and magnetic field distributions can be equal to the transverse dimension of the system. Then, different nuclei are in magnetic fields of different strength.

The purpose of this paper is the determination of magnetic field distribution in different size-quantized systems, specifically, in a quantum film and quantum strip.

The orbital magnetism in systems with spatial quantization was considered in a number of papers (see, e.g., [2–4]). However, these papers deal with the total magnetization of small systems. Unlike previous studies, we concentrate on the spatial distribution of a magnetic field.

Diamagnetic contribution. Let us consider an electron gas confined in a film with the coordinates $0 < x < L_x$, $0 < y < L_y$, and $0 < z < d$, where $d \ll L_x, L_y$. Let a magnetic field $\mathbf{B}$ be directed along the x axis in the plane of the film, i.e., in the (x, y) plane. The field obeys the Maxwell equation

$$\partial \mathbf{B}/\partial z = 4\pi \mathbf{j}(z)/c.$$

The diamagnetic current density $\mathbf{j}$ has only a y component. Since the diamagnetism is weak, we ignore the corrections to the uniform external field in the expression for the diamagnetic current. The equilibrium current density can be derived from the expression

$$\begin{aligned} j_y(z) &= \mathrm{Sp}(\hat{j}_y(z)\, f(\hat{\mathcal{H}})) \\ &= \int_{-\infty}^{\infty} dE\, f(E)\mathrm{Sp}(\hat{j}_y(z)\delta(E - \hat{\mathcal{H}})), \end{aligned} \tag{1}$$

where $\hat{\mathcal{H}} = (\hat{\mathbf{p}} + e\mathbf{A}/c)^2/2m + U(z)$ is the Hamiltonian of an electron in the magnetic field, $\mathbf{A} = (0, -B_0 z, 0)$ is the vector potential of the external magnetic field $\mathbf{B}_0$, $U(z)$ is the bounding potential, $\hat{j}_y(z) = -e\{\hat{v}_y, \delta(z - \hat{z})\}/S$ is the operator of orbital current density, $\hat{\mathbf{v}} = (\hat{\mathbf{p}} + e\mathbf{A}/c)/m$ is the operator of electron velocity, the braces $\{\ldots\}$ represent the symmetrization operation, $f(E) = (\exp((E - \mu)/T) + 1)^{-1}$ is the Fermi distribution function (where μ and T are the chemical potential and the temperature), and $S = L_x L_y$ is the area of the system. Here and below, $\hbar = 1$.

We consider the current using the linear approximation in an external field. Expanding the current density

in powers of the magnetic field, we obtain

$$j_y(z) = \frac{e}{mS}\mathrm{Sp}\left[\delta(z-\hat{z})\left(\frac{e}{c}B_0 z f(\hat{\mathcal{H}}_0) - \int_{-\infty}^{\infty} dE\, f(E)\hat{p}_y(\delta(E-\hat{\mathcal{H}}) - \delta(E-\hat{\mathcal{H}}_0))\right)\right]. \quad (2)$$

Here, $\hat{\mathcal{H}}_0 = \hat{\mathbf{p}}^2/2m + U(z)$ is the Hamiltonian in the absence of a magnetic field. For the operator $\delta(E-\hat{\mathcal{H}})$, the following expansion is valid:

$$\delta(E-\hat{\mathcal{H}}_0-\hat{V}) = \delta(E-\hat{\mathcal{H}}_0) + \frac{1}{2\pi i}[\hat{R}^-\hat{V}\hat{R}^- - \hat{R}^+\hat{V}\hat{R}^+] + \ldots, \quad (3)$$

where $\hat{R}^{\pm} = (E-\hat{\mathcal{H}}_0 \pm i\eta)^{-1}$, $\eta \longrightarrow +0$. Using the perturbation $\hat{V} = -(e/m)B_0 z\hat{p}_y$ of the Hamiltonian in the magnetic field and calculating the trace in Eq. (2) in the zero-field states representation, we obtain with the help of Eq. (3)

$$j_y(z) = \frac{2e^2B_0}{mcS}\sum_{n,\mathbf{p}}\left[(z-z_{nn})\varphi_n(z)^2 f(E_{n,\mathbf{p}}) + \sum_{n'\neq n}\frac{p_y^2}{m}\varphi_n(z)\varphi_{n'}(z)z_{nn'}\frac{f_{n,\mathbf{p}}-f_{n',\mathbf{p}}}{E_{n,\mathbf{p}}-E_{n',\mathbf{p}}}\right]. \quad (4)$$

Here, $\varphi_n(z)$ represents the transverse wave functions in the absence of a magnetic field, $\mathbf{p}$ is the longitudinal momentum, $E_{n,\mathbf{p}} = E_n + p^2/2m$ is the electron energy in the nth subband of the transverse quantization, and $f_{n,\mathbf{p}} \equiv f(E_{n,\mathbf{p}})$.

In the rectangular quantum-well model (a potential with hard walls: $U(z) = 0$ within the interval $0 < z < d$ and $U(z) = \infty$ for $z < 0$ and $z > d$), Eq. (4) at $T = 0$ is reduced to the form

$$j_y(E_F, 0; z) = \frac{e^2B_0}{4\pi cd^2}\sum_{n=1}^{\infty}\frac{E_F-E_n}{E_n}\theta(E_F-E_n) \times [(E_F+3E_n)d(2z-d)\sin^2(\pi nz/d) - (E_F-E_n)n\pi z(z-d)\sin(2\pi nz/d)]. \quad (5)$$

Here, $E_F = k_F^2/2m = \mu(T=0)$ is the Fermi energy and $E_n = \pi^2n^2/2md^2$.

The expression for the current at nonzero temperature can be derived from Eq. (5) by using the relation

$$j_y(\mu, T; z) = \int dE\, j_y(E, 0; z)\left(-\frac{\partial f(E)}{\partial E}\right). \quad (6)$$

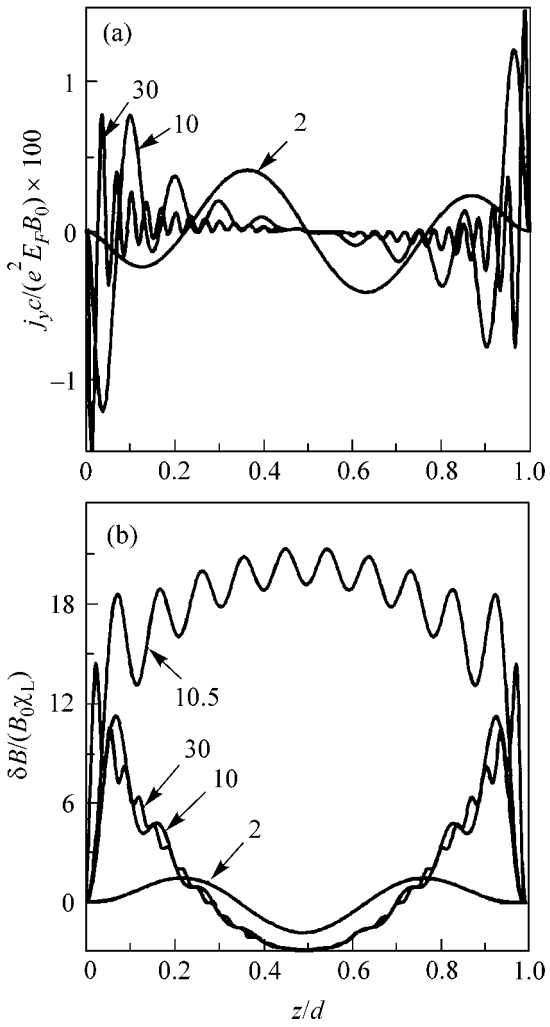

Fig. 1. Evolution of the (a) current density and (b) magnetic field at $T = 0$ with increase in the quantum film thickness. The values of k_Fd/π are indicated in the plots (the integral part of k_Fd/π gives the number of populated subbands). For $k_Fd/\pi = 2$, 10, and 30, the Fermi energy coincides with the subband bottom, while for $k_Fd/\pi = 10.5$, it lies between the 10th and 11th subbands.

Figure 1a shows the distribution of current in a film with hard walls. The current density is antisymmetric about the middle of the well and decreases in an oscillatory manner with the distance from the boundaries. Oscillations are the manifestation of the Friedel effect, namely, the susceptibility singularity at the wave vector $2k_F$. The current density has an alternating sign, so that, strictly speaking, the term "diamagnetic" refers to the total surface current only.

In the low-temperature limit, the decay of current into the depth of the well is slow. The asymptotic behavior of the surface current density in the limit $k_Fd/\pi \gg 1$ for $z \ll d$ can be found by replacing the sum over n in

Eq. (5) by an integral with the use of the Euler–Maclaurin summation formula

$$\sum_{j=m}^{n} f(j) = \int_{m}^{n} dx\, f(x) + \frac{1}{2}[f(n) + f(m)] + \ldots \qquad (7)$$

As a result, we obtain

$$\begin{aligned} j_y &= 3\chi_L c k_F B_0 \left(-\frac{\cos x}{x} + 3x^2 \int_x^\infty \frac{\sin t}{t^5} dt \right), \\ \frac{\delta B}{B_0} &= 4\pi\chi_L \left(1 - \frac{3\sin x}{2x} + \frac{3x^3}{2} \int_x^\infty \frac{\sin t}{t^5} dt \right). \end{aligned} \qquad (8)$$

Here, $\chi_L = -e^2 k_F / 12\pi^2 mc^2$ is the Landau magnetic susceptibility at $T = 0$ and $x = 2k_F z$. The first terms in Eqs.(8) represent the asymptotic behavior in the region $z \gg \pi/k_F$. In particular, the constant contribution to $\delta B/B_0$ exactly yields the Landau magnetic susceptibility. In the region $d - z \ll d$, the quantities j_y and $\delta B/B_0$ exhibit a similar behavior.

At nonzero temperature, we obtain for $k_F z \gg 1$

$$\frac{\delta B}{B_0} = 4\pi\chi_L \left[1 - \frac{3\pi T}{4E_F} \frac{\sin(2k_F z)}{\sinh(z/l_T)} \right], \qquad (9)$$

where $l_T = k_F/2\pi mT$ is the characteristic decay length. Note that the impurity scattering also leads to the decay of $\delta B(z)$ within the mean free path from the surface.

Expressions (8) and (9) for the surface current and magnetic field are also valid in the bulk normal-metal limit, where $d \longrightarrow \infty$. In this case, the ratio between the mean free path and the sample thickness is unimportant. Note that, since our consideration is performed in the weak magnetic-field limit, we implicitly use small parameters, namely, the ratios of the characteristic lengths of the problem to the cyclotron radius. For a finite magnetic field in the bulk normal-metal limit, Eqs. (8) and (9) remain valid up to distances on the order of cyclotron radius from the boundary.

In Fig. 1a, in addition to the surface current oscillating with the coordinate, one can see a small regular component of the current density, which linearly depends on the transverse coordinate. Asymptotically, when $k_F d/\pi \gg 1$, this contribution has the form

$$\begin{aligned} -\frac{e^2 B_0 k_F}{12mcd^2}(z - d/2)(1 + 6\zeta(\zeta - 1)), \\ \zeta = k_F d/\pi - [k_F d/\pi]. \end{aligned} \qquad (10)$$

Here, the square brackets denote the integral part of a number. The linear component is smaller than the surface current by a factor of $k_F d$. The coefficient $(1 + 6\zeta(\zeta - 1))$ multiplying the linear term oscillates with chemical potential in such a way that, when averaged over k_F or over the thickness, it becomes zero (in the bulk metal limit, such an averaging may correspond to the averaging over an ensemble of samples with an inevitable variation in thickness).

At nonzero temperature, the linear term has the form

$$-\frac{e^2 T B_0}{\pi c d}(z - d/2) \sum_{n=1}^{\infty} \frac{\cos(2nk_F d)}{n \sinh(nT/\theta)}, \qquad (11)$$

where $\theta = E_F(\pi k_F d)^{-1}$ is the characteristic temperature above which the linear term exponentially decreases.

The corrections to the magnetic field are shown in Fig. 1b. The linear dependence of j_y on the coordinate causes a contribution to the magnetic field that is parabolic in the coordinate and sensitive to the parameter ζ.

Note that the linear component of the current density and the parabolic contribution to the magnetic field are associated with the orbital magnetism. In a quantum film, the orbital contribution to the magnetic susceptibility exhibits a fluctuating growth with a width proportional to $k_F d$, which corresponds to the increase in the parabolic contribution to the magnetic field.

Two-dimensional strip. Let us consider 2D electrons whose motion is confined within the strip $0 < y < L_y$, $0 < z < d$, where $d \ll L_y$. This case corresponds to the elimination of the x coordinate from the formulas of the previous section. Let the magnetic field **B** also be directed along the x axis. Expression (4) for the current density remains valid if we retain only the summation over n and over the momentum p_y. In the linear approximation in B_0 we obtain, for the rectangular potential well model at zero temperature, the following expression instead of Eq. (5):

$$\begin{aligned} j_y(E_F, 0; z) = \frac{2e^2 B_0 k_F}{3mcd^2} \sum_{n=1}^{\infty} (1 - E_n/E_F)^{1/2} \theta(E_F - E_n) \\ \times [(E_F/E_n + 2)d(2z - d)\sin^2(\pi n z/d) \\ - (E_F/E_n - 1)n\pi z(z - d)\sin(2\pi n z/d)]. \end{aligned} \qquad (12)$$

Figure 2 shows the distribution of the current density in the strip at $T = 0$. By analogy with Eq. (8), for the surface current density in the limit $k_F d/\pi \gg 1$ when $z \ll d$, we obtain

$$\begin{aligned} j_y &= 3\pi\chi_L^{2D} c k_F B_0 x^2 \left(\int_0^x \frac{J_2(t)dt}{t^2} - \frac{1}{3} \right) \\ &= 3\pi\chi_L^{2D} c k_F B_0 x^2 \int_x^\infty \frac{J_2(t)dt}{t^2}. \end{aligned} \qquad (13)$$

Here, $\chi_L^{2D} = -e^2/12\pi mc^2$ is the Landau magnetic susceptibility for the 2D electron gas at $T = 0$ and $J_2(t)$ is the Bessel function.

Expression (13) for the current density has the following asymptotic behaviors:

$$j_y = 3\pi\chi_L^{2D} c k_F B_0 \begin{cases} \dfrac{x^2}{3} & \text{for } x \ll 1, \\ \sqrt{\dfrac{2}{\pi x}}\sin(x-\pi/4) & \text{at } x \gg 1. \end{cases} \quad (14)$$

The decay of the Friedel oscillations far away from the boundary proves to be slower than in the 3D case.

At nonzero temperature, we obtain for $k_F z \gg 1$

$$j_y = 3\pi\chi_L^{2D} c k_F B_0 \frac{\sin(2k_F z - \pi/4)}{\sqrt{\pi k_F z}} \frac{z/l_T}{\sinh(z/l_T)}. \quad (15)$$

Paramagnetic current. In addition to the diamagnetic current, a paramagnetic current related to electron spin is also present in the system. This contribution can also be found from Eq. (1) with allowance for the spin-related component of the Hamiltonian, $-g\mu_B B_0 \sigma_x/2$, and the spin-related components of the current density operator, $\hat{\mathbf{j}}^{(sp)} = cg\mu_B \nabla(\boldsymbol{\sigma}\delta(z - \hat{z}))/S$. Here, g is the electron g factor, μ_B is the Bohr magneton, and σ_i represents the Pauli matrices. In the linear approximation in B_0, we obtain, after simple mathematics, the following expression for the paramagnetic current density:

$$j_y^{(sp)} = \frac{g^2\mu_B^2 c B_0}{2S}\sum_{n,\mathbf{p}}\left(-\frac{\partial f(E_{n\mathbf{p}})}{\partial E}\right)\frac{\partial\varphi_n^2(z)}{\partial z} \equiv \frac{g^2\mu_B^2 c B_0}{4}\frac{\partial}{\partial\mu}\frac{\partial}{\partial z}n(z), \quad (16)$$

where $n(z)$ is the 2D or 3D local electron concentration. This current and the corresponding magnetic field must be added to the diamagnetic contributions considered in the preceding sections. The ratio between the diamagnetic and paramagnetic contributions depends on the g factor and, in principle, can widely vary for different materials.

In the specific case of a 3D quantum film with hard walls at $T = 0$, one has

$$j_y^{(sp)} = -\frac{g^2\mu_B^2 m k_F^2 c B_0}{2\pi^2}\left(\frac{\cos x}{x} - \frac{\sin x}{x^2}\right), \quad \delta B = \frac{g^2\mu_B^2 m k_F B_0}{\pi}\left(1 - \frac{\sin x}{x}\right). \quad (17)$$

For a 2D strip, the paramagnetic current density has the form

$$j_y^{(sp)} = g^2\mu_B^2 m k_F c B_0 J_1(x)/2. \quad (18)$$

Consider a thought experiment on the excitation of nuclear spin transitions by an alternating gate voltage. Let a quantum film with a vertical gate be placed in a magnetic field with the z and x components. In an infinite film, the normal field component remains unscreened. The longitudinal component of the magnetic field depends on the number of electrons and on their states and, hence, can be controlled by acting on the electron subsystem. In particular, an alternating voltage applied to the gate will modulate the magnetic field and induce NMR transitions. The resonance can be detected by the frequency (or magnetic-field) dependence of the gate impedance.

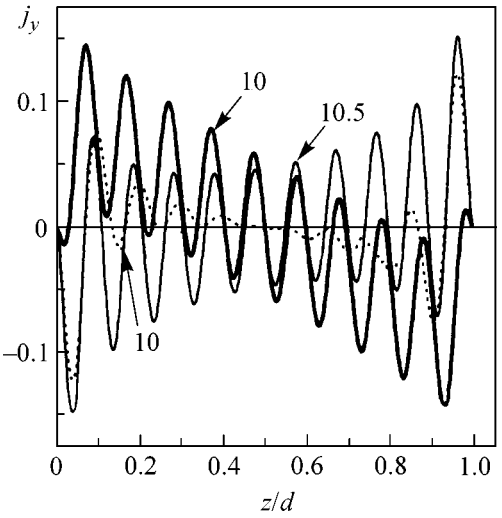

Fig. 2. Current density in a 2D strip at $T = 0$ in units of $e^2 B_0 k_F/mc$; $k_F d/\pi = 10$ and 10.5. The dotted curve is presented for comparison and corresponds to the dimensionless current density in the quantum film at $k_F d/\pi = 10$. One can see that, in the 2D case, the oscillations of the current density are damped much slower than in the 3D case.

In addition to the excitation of nuclear transitions by an alternating magnetic field, the quadrupolar nuclei are also affected by the nonuniform electric field produced by the gate electrode. However, this effect is absent for nuclei with spin 1/2 for which only the NMR takes place.

This work was supported by the Russian Foundation for Basic Research (project nos. 00-02-17658 and 02-02-16377) and the programs of the Ministry of Science of the Russian Federation "Physics of Solid-State Nanostructures" and "Quantum Macrophysics."

REFERENCES

1. L. D. Landau and E. M. Lifshitz, *Course of Theoretical Physics*, Vol. 5: *Statistical Physics* (Nauka, Moscow, 1995; Pergamon, Oxford, 1980), Part 1.
2. M. Ya. Azbel, Phys. Rev. B **48**, 4592 (1993).
3. K. Richter, D. Ullmo, and R. A. Jalabert, Phys. Rep. **276**, 1 (1996).
4. E. Gurevich and B. Shapiro, J. Phys. **I 7**, 807 (1997).

Translated by E. Golyamina

JETP Letters, Vol. 75, No. 9, 2002, pp. 474–478. Translated from Pis'ma v Zhurnal Éksperimental'noĭ i Teoreticheskoĭ Fiziki, Vol. 75, No. 9, 2002, pp. 565–569.

Dynamics of a Two-Level System Interacting with a Random Classical Field

G. B. Lesovik, A. V. Lebedev*, and A. O. Imambekov

Landau Institute for Theoretical Physics, Russian Academy of Sciences, ul. Kosygina 2, Moscow, 117334 Russia

** e-mail: alebedev@itp.ac.ru*

Received March 28, 2002

The dynamics of a particle interacting with a random classical field in a two-well potential is studied by the functional integration method. The probability of particle localization in either of the wells is studied in detail. Certain field-averaged correlation functions for quantum-mechanical probabilities and the distribution function for the probabilities of final states (which can be considered as random variables in the presence of a random field) are calculated. The calculated correlators are used to discuss the dependence of the final state on the initial state. One of the main results of this work is that, although the off-diagonal elements of the density matrix disappear with time, a particle in the system is localized incompletely (wave-packet reduction does not occur), and the distribution function for the probability of finding particle in one of the wells is a constant at infinite time.

PACS numbers: 03.65.Ta; 03.65.Yz

The standard interpretation of quantum mechanics includes the concept of the wave-packet reduction (WPR) in the act of measurement [1]. The question of the WPR mechanism either remains beyond the theory or is postulated. In [2], it was suggested that the reservoir be regarded as a WPR source. In this work, we used a two-level system as an example to study in detail the influence of the reservoir degrees of freedom (which were modeled by a random classical field) on the localization process.

The decoherence concept, which was developed over the past 20 years, leaves the WPR problem open [3]. Researchers are typically interested in the evolution of the density matrix of a quantum system interacting with the surrounding medium. With such an approach, much information on the dynamics of the system is lost after averaging over the medium degrees of freedom, rendering the WPR problem unresolved. In [2], it was suggested that the WPR be considered in terms of quantities other than the density matrix.

In this work, we used the simple two-level system as an example to demonstrate the method for and the results of calculating the quantities of this sort.

Let us consider a particle interacting with a random classical field in a double-well potential. The problem of interest is as follows: the particle is held in the left well until $t = 0$, whereupon it is released. In what follows, we are interested in the quantities averaged over the medium degrees of freedom. Since, after averaging, the probability of finding a particle in the left well does not carry full information about the dynamics [2], we will be interested not only in the medium-averaged probability $\langle P_{L\to L}(t)\rangle$ of finding a particle in the left well (the first and second indices denote the initial and final states, respectively), but also in the correlators of the form

$$\langle P_{L\to L}(t)P_{L\to R}(t)\rangle, \tag{1}$$

where the parentheses stand for the averaging over the degrees of freedom of the reservoir. The necessity for calculating the correlators of this type follows from the fact that the probabilities given by the density matrix are the result of both quantum-mechanical averaging and averaging over the medium degrees of freedom. For instance, $\langle P_{L\to L}(t=\infty)\rangle$ can become equal to 1/2 by various ways. A situation is possible for which, depending on the reservoir state, either $P_{L\to L}(t=\infty) = 1$ or $P_{L\to L}(t=\infty) = 0$, while 1/2 is obtained only after averaging. In this case, the WPR occurs in the model considered, and the zero value of correlator (1) is unambiguous evidence of this fact. In the more general case, there is a certain probability density $P_{L\to L}(t)$ of the reservoir states for which the particle occurs in the right well with the probability $P_{L\to L}(t)$. If all correlators of the form $\langle P_{L\to L}(t)^n\rangle$ are known, one can determine the quantity $P(P_{L\to L}(t))$.

Let us formulate the model in more detail. Assume that the wells are symmetric, so that the ground level is degenerate in the absence of tunneling. Under certain conditions [4], the Hilbert space of particle states can be thought of as being two-dimensional.

The states for which the particle coordinate takes the definite values $\pm q_0/2$ are chosen as the basis set. In the

presence of tunneling, the Hamiltonian of a particle not interacting with the field has the form

$$H_0 = -\frac{1}{2}\hbar\Delta\sigma_x.$$

Here, σ_x is the Pauli matrix, and the basis is chosen so that the eigenvalue +1(–1) of the matrix σ_z corresponds to the particle localized in the right(left) well. The interaction of the field with a particle is taken into account by adding to the Hamiltonian the term $q\varphi(t)$, which is linear in the field. In this model, the random field is determined by the external medium. We assume that the probability distribution for the field $\varphi(t)$ is Gaussian and the field correlator has the white-noise form

$$\langle\varphi(t_1)\varphi(t_2)\rangle = \delta(t_1 - t_2)\langle\varphi^2\rangle. \quad (2)$$

In this case, the averaging is carried out over the degrees of freedom of the surrounding medium, which induces the uncontrolled field deviations from zero. The Hamiltonian of the particle is

$$H(t) = -\frac{1}{2}\hbar\Delta\sigma_x + \frac{q_0\varphi(t)}{2}\sigma_z. \quad (3)$$

This model is equivalent to the spin 1/2 in a magnetic field, whose x component is fixed, while the component along the z axis is random.

Making use of the influence functional [5], one can write the probability $\langle P_{L\to L}(t)\rangle$ as a double functional path integral:

$$\begin{aligned}(\langle P_{L\to L}(t)\rangle = \iint Dq_1(\tau 1)Dq_2(\tau 2)A[q_1(\tau 1)])\\ \times A^*[q_2(\tau 2)]F[q_1(\tau 1), q_2(\tau 2)],\end{aligned} \quad (4)$$

where the integral is taken over all paths for which $q_1(0) = q_2(0) = q_1(t) = q_2(t) = -q_0/2$, and $A[q(\tau)]$ is the amplitude for the path $q(\tau)$ in the absence of a random field; $F[q_1(\tau 1), q_2(\tau 2)]$ is the influence functional that is equal, for the random Gaussian potential with correlator (2), to [5]

$$\begin{aligned}&F[q_1(\tau 1), q_2(\tau 2)]\\ &= \left\langle \exp\left\{-\frac{i}{\hbar}\int_0^t \varphi(\tau)(q_1(\tau) - q_2(\tau))d\tau\right\}\right\rangle\\ &= \exp\left\{-\frac{\langle\varphi^2\rangle}{2\hbar^2}\int_0^t (q_1(\tau) - q_2(\tau))^2 d\tau\right\}.\end{aligned} \quad (5)$$

At any instant of time, the pair of paths $[q_1, q_2]$ is in one of the four states [–, –], [–, +], [+, –], and [+, +], which will be denoted as A, B, C, and D. We introduce the notation $\xi(t) = q_0^{-1}(q_1(t) - q_2(t))$. Then, the influence functional is recast as

$$F[q_1(\tau 1), q_2(\tau 2)] = \exp\left\{-\Gamma\int_0^T \xi(t)^2 dt\right\}, \quad (6)$$

$$\Gamma = q_0^2\langle\varphi^2\rangle/2\hbar^2. \quad (7)$$

Following the formalism described in [4], we expand $\langle P_{L\to L}(t)\rangle$ in powers of $i\Delta/2$. This multiplier (except for the sign) appears at every jump between the wells. We will describe each state $[q_1, q_2]$ at every instant of time as a four-dimensional vector $\mathbf{E}_i$, where $i = \{1, 2, 3, 4\}$ corresponds to the $\{A, B, C, D\}$ states. The matrix of possible jumps has the form (the sign corresponds to the sign of transition amplitude)

$$\Lambda = \begin{bmatrix} 0 & -1 & 1 & 0\\ -1 & 0 & 0 & 1\\ 1 & 0 & 0 & -1\\ 0 & 1 & -1 & 0\end{bmatrix}. \quad (8)$$

Let us introduce the matrix allowing for the path weights due to the influence functional:

$$\mathbf{U}(t) = \begin{bmatrix} 1 & 0 & 0 & 0\\ 0 & e^{-\Gamma t} & 0 & 0\\ 0 & 0 & e^{-\Gamma t} & 0\\ 0 & 0 & 0 & 1\end{bmatrix}. \quad (9)$$

Then $\langle P_{L\to L}(t)\rangle$ can be written as

$$\begin{aligned}&\langle P_{L\to L}(t)\rangle = \mathbf{E}_1^T\\ &\times\left[\sum_{n=0}^{\infty}\int_0^t dt_n\int_0^{t_n} dt_{n-1}\ldots\int_0^{t_2} dt_1\mathbf{U}(t - t_n)\mathbf{S}\ldots\mathbf{S}\mathbf{U}(t_1)\right]\times\mathbf{E}_1,\end{aligned} \quad (10)$$

where $\mathbf{S} = i\Delta/2\Lambda$; $t_1, \ldots, t_n$ are the hopping times; and the vector $\mathbf{E}_1 = \{1, 0, 0, 0\}^T$corresponds to the state A. Applying the Laplace transform to $\langle P_{L\to L}(t)\rangle$,

$$\langle P_{L\to L}(\lambda)\rangle = \int_0^{\infty}\langle P_{L\to L}(t)\rangle e^{-\lambda t}dt,$$

and changing the integration variables in Eq. (10), one obtains

$$\begin{aligned}\langle P_{L\to L}(\lambda)\rangle &= \mathbf{E}_1^T\times\left[\sum_{n=0}^{\infty}[\mathbf{U}(\lambda)\mathbf{S}]^n\right]\mathbf{U}(\lambda)\times\mathbf{E}_1\\ &= \mathbf{E}_1^T\times[\mathbf{U}^{-1}(\lambda) - \mathbf{S}]^{-1}\times\mathbf{E}_1,\end{aligned} \quad (11)$$

where $\mathbf{U}(\lambda)$ is the Laplace transform of $\mathbf{U}(t)$:

$$\mathbf{U}(\lambda) = \begin{bmatrix} \lambda^{-1} & 0 & 0 & 0 \\ 0 & (\lambda+\Gamma)^{-1} & 0 & 0 \\ 0 & 0 & (\lambda+\Gamma)^{-1} & 0 \\ 0 & 0 & 0 & \lambda^{-1} \end{bmatrix}. \quad (12)$$

Therefore, the calculation of $\langle P_{L\to L}(t)\rangle$ amounts to the evaluation of the matrix element of the inverse of a 4×4 matrix and to the taking of inverse Laplace transform. The result is

$$\langle P_{L\to L}(\lambda)\rangle = \frac{1}{2\lambda}\frac{2\lambda^2+2\lambda\Gamma+\Delta^2}{\lambda^2+\Gamma\lambda+\Delta^2}.$$

To find $\langle P_{L\to L}(t=\infty)\rangle$, it suffices to know only the residue of $\langle P_{L\to L}(\lambda)\rangle$ at $\lambda = 0$, which is equal to the inverse Laplace transform at $t = \infty$. The quantity $\langle P_{L\to L}(t)\rangle$ can be exactly calculated to give

$$\frac{1}{2} + \frac{\exp\left\{\frac{1}{2}t(-\Gamma+\sqrt{\Gamma^2-4\Delta^2})\right\}(\Gamma+\sqrt{\Gamma^2-4\Delta^2})}{4\sqrt{\Gamma^2-4\Delta^2}} + \frac{\exp\left\{-\frac{1}{2}t(\Gamma+\sqrt{\Gamma^2-4\Delta^2})\right\}(-\Gamma+\sqrt{\Gamma^2-4\Delta^2})}{4\sqrt{\Gamma^2-4\Delta^2}}. \quad (13)$$

One can see that $\langle P_{L\to L}(t=\infty)\rangle = 1/2$ for nonzero Γ; at $\Gamma = 2\Delta$, the damping oscillations give way to relaxation.

In the limit $\Gamma \gg \Delta$, two relaxation times appear in the system. One of them, $\tau_1 = \Gamma^{-1}$, is considerably shorter than the other, $\tau_2 = \Gamma/\Delta^2$.

The off-diagonal elements $\langle \Psi_L(t)^*\Psi_R(t)\rangle$ of the density matrix can be calculated in a similar way. The result

$$\langle \Psi_L(t)^*\Psi_R(t)\rangle = \frac{i\Delta\exp\left\{-\frac{1}{2}t(\Gamma+\sqrt{\Gamma^2-4\Delta^2})\right\}}{2\sqrt{\Gamma^2-4\Delta^2}} - \frac{i\Delta\exp\left\{\frac{1}{2}t(-\Gamma+\sqrt{\Gamma^2-4\Delta^2})\right\}}{2\sqrt{\Gamma^2-4\Delta^2}} \quad (14)$$

also has two characteristic times, with $\langle \Psi_L(\infty)^*\Psi_R(\infty)\rangle = 0$. In the limit $\Gamma \gg \Delta$, the maximum magnitude $\Delta/2\Gamma$ is reached in a time on the order of τ_1.[1]

To calculate the quantity $\langle P_{L\to L}(t)P_{L\to L}(t)\rangle$, one can also use the formalism developed above. In this case, the path integral is taken over four trajectories and the system state is described at every instant by a 16-dimensional vector. After introducing for each pair of trajectories their own variables $\xi_1(t) = q_0^{-1}(q_1(t) - q_2(t))$ and $\xi_2(t) = q_0^{-1}(q_3(t) - q_4(t))$, the four-point influence functional can be written, similarly to Eq. (6), as

$$F[q_1(\tau 1), q_2(\tau 2), q_3(\tau 3), q_4(\tau 4)] = \exp\left\{-\Gamma\int_0^t (\xi_1(\tau)+\xi_2(\tau))^2 d\tau\right\}. \quad (15)$$

Introducing, by analogy with Eqs. (8) and (12), the 16-dimensional matrices $\mathbf{S2}(t)$ and $\mathbf{U2}(t)$ (we do not give here their explicit form), one arrives at the formula analogous to Eq. (11):

$$\langle P_{L\to L}(t)P_{L\to L}(t)\rangle = \mathbf{E}_1^T \times [\mathbf{U2}^{-1}(\lambda) - \mathbf{S2}]^{-1} \times \mathbf{E}_1, \quad (16)$$

where the vector $\mathbf{E}_1$ corresponds to the state $[-,-,-,-]$ of the paths $[q_1, q_2, q_3, q_4]$.

Calculation gives

$$\langle P^2_{L\to L}(t)\rangle = \frac{1}{3\lambda} + \frac{\Gamma+\lambda}{2(\Delta^2+\Gamma\lambda+\lambda^2)} + \frac{\Delta^2+(\Gamma+\lambda)(4\Gamma+\lambda)}{6(4\Delta^2(3\Gamma+\lambda)+\lambda(\Gamma+\lambda)(4\Gamma+\lambda))}. \quad (17)$$

For the infinite time, one has $\langle P_{L\to L}(t=\infty)^2\rangle = 1/3$. In the limit $\Gamma \gg \Delta$, this correlator also has two characteristic times, which are determined by the real parts of the poles of $\langle P^2_{L\to L}(t)\rangle$. For the first nonvanishing terms, the relaxation times in Eq. (17) are equal to τ_1, τ_1, $\tau_1/4$, τ_2, and $\tau_2/3$.

[1] Note that, since the particle in our problem (or "spin" in the equivalent problem) interacts with the classical field, it is formally described by a pure density matrix. This is natural, because the particle cannot act on the classical field, so that the entangled quantum states do not appear. Nevertheless, from the practical viewpoint, the distinction between the presence of a "real" reservoir and the random classical field is insignificant, because, to prove that the particle is in a pure state, one must conduct a set of measurements. For example, to obtain the definite result in a single measurement, one must know exact data on the magnitude of fluctuating classical field $\varphi(t)$, whose monitoring at the exact "spin" location is highly conjectural. Moreover, the temporal dynamics of the probabilities $\langle P_{L\to L}(t)\rangle$ are identical in both cases.

For the remaining second-order correlators, similar calculations give

$$\langle P_{L\to R}(t=\infty)^2\rangle = \frac{1}{3},$$
$$\langle P_{L\to L}(t=\infty)P_{L\to R}(t=\infty)\rangle = \frac{1}{6}. \quad (18)$$

Thus, although the off-diagonal elements of the density matrix vanish with time, $\langle P_{L\to L}(t=\infty)P_{L\to R}(t=\infty)\rangle \neq 0$, so that the particle localization (wave-packet reduction) in the system does not occur.

It is straightforward to generalize the above computational procedure to the case of $\langle P_{L\to L}(t)^n\rangle$, although the sizes of the corresponding matrices rapidly increase. Numerical computations show that

$$\langle P_{L\to L}(t=\infty)^3\rangle = \frac{1}{4}, \quad \langle P_{L\to L}(t=\infty)^4\rangle = \frac{1}{5}. \quad (19)$$

Thus, we assume (although we have not succeeded in obtaining the general proof) in our model that the probability density $P(P_{L\to L}(\infty))$ of the reservoir states for which the particle may be found in the left well with the probability $P_{L\to L}(\infty)$ in an infinite time is unity on the interval (0, 1). Indeed, in this case,

$$\langle P^n_{L\to L}\rangle = \int_0^1 (P_{L\to L})^n P(P_{L\to L})d(P_{L\to L}) = \frac{1}{n+1}, \quad (20)$$

which is fully consistent with our previous results. The correlators of the form $\langle P^n_{L\to L}P^m_{L\to R}\rangle$ are equal to

$$\langle P^n_{L\to L}P^m_{L\to R}\rangle = \int_0^1 P^n(1-P)^m dP = \frac{n!m!}{(n+m+1)!}. \quad (21)$$

Using the symmetry of matrices in Eq. (11), one can establish the following symmetry about the permutation of the initial and final states:

$$\langle P^n_{L\to L}P^m_{L\to R}\rangle = \langle P^n_{L\to L}P^m_{R\to L}\rangle. \quad (22)$$

Let us now consider how the final state depends on the initial state if the latter has the form

$$|S\rangle = a|\Psi_L\rangle + b|\Psi_R\rangle, \quad |a|^2 + |b|^2 = 1. \quad (23)$$

Using Eqs. (21) and (23), one obtains

$$\langle P^n_{S\to L}\rangle = \langle (a^*\langle\Psi_{L\to L}| + b^*\langle\Psi_{R\to L}|)^n (a\langle\Psi_{L\to L}| + b\langle\Psi_{R\to L}|)^n\rangle = (|a|^2 + |b|^2)^n/(n+1) = 1/(n+1). \quad (24)$$

Therefore, in the model considered, the distribution function for the probabilities in the final state is independent of the initial state after a very long time.

Nevertheless, the final state depends on the initial state in every *particular* case. The sensitivity to the initial state can be determined by calculating the following correlator:

$$\langle (P_{S\to L} - P_{S'\to L})^2\rangle = \frac{|ab' - a'b|^2}{3}, \quad (25)$$

where $|S'\rangle = a'|\Psi_L\rangle + b'|\Psi_R\rangle$.

Consider, as an example, the case for which $a = b = 1/\sqrt{2}$ for one initial (ground) state $|S\rangle$ and $a' = b' = 1/\sqrt{2}$ for the other (excited) state $|S'\rangle$. Then, $\langle (P_{S\to L} - P_{S'\to L})^2\rangle = 1/3$. Note that the value $1/\sqrt{3}$ obtained for the mean difference in the final probabilities is larger than the average probability 1/2.

We are now in position to discuss the sensitivity of the final state to the variations in the external field. We formulate the problem in terms of a spin in an external magnetic field. Consider the correlator of the form $\langle (P_L\{H(t)\} - P_L\{H(t) + \delta H_z(t)\})^2\rangle$. In the general form, the problem is complicated by the fact that the Hamiltonian $\mathbf{H}(t)\boldsymbol{\sigma}$ does not commute with itself at different instants of time. However, we can consider a particular case of the field $\delta H_z(t)$ acting during a short time interval (such that the spin rotation about the x axis can be ignored because of the smallness of $H_x\sigma_x$) at the very beginning of state evolution. In this case, the problem reduces to the previous problem if the state $|S'\rangle = a'|\Psi_L\rangle + b'|\Psi_R\rangle$ is defined as

$$|S'\rangle = \exp\left[\frac{i}{\hbar}\int dt\delta H_z(t)\sigma_z\right][a|\Psi_L\rangle + b|\Psi_R\rangle]. \quad (26)$$

The new state (a', b') is determined by the relative phase incursion $2\delta\Phi = (2/\hbar)\int \delta H_z(t)dt$ for a and b. If the field pulse is applied at nonzero time, we can reformulate the problem starting with a certain fixed state (a_0, b_0) at time t_0. In this case, one obtains, after averaging, l

$$\langle (P_L\{H(t)\} - P_L\{H(t) + \delta H_z(t)\})^2\rangle_{t=\infty} = \langle (P_L(t_0)P_R(t_0))\rangle \frac{4\sin^2(\delta\Phi)}{3}. \quad (27)$$

We note in conclusion that, in our opinion, the localization in a double-well potential will occur at long times if a quantum reservoir is added to the classical reservoir. Qualitatively, this process can be imagined as follows: at every instant of time, the energy levels in the wells are different due to the classical field, the difference being sufficiently large for the instantaneous eigenstates of the Hamiltonian to be localized in either of the wells, while the transition to the lowest (localized) state occurs due to the photon emission.

We thank G.E. Volovik for helpful discussions. This work was supported by the Public Foundation for Assisting in Russian Science, the Russian Foundation for Basic Research (project no. 00-02-16617), the Ministry of Science (project "Physical Fundamentals of Quantum Calculations"), the Dutch Scientific Foundation (grant for collaboration with Russia), and the Swiss Scientific Foundation.

REFERENCES

1. L. D. Landau and E. M. Lifshitz, *Course of Theoretical Physics*, Vol. 3: *Quantum Mechanics: Non-Relativistic Theory* (Nauka, Moscow, 1974; Pergamon, New York, 1977), Chap. 1, Parag. 7.
2. G. B. Lesovik, Pis'ma Zh. Éksp. Teor. Fiz. **74**, 528 (2001) [JETP Lett. **74**, 471 (2001)]; G. B. Lesovik, Usp. Fiz. Nauk **171**, 449 (2001).
3. S. L. Adler, quant-ph/0112095.
4. A. J. Leggett, S. Chakravarty, A. T. Dorsey, *et al*., Rev. Mod. Phys. **59**, 1 (1987).
5. R. P. Feynman and F. L. Vernon, Jr., Ann. Phys. (N.Y.) **24**, 118 (1963).

Translated by V. Sakun

JETP Letters, Vol. 75, No. 9, 2002, pp. 479–481. Translated from Pis'ma v Zhurnal Éksperimental'noĭ i Teoreticheskoĭ Fiziki, Vol. 75, No. 9, 2002, pp. 570–572.

Invariant Relation in the Problem of Size Quantization in a Self-Consistent Potential Near the Semiconductor Boundary

S. I. Dorozhkin

Institute of Solid-State Physics, Russian Academy of Sciences, Chernogolovka, Moscow region, 142432 Russia

Received April 2, 2002

The invariant relation in the eigenvalue problem is found for a one-dimensional nonlinear integrodifferential operator acting on the normalized eigenfunctions. The invariance of the obtained relationship follows, in particular, from the fact that it is independent of the detailed form of the operator. This problem arises in the physics of a two-dimensional electron system near the semiconductor boundary, where the potential well is formed, on the one hand, by a high potential barrier at the boundary and, on the other, by the intrinsic electric field screened by two-dimensional electrons filling the well. The invariant relates the energy of the size-quantization level to the average size of electron wave function in the well. © *2002 MAIK "Nauka/Interperiodica".*

PACS numbers: 72.20.Dp; 73.40.Kp

The problem analyzed in this work was solved numerically over more than thirty years (see review [1]). It arises in the calculation of electron energy levels and wave functions in one-dimensional potential wells near flat interfaces between a semiconductor and an isolator or between two semiconductors with different energy gaps. In the case considered in this work, the interface corresponds to the infinitely high potential step at $z = 0$ (the z axis is perpendicular to the interface; see figure). Electrons with charge e and effective mass m are held against the interface by an external electric field E_0 created by the charges in the $z < 0$ half-space. All charges are assumed to be uniformly distributed along the planes parallel to the semiconductor boundary. The potential well is typically narrow, so that the quantization of electron motion along the z axis gives rise to discrete size-quantization levels (bottoms of the subbands corresponding to the free electron motion along the semiconductor surface). The problem is nonlinear because of the screening of the electric field by electrons with surface density n_s. The basic equation for this problem can be written at $z \geq 0$ in the form [1]

$$-\frac{\hbar^2}{2m}\frac{d^2\Psi_0(z)}{dz^2} + \Psi_0(z)e\left[-E_0 z + \frac{2\pi e n_s}{\chi} z + \frac{4\pi e n_s}{\chi}\int_0^z (\Psi_0(u))^2 (u - z)du + f(z)\right] = \varepsilon_0 \Psi_0(z). \quad (1)$$

Here, ε_0 is the energy of the lowest level, χ is the dielectric constant of the semiconductor, and $f(z)$ is the E_0- and n_s-independent potential created by the charges bound in the region $z > 0$. Other limitations on this potential will be discussed below. The eigenfunction $\Psi_0(z)$ of the problem satisfies the boundary conditions $\Psi_0(z = 0) = \Psi_0(z = \infty) = 0$ and is normalized:

$$\int_0^\infty (\Psi_0(z))^2 dz = 1. \quad (2)$$

The main goal of this work is to demonstrate that the solutions to Eqs. (1) and (2) satisfy the relationship

$$\frac{\partial \varepsilon_0}{\partial E_0} + e z_0 - \frac{2\pi e^2 n_s}{\chi}\frac{\partial z_0}{\partial E_0} + e n_s \frac{\partial z_0}{\partial n_s} = 0, \quad (3)$$

where

$$z_0 = \int_0^\infty (\Psi_0(z))^2 z dz \quad (4)$$

is the mean value of coordinate z in the state with the wave function $\Psi_0(z)$.

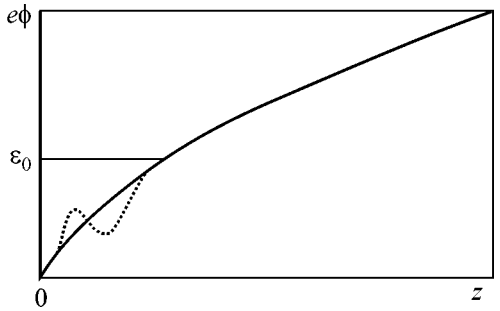

Schematic dependence of the electron potential energy $e\phi$ ($e < 0$) on the coordinate z; the z axis is perpendicular to the semiconductor surface. The solid and dashed lines correspond to two different functions $f(z)$ satisfying Eq. (3).

0021-3640/02/7509-0479$22.00 © 2002 MAIK "Nauka/Interperiodica"

Relationship (3) is proved by the evaluation of the partial derivatives appearing in it followed by the substitution of the resulting expressions in Eq. (3). The derivatives are calculated by linearizing Eq. (1) with respect to the increments ΔE_0, Δn_s, and $\Delta\varepsilon_0$ and to the variation $\Delta\Psi_0(z)$ of function $\Psi_0(z)$. As in the standard perturbation theory, the variation $\Delta\Psi_0(z)$ is expanded in the orthonormalized basis set of eigenfunctions $\Phi_i(z)$ (i is an integer), which, in the case of nonlinear Eq. (1), satisfy the equation

$$-\frac{\hbar^2}{2m}\frac{d^2\Phi_i(z)}{dz^2} + \Phi_i(z)\left[-E_0 z + \frac{2\pi e n_s}{\chi} z + \frac{4\pi e n_s}{\chi}\int_0^z (\Psi_0(u))^2 (u-z)du + f(z)\right] = \lambda_i \Phi_i(z). \quad (5)$$

This is the ordinary Schrödinger equation with a given potential. For the proof given below, it is sufficient to require that all eigenvalues λ_i of Eq. (5) constitute a discrete spectrum. This imposes certain restrictions on the possible form of function $f(z)$, though it is quite probable that the restrictions on the function $f(z)$ satisfying basic relationship (3) may be weaker. Note that the function $\Psi_0(z) = \Phi_0(z)$ also appears in the chosen orthonormalized set of functions $\Phi_i(z)$. Due to normalization condition (2), the variation $\Delta\Psi_0(z)$ is orthogonal to $\Psi_0(z)$, so that

$$\Delta\Psi_0(z) = \sum_{i\neq 0}\alpha_i\Phi_i(z). \quad (6)$$

Here, α_i are the expansion coefficients. The equation obtained by the linearization of Eq. (1) and substitution of Eq. (6) for $\Delta\Psi_0(z)$ is then multiplied by the functions $\Phi_k(z)$ ($k\neq 0$) and $\Psi_0(z)$ and integrated with respect to z. As a result, the problem is reduced, respectively, to an inhomogeneous set of linear equations for the parameters α_i and to an expression for $\Delta\varepsilon_0$. In calculating the derivatives with respect to E_0 and n_s, the corresponding sets of equations have the form

$$\sum_{i\neq 0} b_{ki}\alpha_i^{(E_0)} = e\Delta E_0 B_k, \quad (7)$$

$$\sum_{i\neq 0} b_{ki}\alpha_i^{(n_s)} = -\frac{2\pi e^2}{\chi}\Delta n_s (B_k + 2A_k). \quad (8)$$

Here,

$$b_{ki} = \delta_{ki}(\lambda_k - \varepsilon_0) + \frac{8\pi e^2 n_s}{\chi}\int_0^\infty \Psi_0(z)\Phi_k(z)\times\int_0^z \Psi_0(u)\Phi_i(u)(u-z)dudz, \quad (9)$$

$$A_k = \int_0^\infty \Psi_0(z)\Phi_k(z)\int_0^z (\Psi_0(u))^2 (u-z)dudz, \quad (10)$$

$$B_k = \int_0^\infty \Psi_0(z)\Phi_k(z) z dz. \quad (11)$$

When proving relationship (3), the equalities $b_{ik} = b_{ki}$ and

$$\int_0^\infty (\Psi_0(z))^2\int_0^z \Psi_0(u)\Phi_k(u)(u-z)dudz = A_k + B_k \quad (12)$$

were used, which can easily be verified by changing the order of integration in the corresponding double integrals. It turns out that, to prove Eq. (3), there is no need to know the detailed expressions for the solutions to the set of linear Eqs. (7) and (8). It suffices to write these solutions in a rather general form,

$$\alpha_i^{(E_0)} = e\Delta E_0 \sum_{k\neq 0} c_{ik}B_k, \quad (13)$$

$$\alpha_i^{(n_s)} = -\frac{2\pi e^2}{\chi}\Delta n_s \sum_{k\neq 0} c_{ik}(B + 2A_k), \quad (14)$$

and use the symmetry property $c_{ik} = c_{ki}$ of the coefficients c_{ik}, as follows from the symmetry of coefficients b_{ik}. The validity of Eq. (3) can be checked by substituting into it the following expressions obtained for the partial derivatives using Eq. (12) in accordance with the scheme described above:

$$\frac{\partial\varepsilon_0}{\partial E_0} = -ez_0 + \frac{8\pi e^3 n_s}{\chi}\sum_{i,k\neq 0} c_{ik}B_k(A_i + B_i), \quad (15)$$

$$\frac{\partial z_0}{\partial E_0} = 2\int_0^\infty \Psi_0(z)\frac{\Delta\Psi_0(z)}{\Delta E_0} z dz = 2e\sum_{i,k\neq 0} c_{ik}B_k B_i, \quad (16)$$

$$\frac{\partial z_0}{\partial n_s} = -\frac{4\pi e^2}{\chi}\sum_{i,k\neq 0} c_{ik}(B_k + 2A_k)B_i. \quad (17)$$

When checking, the symmetry of coefficients c_{ik} should be taken into account.

From the mathematical point of view, the invariance of Eq. (3) primarily follows from the fact that it is independent of the form of function $f(z)$ (as long as this function satisfies the conditions discussed above) and parameter m. This expression is also valid for all solutions to Eqs. (1) and (2) and not just for the solution corresponding to the lowest energy ε_0 among the eigenvalues of Eq. (1). The latter of these statements is evident from the fact that, while proving, no restriction was imposed on ε_0.

It is quite probable that relationship (3) reflects the important intrinsic symmetry of the problem. This is indicated, in particular, by the fact that condition (3) is fulfilled not only for the solutions to Eqs. (1) and (2), but also for any normalized one-parametric function with the parameter chosen so as to minimize the functional, whose minimization, generally, results in Eq. (1). In this case, ε_0 is the mean electron energy (kinetic and potential) in the state described by the chosen one-parametric wave function in the potential entering Eq. (1).

The physical meaning of relationship (3) is clear: it relates the size z_0 of the electron localization region in the potential well to the energy of size-quantization level. Note that, if one sets $n_s = 0$ in Eq. (3), then one obtains the well-known relation [1] for the triangular potential well, which arises in Eq. (1) if $f(z) = 0$. Moreover, in the triangular well, the obtained relationship is valid for all energy levels. The distinguishing feature of the physical problem with $n_s \neq 0$ is that, in the case of filling higher size-quantized subbands, initial Eq. (1) should be replaced by the set of equations for the electron wave functions in different subbands. So, for $n_s \neq 0$, condition (3) is only met if electrons fill the lowest size-quantized subband with the bottom at ε_0.

By way of illustration of the above general statement about one-parametric functions, one can easily verify that Eq. (3) is fulfilled, in particular, for the Fang–Howard variational function $\xi(z) = (b^3/2)^{1/2} z \exp(-bz/2)$, which is widely used in the analysis of quasi-two-dimensional electron systems near the semiconductor surface [1]. One has for this function $z_0 = 3/b$, and the expression for the subband bottom energy can be taken in the form [1] $\varepsilon_0 = \hbar^2 b^2/8m + 12\pi e^2 N_{\text{depl}}/\chi b + 33\pi e^2 n_s/4\chi b$ (N_{depl} is the surface density of charged impurities in a depleted layer lying at $z \gg z_0$), with $N_{\text{depl}} = -\chi E_0/4\pi e - n_s/2$. The value of $b_{\min}$ minimizing the total energy of the electron system is [1]

$$b_{\min} = (48\pi m e^2 N^*/\chi\hbar^2)^{1/3}, \tag{18}$$

where $N^* = N_{\text{depl}} + (11/32)n_s$.

The form of invariant (3) changes if additional terms depending on E_0, n_s, or $\Psi_0(z)$ appear in Eq. (1). In this connection, it is worthwhile to give an expression for the invariant corresponding to the equation obtained by the minimization of the energy functional that is more appropriate to the experimental situation. This equation differs from Eq. (1) by the additional term

$$-\frac{\hbar^2}{2m}\frac{d^2\Psi_0(z)}{dz^2} + \Psi_0(z)e\left[-E_0 z + \frac{2\pi e n_s}{\chi} z + \frac{4\pi e n_s}{\chi}\int_0^z (\Psi_0(u))^2 (u - z)\,du - \frac{2\pi e n_s}{\chi}\int_0^\infty (\Psi_0(z))^2 z\,dz + f(z)\right] = \varepsilon_0 \Psi_0(z). \tag{19}$$

The invariant for this equation is obtained in perfect analogy to Eq. (3):

$$\frac{\partial \varepsilon_0}{\partial E_0} + e z_0 + e n_s \frac{\partial z_0}{\partial n_s} = 0. \tag{20}$$

Note in conclusion that the existence and the form of Eqs. (3) and (20) were "guessed" when analyzing our experimental results, which will be published in the immediate future.

I am grateful to S.V. Iordanskiĭ and V.E. Bisti for helpful discussions. This work was supported by the Russian Foundation for Basic Research and the INTAS.

REFERENCES

1. T. Ando, A. B. Fowler, and F. Stern, Rev. Mod. Phys. **54**, 437 (1982); T. Ando, A. B. Fowler, and F. Stern, in *Electronic Properties of Two-Dimensional Systems* (Mir, Moscow, 1985).

Translated by V. Sakun

JETP Letters, Vol. 75, No. 9, 2002, pp. 482–486. From Pis'ma v Zhurnal Éksperimental'noĭ i Teoreticheskoĭ Fiziki, Vol. 75, No. 9, 2002, pp. 573–577.

Two-Dimensional Ordering of Inclusions in Smectic C Phase[1]

P. Cluzeau[1], G. Joly[1], H. T. Nguyen[2], and V. K. Dolganov[3]

[1] *Laboratoire de Dynamique et de Structure des Matériaux Moléculaires, ESA CNRS 8024, Université de Lille I, 59655 Villeneuve d'Ascq Cedex, France*

[2] *Centre de Recherche Paul Pascal, CNRS, Université de Bordeaux I, F-33600 Pessac, France*

[3] *Institute of Solid State Physics, Russian Academy of Sciences, Chernogolovka, Moscow region, 142432 Russia*

Received April 3, 2002

The organization of inclusions nucleated in free standing films of smectic C (SmC) liquid crystal is investigated using polarized light microscopy. Anchoring on the inclusion boundaries induces distortions of the in-plane orientational order of the SmC phase, which drive the elastic interactions between inclusions. Such interactions show a quadrupolar character. At low concentration, the inclusions self-organize in linear or branched chain structures, while at high concentrations two-dimensional patterns appear in the film. © *2002 MAIK "Nauka/Interperiodica".*

PACS numbers: 61.30.Jf; 68.55.Ln

The collective behavior of dispersions of particles in a host fluid has been the subject of great interest over the past decade for science and technology [1–3]. In recent years, liquid crystals have become model objects for those investigations. The first reason is that, in liquid crystals, effective interaction between the particles is realized via distortions of molecular ordering. The second reason is that the inclusions and the resulting elastic deformation of the director field can be easily visualized optically with a polarizing microscope. In the field of liquid-crystal emulsion (i.e., water or silicone oil droplets dispersed in a nematic host phase), the investigations give evidence of long-range attraction and short-range repulsion between droplets, which lead to the formation of linear chains [1, 4–6].

Most of the previous investigations have been devoted to systems in which the director configuration around a particle is homeotropic, i.e., perpendicular anchoring of the molecules at a particle surface. It was shown that, if the particle is placed into a uniformly aligned director field, a topological defect is created in the film in order to compensate the topological charge of the particle [7]. The particle and its associated defect form a topological dipole which drives long-range attraction between particles. Dipolar interactions between droplet-defect pairs lead to the formation of linear chains of droplets separated by point topological defects. Such chains were first observed in nematic (N) liquid-crystal emulsion [1, 4–6] and, recently, in two-dimensional chiral smectic (SmC*) free-standing films [8, 9]. In the former, the preferred direction of the alignment of molecules is specified by the unit-vector field **n** called the director. In smectic C (SmC) phase, each layer is a two-dimensional anisotropic liquid with rod-like molecules tilted in a given direction, the in-plane orientational order of the molecules in the smectic layers being specified by the so-called **c** director (projection of the average direction of the long molecular axis onto the layer plane).

In this paper, we present an investigation of particles in nonchiral smectic films with another type of interparticle interaction. These particles exhibit planar anchoring of the **c** director, i.e., parallel to the particle's surface. We observed the formation of both linear structures and a two-dimensional periodic lattice. The liquid crystal studied in our experiments was decyl oxybenzoic acid (DOBA), which exhibits the following phase sequence: crystal–SmC–N–I [10]. We used a material slightly doped with ethyldecyloxybenzoate both to decrease the temperature of nucleation of the inclusions and to increase the temperature range of stability of the inclusions in the films. In a bulk sample of this mixture, the SmC–N phase transition ranges from 114°C to 117°C. In thick free-standing films, the nucleation of inclusions begins just above 114°C. Free-standing films were prepared by drawing a small amount of liquid crystal in the SmC phase across a 4-mm hole in a glass plate. The experiments were carried out on films with a thickness from 1 to 3 μm. The temperature was controlled to within ±10 mK. Microscopic observations were performed in reflected light between crossed polarizers, and the texture varied from dark to bright according to the position of the **c** director with respect to the polarizers. A video camera enabled dynamic observations. The determination of the film thickness and the direction of the **c**-director field was obtained from the reflection spectrum measurements.

Figure 1 presents pictures of the droplets between crossed polarizers. Observations for two orientations of the film [the **c** director at 45° (Fig. 1a) and parallel

[1] This article was submitted by the authors in English.

(Fig. 1b) to the polarization of incident light] provide more information about the distribution of the **c** director-field deformation near the droplets. In dark regions in Fig. 1a and in bright ones in Fig. 1b, the **c** director is rotated by about 45° with respect to its direction at long distances from the inclusion. Careful observation of Fig. 1b reveals that the deformation of the **c** director field around the inclusion is not equivalent along the vertical and horizontal directions. Two peculiarities are attached on the left and right sides of the droplet boundary. Note that the orientation of the symmetry axis connecting these antipodal points is parallel to the **c**-director field in the film.

The analysis of the process of nucleation and growth of droplets showed that the boundary of a droplet is a defect line with a tangential boundary condition. Droplets nucleate inside a short double line and two parts of the defect line become the droplet boundary forming a loop. The director configuration around particle is homogeneous. There is only a breaking in the direction of tangential anchoring at the opposite points of the droplet boundary, in which the ends of two line defects surrounding the droplet are connected. The dependence of surface droplet energy, defect line tension, and elastic energy on the inclusion dimension leads to a change of the droplet shape. Small droplets (less than 15 μm) can have a slightly elliptical form with the long axis oriented along the **c** director. Large droplets (above 15 μm) are almost ideally circular (Fig. 1b). It is worth mentioning that the droplet in Fig. 1a also has a circular shape. However, it appears elliptical because the darkened regions occupy areas inside the droplet as well as outside. Circular inclusions may be conceived as oblate spheroids with the short axis slightly larger than the film thickness. The deformation of the film at the place of inclusion is visible by observing the interference fringes in monochromatic light. Concerning the nature of the inclusions, both the temperature of nucleation and the spheroid shape of the inclusions strongly suggest that the local order in the inclusion is nematic. In the case of smectic order in the inclusion, we would obtain a circular island of greater thickness than the background film [9]. Such an island exhibits a flat surface instead of a spheroid shape. The stability of the film is ensured by smectic layers surrounding the inclusion. Indeed, the air–liquid crystal interface is known to promote the smectic order.

Figure 2a schematically describes the director field around the droplet with planar anchoring on the particle surface. The distortion near the singular points (M and N) is drawn in Fig. 2b. The distribution of the director field near these points corresponds to a topological defect with a strength equal to 1/2. Note that the symmetry of the **c** director in the SmC phase does not permit the isolated 1/2 defect in the bulk of the liquid crystal. However, such defects can exist when attached to a surface—in our case, to the inclusion boundary. The presence of a pair of singularities on the particle boundary preserves the zero topological charge of the film.

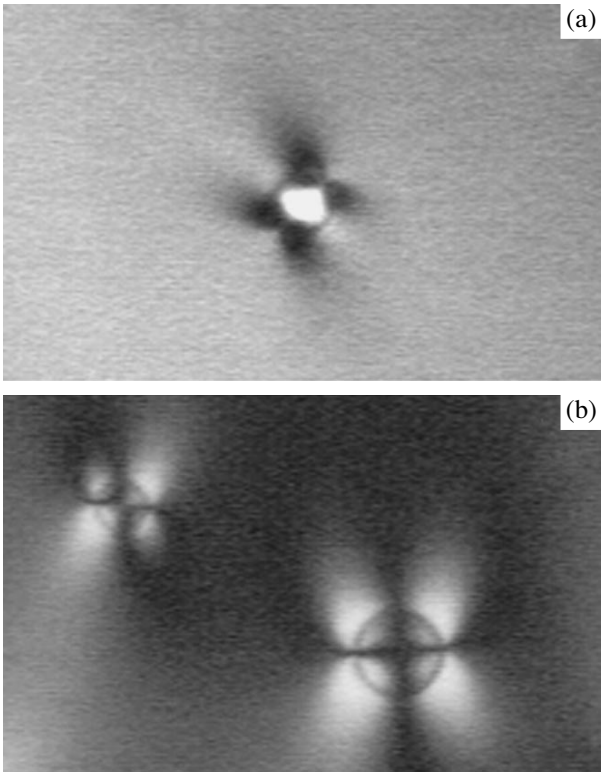

Fig. 1. Microscope picture of a single inclusion in the SmC free-standing film observed under crossed polarizers (horizontal and vertical); (a) and (b) figures correspond to the **c** director, respectively, at 45° and parallel to the polarization of the incident light. $T = 114.2°C$. The horizontal size of each image is about 130 μm.

Zones with a small distortion of the director field near each droplet are well seen in Fig. 1b: (i) two acute zones starting from the opposite point defects; (ii) two larger zones in the orthogonal direction. As mentioned above, strong distortion of the **c**-director field is mostly located in dark regions in Fig. 1a and in bright regions in Fig. 1b. These directions are expected to be the directions of attraction between neighboring inclusions. Spatial ordering of inclusions at the equilibrium distance should minimize the **c**-director deformation with respect to two isolated inclusions. Indeed, if several particles are nucleated, they generally form chains (Fig. 3). The formation of chains from spherical particles with planar anchoring was already observed in inverted emulsion (water droplets suspended in nematic liquid crystals) [4]. However, in chains, water droplets come into contact with one another, which quickly leads to droplet coalescence. In smectic films, chains can be stable for a long time. Distortion of the director field is easily observed near the chains (Fig. 3). A schematic drawing of the director field is given in Fig. 2c. The chains form an angle of about 40° with the **c** director. Between the inclusions, the **c**-director field has approximately the same direction coinciding with the

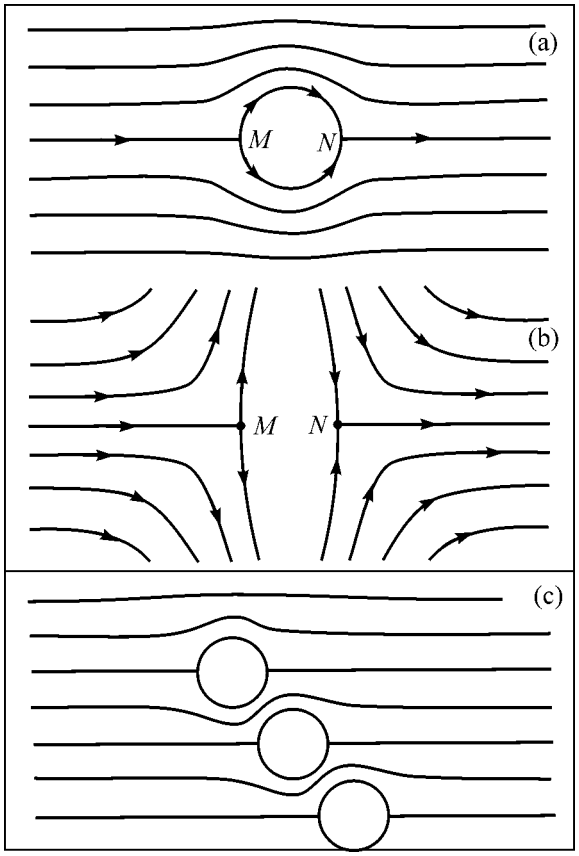

Fig. 2. Schematic representation of the distortion of the director field induced by inclusions; (a) and (b) figures correspond to the **c**-director configuration, respectively, near the single inclusion and near point disclinations. Two surface defects (*M* and *N*) are induced at the surface of the inclusion; (c) **c**-director field configuration induced by a chain of inclusions.

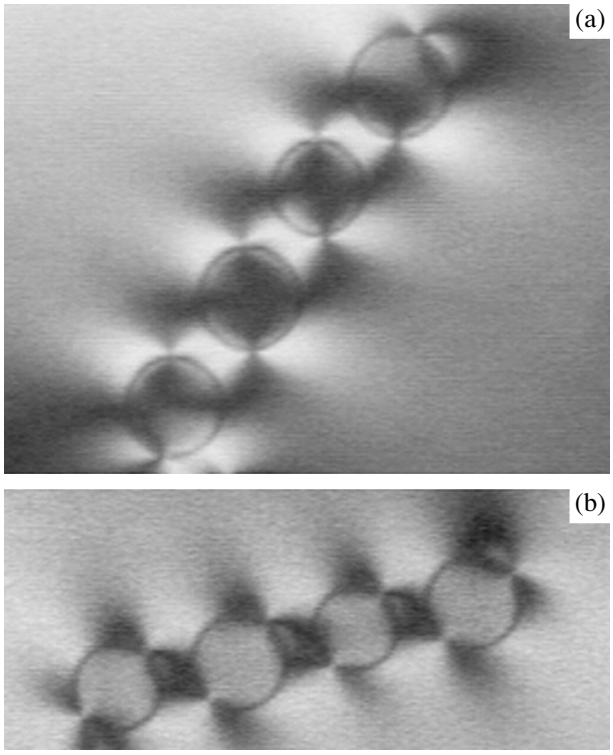

Fig. 3. Microscope picture of a chain of four inclusions. Polarization of the insident light is along the horizontal axis. T = 115.5°C. The horizontal size of each picture is about 130 μm.

direction of planar anchoring at the inclusion boundary. Such organization of inclusions minimizes the deformation of director field in the film.

Interaction between particles with planar anchoring is of the quadrapolar type [11]. This type of interaction leads to a higher possibility of structural organization than the dipolar type. In this latter case, the attraction is maximal along the axis of the topological dipole, i.e., along the **c**-director orientation at a long distance [1, 8, 9]. The formation of linear chains is then a consequence of dipolar symmetry. The positions of two particles on both sides of a third one (central) are equivalent if the particles are located along a straight line. In the case of quadrupolar interaction, there are two directions and, respectively, four positions of particles along which neighboring particles may be located. Figure 4a shows bent chains. They appear when one of the particles is located in a nonequivalent position. Figure 4b shows two adjoint chains. The distances between particles in a chain and between the chains are practically identical.

At high droplet density, a two-dimensional, spatially oriented structure is built (Fig. 5a, inclusions have a slightly oblong shape). Such a degree of organization can only be achieved if all particles exhibit approximately the same size. These structures exhibit spatial ordering of the **c**-director configuration in the film and orientational ordering of inclusions: lines connecting singular points at the inclusion boundary are oriented in a specific direction (the vertical direction in Fig. 5a). A part of the film with two-dimensional ordering of circular particles is shown in Fig. 5b. Generally, the nucleation of large particles leads to a distribution of the particle size which prevents the formation of a large-scale well-organized structure. The different orientations of the **c**-director field between droplets are clearly visualized upon the observation between crossed polarizers (Fig. 5). A schematic representation of the director field between the particles is given in Fig. 5c. Regions with nearly parallel orientation of the **c** director are located between the nearest particles (dark regions in Fig. 5a) and on the diagonals (dark regions in Fig. 5b). However, these regions have different orientations of the **c** director. This means that the **c** director does not keep the average direction over the whole area of the film. The presence of neighboring inclusions disturbs the pair interactions. As a consequence, binary interaction between inclusions, usually used for modeling, is insuf-

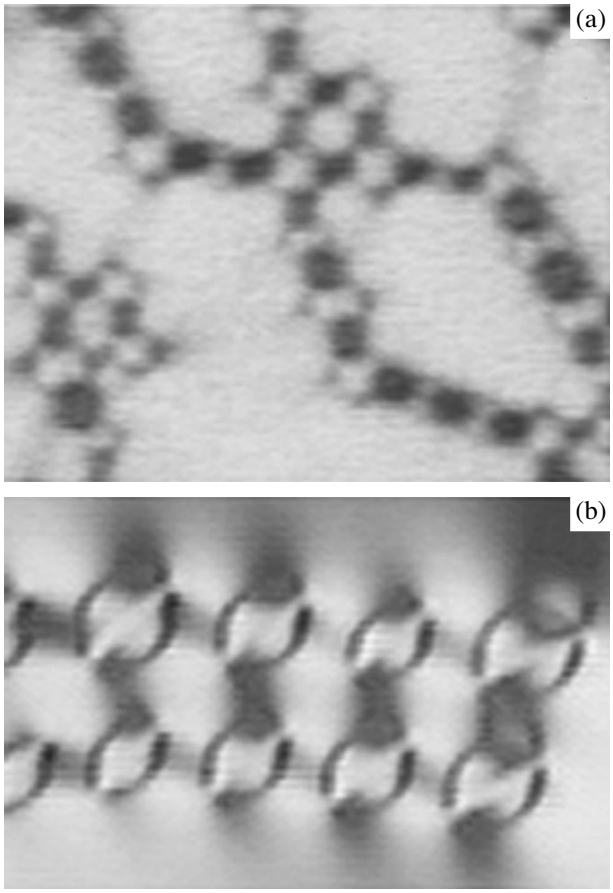

Fig. 4. Microscope picture, between crossed polarizers, of complex structures formed by inclusions. Due to the quadrupolar character of the interactions, the particles can have different positions with respect to the next neighboring particle. $T = 116.1°C$. The horizontal size is about 130 μm.

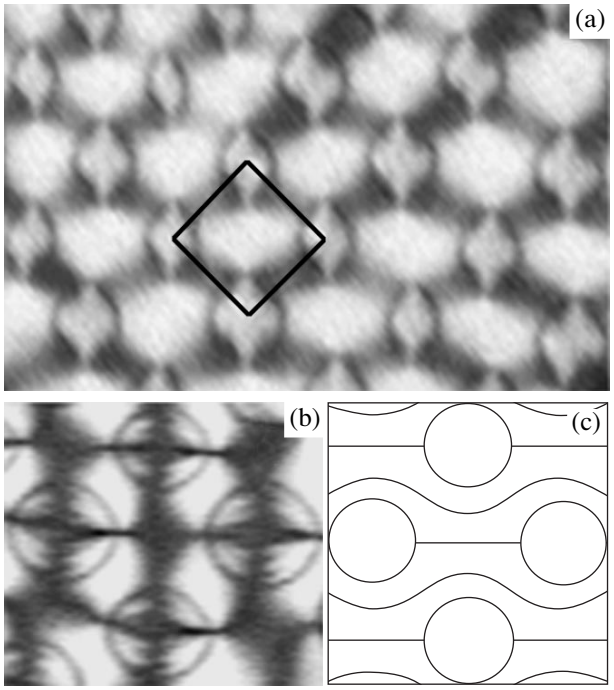

Fig. 5. (a) Two-dimensional ordering structure formed by inclusions. The structure is formed by slightly oblong inclusions. The square gives the unit pattern of the structure. The horizontal size is about 90 μm. (b) Part of the two-dimensional structure formed by circular inclusions. $T = 116.6°C$. The horizontal size is about 50 μm. The polarizer is (a) at 45° with respect to the horizontal axis and (b) along the horizontal axis. Schematic representation of the **c**-director field for a two-dimensional structure (c).

ficient for describing two-dimensional spatial and orientational ordering of inclusions.

In this paper, we have studied the behavior of nematic inclusions nucleated at the SmC-N transition in two-dimensional ordered free-standing films. After the nucleation process, spatially inhomogeneous inclusion distribution is achieved due to both long-range attractive and short-range repulsive interactions between particles. Such interactions result from the elastic deformation of the **c**-director field induced by the tangential **c**-director anchoring at the inclusions boundary. It should be noted that, in theoretical work [7], simulations of radial and tangential anchoring are treated and both lead to a –1 hyperbolic point defect associated with the inclusion. As a result, the inclusion defect pairs always exhibit the dipolar symmetry, and the radial and tangential anchoring only differ by the orientation of the topological dipole, respectively, parallel or normal to the **c**-director field far from the inclusion. In our experiments, we observed two 1/2 defects attached to the surface of the inclusion. The structural organization shows a quadrupolar interaction, which drives the formation of more complex structures than in the dipolar case. According to the inclusion densities, different types of structure can be achieved: at a low inclusion density, linear and bent chains are built, while, at high density, we observe two-dimensional pattern resulting from positional and orientational ordering of the inclusions. This study underlines the influence of anchoring conditions at the inclusion boundary on the type of interaction. The dynamics of self-organization and a model of interactions between inclusions are under investigation. The confrontation of the quadrupolar and dipolar interaction in free-standing films provides an important basis for a more general understanding of the behavior of colloidal inclusions in membranes and two-dimensional films, such as Langmuir films or biological phospholipid bilayers.

We thank L. Lejcek and P. Poulin for helpful discussions. V.D. is grateful to the University of Lille I and their Laboratoire de Dynamique et Structure des Materiaux Moleculaires for the hospitality. This work was supported by the Russian Foundation for Basic Research, project no. 01-02-16507 (V.D.).

REFERENCES

1. P. Poulin, H. Stark, T. S. Lubensky, and D. A. Weitz, Science **275**, 1770 (1997).
2. A. P. Ruhwandl and E. M. Zukoski, Adv. Colloid Interface Sci. **30**, 153 (1989).
3. W. B. Russel, D. A. Soville, and W. R. Schowaiter, *Colloidal Dispersions* (Cambridge Univ. Press, Cambridge, 1989).
4. P. Poulin and D. Weitz, Phys. Rev. E **57**, 626 (1998).
5. T. C. Lubensky, D. Pettey, and N. Currier, Phys. Rev. E **57**, 610 (1998).
6. J-Ch. Loudet, P. Barois, and P. Poulin, Nature **407**, 611 (2000).
7. D. Pettey, T. C. Lubensky, and D. R. Link, Liq. Cryst. **25**, 579 (1998).
8. P. Cluzeau, P. Poulin, G. Joly, and H. T. Nguyen, Phys. Rev. E **63**, 031702 (2001).
9. P. Cluzeau, V. Dolganov, P. Poulin, *et al.*, Mol. Cryst. Liq. Cryst. **364**, 381 (2001).
10. D. Demus, *Flüssige Kristalle in Tabellen* (VEB Deutscher fur Grundstoff Industrie, Leipzig, 1974); M. Petrov, A. Braslou, A. M. Levelut, and G. Durand, J. Phys. II **2**, 1159 (1992).
11. S. Ramaswamy, R. Nityananda, V. A. Raghunathan, and J. Prost, Mol. Cryst. Liq. Cryst. Sci. Technol., Sect. A **288**, 175 (1996).

JETP Letters, Vol. 75, No. 9, 2002, pp. 487–491. Translated from Pis'ma v Zhurnal Éksperimental'noĭ i Teoreticheskoĭ Fiziki, Vol. 75, No. 9, 2002, pp. 578–583.

Ultrafast Faraday Effect and the Dynamics of the Antiferromagnet–Paramagnet Phase Transition in $FeBO_3$

A. V. Kimel'[1]*, R. V. Pisarev[1], J. Hohlfeld[2], and Th. Rasing[2]

[1]*Ioffe Physicotechnical Institute, Russian Academy of Sciences, Politekhnicheskaya ul. 26, St. Petersburg, 194021 Russia*
**e-mail: kimel@pop.ioffe.rssi.ru*
[2]*Research Institute for Materials, University of Nijmegen, 6525 ED Nijmegen, Netherlands*
Received April 5, 2002

The optical pump–probe technique using ultrashort laser pulses with a photon energy of 1.55 eV was used to study the dynamics of the antiferromagnet–paramagnet phase transition in $FeBO_3$. The Faraday magneto-optical effect was measured with a time resolution of 100 fs, and signal transients were observed as functions of sample temperature. The rate of photoinduced phase transition was shown to be limited by the phonon–magnon relaxation rate with a characteristic time of 700 ps. The subpicosecond dynamics of Faraday rotation is not associated with the destruction of magnetic order but is caused by electron photoexcitation and recombination.

PACS numbers: 75.30.Kz; 42.65.Re; 78.20.Ls; 71.36.+c; 75.50.Ee

The invention of lasers generating pulses with a duration of 100 fs and shorter gave impetus to the study of ultrafast processes in the electron, phonon, and spin subsystems of solids. Over a long period of time, the methods of ultrafast spectroscopy were successfully exploited to study the dynamics of photoinduced magnetization and other nonequilibrium processes in semiconductors [1]. However, works on the ultrafast dynamics of nonequilibrium processes in magnetically ordered media, where photoexcitation can change or even destroy the magnetic order, have been initiated only recently and are, as yet, few in number. One of the first works in which the rate of magnetic order destruction was considered was devoted to the study of ferromagnetic nickel [2]. In that work, the conclusion was drawn that the characteristic heating time of a spin subsystem is much longer than 10 ps. However, it was claimed shortly afterwards that the magnetic order in Ni can be controlled on the subpicosecond time scale [3, 4], and the assumption was made that there is an efficient energy-exchange channel between electrons and magnons [3]. Subsequent studies both confirmed the possibility of demagnetization on the subpicosecond time scale and argued against this phenomenon [7, 8]. These contradictions can be resolved only by continuing the studies of demagnetization dynamics in other groups of materials where this phenomenon has not yet been investigated. The promising objects for these studies can be provided by antiferromagnetic dielectrics, where the demagnetization processes have not been studied so far. Theoretical works predict that the demagnetization times in these materials may be shorter than 100 fs. Estimates were made for the antiferromagnetic nickel oxide dielectric NiO [9]; however, the experimental study of this material is hampered because of the complexity of its domain structure and the absence of linear magneto-optical effects.

To overcome these technical and, to some extent, fundamental difficulties, the antiferromagnetic iron borate dielectric was chosen in our investigations. This compound crystallizes in the calcite structure with space group $R\bar{3}c$ and has a Néel temperature T_N = 348.35 K [10]. Its antiferromagnetic state is characterized by a weak ferromagnetic moment arising because of a spin disorientation by an angle of 1° in the (111) plane. Due to this moment, the sample can be brought to a single-domain state by a weak external magnetic field. Consequently, the magnetic order in such an uncompensated antiferromagnet can be probed using linear magneto-optical effects.

The optical properties of $FeBO_3$ in the visible range are determined by the localized *d* states of the Fe^{3+} ion in the crystal field (Fig. 1a). In the free Fe^{3+} ion, five *d* electrons constitute a high-spin ground state ^6S (L = 0 and S = 5/2), i.e., orbital singlet and spin sextet. The ^4G state is the nearest excited state. In the octahedral crystal field, the excited state splits into two triplets $^4\Gamma_4^+$ and $^4\Gamma_5^+$, a $^4\Gamma_3^+$ doublet, and a $^4\Gamma_1^+$ singlet. The spin degeneracy is removed by the spin–orbit and exchange interactions. The electric dipole transitions $^6\Gamma_1^+ \longrightarrow {}^4\Gamma_4^+$ and $^6\Gamma_1^+ \longrightarrow {}^4\Gamma_5^+$ from the ground to excited states are forbidden due to the parity and spin selection rules. Nevertheless, four strong lines are observed in the absorption spectrum at 20 K in the region of the first *d–d*

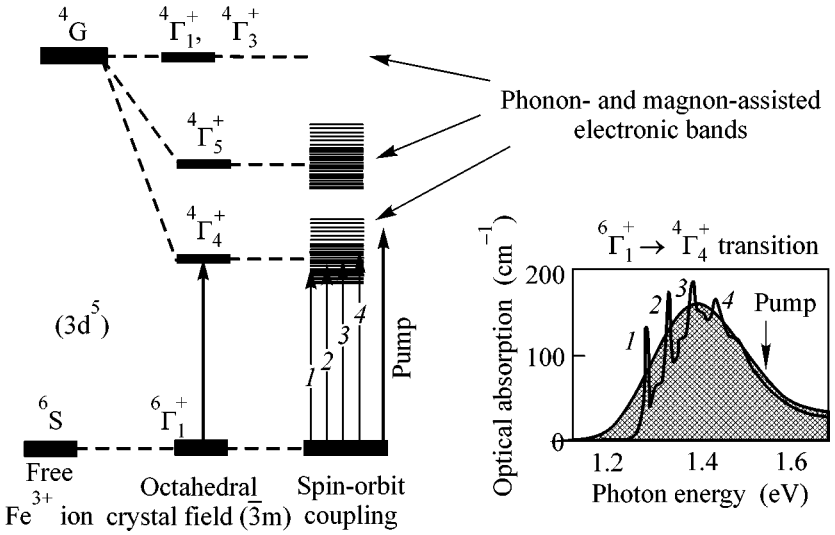

Fig. 1. (a) Energy levels of the Fe^{3+} ion in $FeBO_3$ and (b) absorption spectrum of $FeBO_3$ at (solid line) room temperature and (dotted line) 20 K.

transition (Fig. 1b). At higher temperatures, this splitting smears because of a strong electron–phonon interaction and electron–phonon transitions.

A 300-μm-thick platelet-shaped iron borate sample with the basal plane perpendicular to the optical axis was used in our study. Measurements were made by the optical pump–probe technique using the amplified pulses from a titanium–sapphire laser with a photon energy of 1.55 eV, a pulse duration on the order of 100 fs, and a repetition rate of 1 kHz (Fig. 2). The pump and probe beams were linearly polarized and focused onto the same area of the sample so that the ratio of their intensities was 10 : 1. The spatial radiant exposure per pump pulse was about 30 mJ/cm^2. The angles of incidence for the pump and probe beams were 0° and 20°, respectively. In this geometry, the probe beam after passing through the sample should exhibit the linear magneto-optical Faraday effect, i.e., rotation of the polarization plane by the angle

$$\alpha_F = VML\cos\theta, \qquad (1)$$

where V is the Verdet constant, M is the sample magnetization, L is the geometrical optical path in the sample, and θ is the angle between the magnetization and the light wave vector in the sample. The dynamics of antiferromagnetic order destruction in $FeBO_3$ was studied by measuring the Faraday rotation as a function of the delay time between the pulse and probe pulses. The sample was placed in an ac magnetic field with an amplitude of about 100 Oe and a frequency of 194 Hz. The rotation of the polarization plane was measured at this frequency with a sensitivity no worse than 0.2 mrad using a two-photodiode balanced detector and the lock-in detection technique. Provision was made for varying the sample temperature T_{bias} using a heater. The absorption of pump light brought about static local superheating of the sample by 10 K, which was taken into account by introducing the appropriate correction.

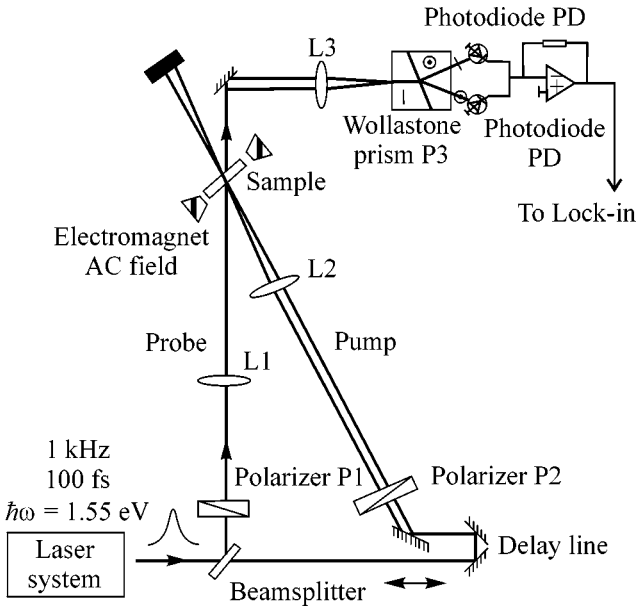

Fig. 2. Scheme of the experimental setup.

As known, optical pumping can alter not only the magnetic but also optical properties of solids. In studying the dynamics of Faraday rotation, it is necessary to measure the photoinduced variations in the sample transmission and use these data for calibration. The transmission transients were measured using a single-

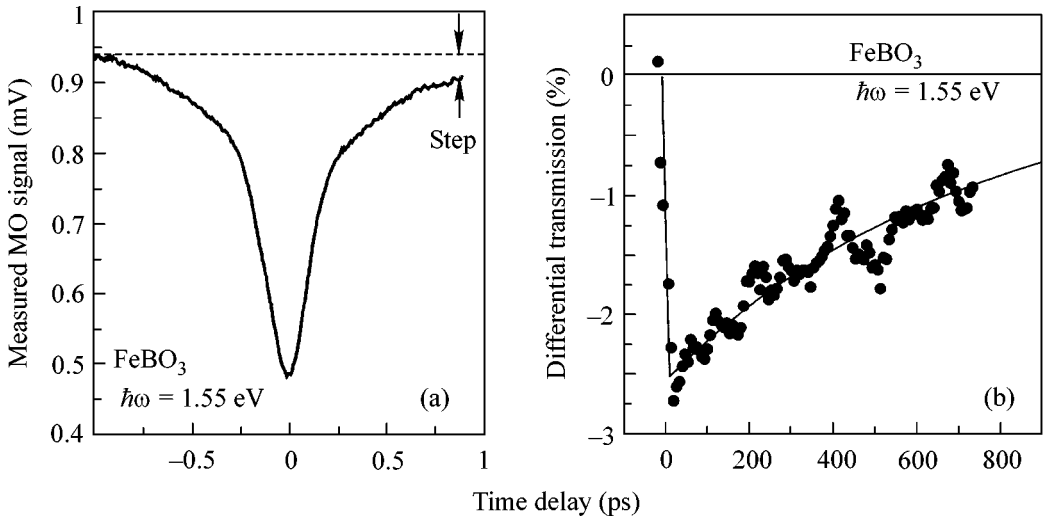

Fig. 3. (a) Photodetector signal as a function of time on a time interval of 1 ps and (b) time behavior of the photoinduced differential transmission.

photodiode scheme with amplitude modulation of the probe beam.

The short-time behavior of the magneto-optical signal is shown in Fig. 3a. The signal drops dramatically when the pump and probe pulses overlap, whereupon it is rapidly restored. For a time delay of about 900 fs, the signal tends to saturation at a level 2–3% lower than before the photoexcitation. Such a behavior of the magneto-optical effect was already observed for the Sr_2FeMoO_6 ferrimagnet [5] and interpreted as ultrafast medium demagnetization. After supplementary studies, we established that this behavior is caused not by the magnetization dynamics but by the photoinduced changes in transmission (Fig. 3b) and by the fact that the signal from the balanced detector linearly depends on intensity. After the transmission dynamics is taken into account in the calibration, the stepwise contribution disappears, while the peak corresponding to the overlap of the pump and probe pulses is retained. In this work, the peak was measured as a function of intensity. Such an ultrafast response in the Faraday effect is proportional to the spatial radiant exposure with a coefficient of $(8 \pm 0.6) \times 10^{-5}$ rad cm^2/mJ.

The long-time behavior of Faraday rotation is shown in Fig. 4 for various temperatures gradually approaching the Néel point. The closer the sample temperature to the Néel point, the more pronounced the dynamic variations in the Faraday rotation. At T_{bias} = 346.5 K, the signal sharply drops within 500 ps, after which it becomes zero.

The temperature dependence of Faraday rotation for the negative delay time is shown in Fig. 5. Considering that the Faraday rotation is proportional to the order parameter, the temperature dependence of the magneto-optical signal can be approximated by the function

$$\alpha_F(T) = \alpha_0(1 - T_s/T_N)^{\beta}, \quad (2)$$

where T_N is the Néel temperature, β is the critical exponent, and T_s is the magnon temperature, which determines the magnitude of the order parameter. The fitting procedure gave $T_N = 347.0 \pm 0.1$ K and $\beta = 0.36 \pm 0.01$. These results are in good agreement with the values $T_N = 348.35$ K and $\beta = 0.354$ reported in [10]. A small distinction in the Néel temperatures can be attributed to the static heating of the sample by the probe beam. The result of the fitting procedure is shown in Fig. 5 by the solid line.

The temperature dependence of the Faraday rotation for zero delay time is shown in Fig. 5 by empty circles. The experimental data were approximated by Eq. (2) using the β and T_N values given above. The result of this approximation is shown in Fig. 5 by the dotted line. The fact that the temperature dependences of Faraday rotation are similar for the negative and zero delay times indicates that the overlap peak is not associated with the destruction of magnetic order, but is caused by the transition of Fe^{3+} ions to the low-spin state $S = 3/2$ and by the photoinduced change in the Verdet constant [11, 12].

The difference between the magneto-optical signals with delay times of –20 and 500 ps is shown in the same graph. One can see that this difference increases as the Néel temperature is approached. Qualitatively, it reproduces the derivative of the Faraday rotation or order parameter with respect to temperature. These factors taken together indicate that the photoinduced change in the magneto-optical signal is due to the rise in magnon temperature. Consequently, for the sample temperature

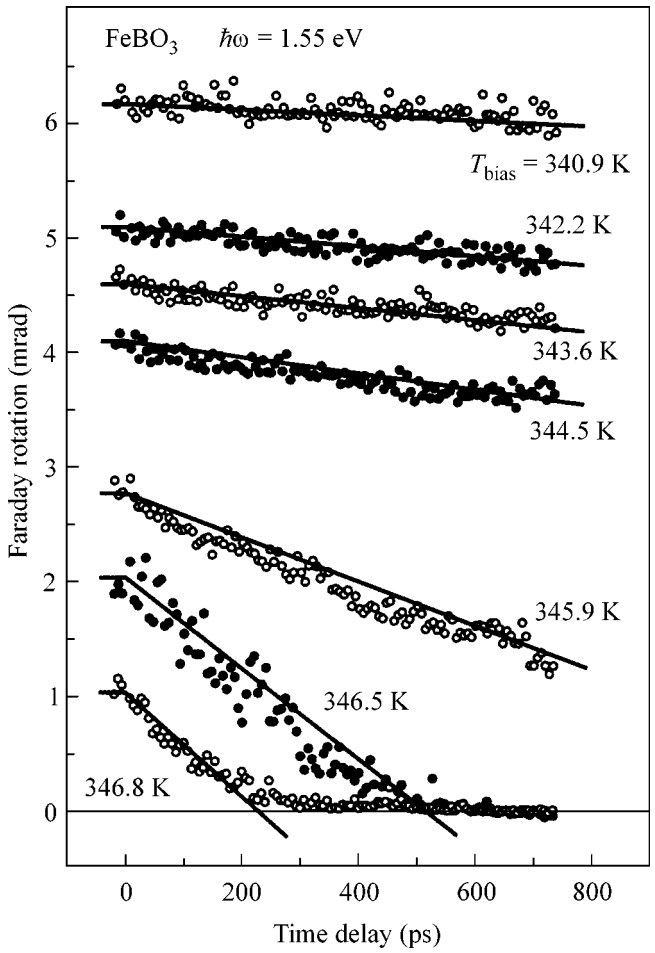

Fig. 4. Long-time behavior of the Faraday rotation.

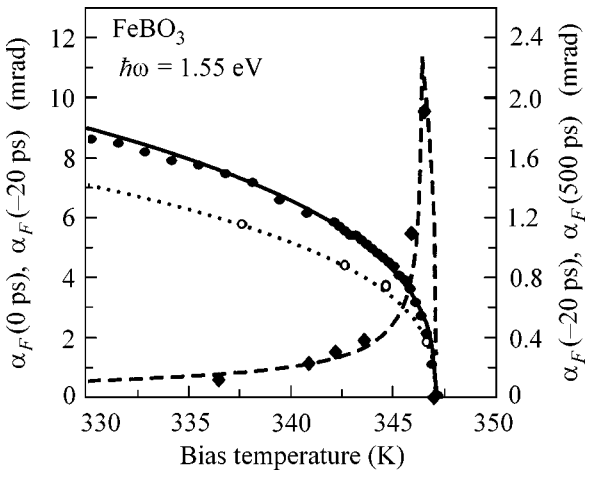

Fig. 5. Faraday rotation as a function of temperature T_{bias} for the [black dots; $\alpha_F^{(0)}$] negative and [empty dots; $\alpha_F^{(-20)}$] zero delay times, and the result of fitting Eq. (2) to the experimental data (solid and dotted lines, respectively). The difference between the magnitudes $\alpha_F^{(-20)}$ and $\alpha_F^{(500)}$ of the Faraday rotation for – 20 and 500 ps is shown by the rhombi together with the calculated curve (dashed line).

T_N = 346.5 K and a delay time of 500 ps, the magnon temperature achieves the Néel temperature and the antiferromagnetic order is destroyed.

The transient magnon temperature $T_s(t)$ can be represented as the sum of static temperature T_{bias} and the dynamic component $\Delta T_s(t)$. Therefore, each of the magneto-optical signal transients can be represented as the dynamic temperature $\Delta T_s(t)$. In the range of temperatures T_{bias} studied, the dependences $\Delta T_s(t)$ were identical to within experimental error. All $\Delta T_s(t)$ dependences were averaged, and the result is shown by the black dots in Fig. 6. Inasmuch as the averaged dynamic component increased monotonically, these data were approximated by the formula

$$\Delta T_s(t) = Tm_s\left(1 - \exp\left(-\frac{t}{\tau_T}\right)\right), \qquad (3)$$

where Tm_s is the amplitude of the dynamic component and τ_T is the heating rate. When fitting, all parameters were taken to be variable, and the result for Tm_s = 1.4 K and τ_T = 700 ps is shown in Fig. 6 by the solid line.

Making use of the resulting parameters Tm_s, τ_T, and α_0, one can determine the difference between the magneto-optical signals for –20 and 500 ps. This difference is shown as a function of temperature by the dashed line in Fig. 5. The experimental data agree well with the calculation. This justifies the statement that the relaxation of the magneto-optical signal is caused by the increase in magnon temperature.

The absorption spectrum of $FeBO_3$ indicates that photons with an energy of 1.55 eV mainly induce the ${}^6\Gamma_1^+ \longrightarrow {}^4\Gamma_4^+$ transition. As a result of this excitation, the iron ions undergo a transition to the low-spin state S = 3/2 and the electron potential energy increases, on average, by 1.4 eV. The remaining of photon energy is transferred to the lattice and to the magnetic system as a result of the electron–phonon and electron–magnon interactions. From the line width near 1.4 eV in the room-temperature absorption spectrum of $FeBO_3$, one can see that the lifetime of the Fe^{3+} ions in the low-spin state S = 3/2 does not exceed 100 fs. The electron relaxation to the ground high-spin state S = 5/2 may be both radiative and nonradiative. As a result of the latter process, the electron energy dissipates to the lattice.

As a rule, the electron–phonon transitions are more intense than the electron–magnon transitions [13]. Consequently, the phonon temperature after photoexcitation is higher than the magnon temperature, so that the equilibrium is disturbed. Thereupon the difference starts to decrease gradually, while the magnon temperature increases with the phonon–magnon relaxation rate.

The previous investigations of magnetization reversal in iron borate using microwave pulses have shown that the $FeBO_3$ lattice is isolated from the magnetic sub-

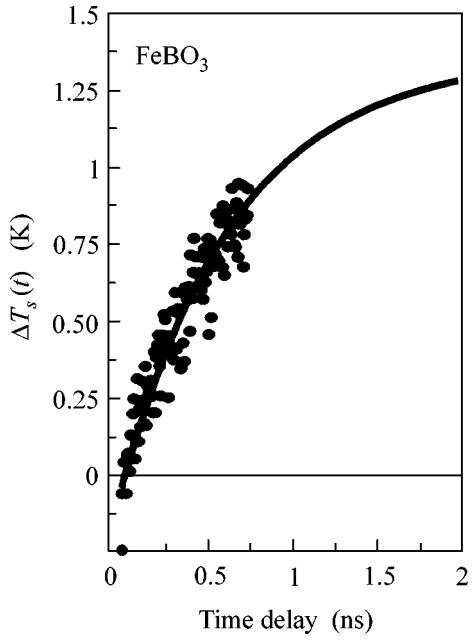

Fig. 6. Time-dependent dynamic component ΔT_S of the magnon temperature. Solid line is the approximation by Eq. (3).

system during 16 ns after the excitation [14]. This value is 20 times as large as the phonon–magnon relaxation time observed in our experiments (τ_T = 700 ps). A difference as large as this may be due to the fact that the phonon–magnon interaction depends on the magnon wave vector. In the microwave experiments, magnons with only small or zero wave vectors are involved, whereas, in our experiment, the energy exchange with the lattice occurs throughout the entire magnon spectrum. Therefore, the phonon–magnon relaxation rates determined by these two methods may markedly differ from each other.

In this work, the dynamics of photoinduced antiferromagnet– paramagnet phase transition in $FeBO_3$ was studied using ultrafast magneto-optical spectroscopy. Contrary to the previously studied metallic nickel and semimetallic strontium molybdate, the photoexcitation of iron borate does not result in the heating of the electron subsystem, but leads to an increase in the phonon temperature as a result of the most intense electron–phonon transitions. The photoinduced destruction of the magnetic order is caused by the increase in magnon temperature as a result of energy exchange with the photoexcited phonon subsystem, and the phase transition rate is limited by the phonon–magnon relaxation rate. Analysis of the temperature dependences has shown that the subpicosecond dynamics of the magneto-optical effect is not associated with the destruction of magnetic order but is caused by the transitions of Fe^{3+} ions to the excited low-spin state S = 3/2 and the recombination into the ground high-spin state S = 5/2 in a time shorter than 100 fs.

We are grateful to V.N. Gridnev, V.V. Pavlov, F. Bentivegna, A. van Etteger, and H.J. Weber for helpful discussions. This work was supported by the Russian Foundation for Basic Research and the programs of the Ministry of Industry and Science.

REFERENCES

1. J. Shah, *Ultrafast Spectroscopy of Semiconductors and Semiconductor Nanostructures* (Springer-Verlag, Berlin, 1996).
2. M. B. Agranat, S. I. Ashitkov, A. B. Granovskiĭ, and G. I. Rukman, Zh. Éksp. Teor. Fiz. **86**, 1376 (1984) [Sov. Phys. JETP **59**, 804 (1984)].
3. E. Beaurepaire, J.-C. Merle, A. Daunois, and J.-Y. Bigot, Phys. Rev. Lett. **76**, 4250 (1996).
4. J. Hohlfeld, E. Matthias, R. Knorren, and K. H. Bennemann, Phys. Rev. Lett. **78**, 4861 (1997).
5. T. Kise, T. Ogasawara, M. Ashida, *et al.*, Phys. Rev. Lett. **85**, 1986 (2000).
6. W. Hübner and C. P. Zhang, Phys. Rev. B **58**, R5920 (1998).
7. M. B. Agranat, S. I. Anisimov, S. I. Ashitkov, *et al.*, Pis'ma Zh. Éksp. Teor. Fiz. **67**, 904 (1998) [JETP Lett. **67**, 953 (1998)].
8. B. Koopmans, M. van Kampen, J. T. Kohlhepp, and W. J. M. de Jonge, Phys. Rev. Lett. **85**, 844 (2000).
9. O. Ney, M. Trzeciecki, and W. Hübner, Appl. Phys. B (2002) (in press).
10. *Landolt-Börnstein: Numerical Data and Functional Relationships in Science and Technology, New Series* (Springer-Verlag, Berlin, 1981), Group III, Vol. 16a.
11. J. Frey, R. Frey, and C. Flytzanis, Phys. Rev. B **45**, 4056 (1992).
12. S. B. Borisov, I. L. Lyubchanskiĭ, A. D. Petrenko, and G. I. Trush, Zh. Éksp. Teor. Fiz. **105**, 524 (1994) [JETP **78**, 279 (1994)].
13. V. V. Eremenko, *Introduction to Optical Spectroscopy of Magnetics* (Naukova Dumka, Kiev, 1997).
14. O. S. Kolotov, A. P. Krasnozhon, and V. A. Pogozhev, Fiz. Tverd. Tela (St. Petersburg) **40**, 305 (1998) [Phys. Solid State **40**, 277 (1998)].

Translated by V. Sakun

JETP Letters, Vol. 75, No. 9, 2002, pp. 492–494. Translated from Pis'ma v Zhurnal Éksperimental'noĭ i Teoreticheskoĭ Fiziki, Vol. 75, No. 9, 2002, pp. 584–587.

Self-Formation of Quantum Wire Networks in Porous InGaAs/GaAs Superlattices

L. K. Orlov* and N. L. Ivina

Institute of Physics of Microstructures, Russian Academy of Sciences, Nizhni Novgorod, 603950 Russia

** e-mail: orlov@ipm.sci-nnov.ru*

Received April 8, 2002

The structures containing networks of one-dimensional quantum wires were obtained through self-formation in the course of electrochemical etching of multilayer heteroepitaxial structures with a two-dimensional charge-carrier gas in InGaAs layers. The fact that the dimensionality of the electron–hole subsystem is reduced and the charge-carrier energy spectrum transforms from two-dimensional to quasi-one-dimensional was demonstrated by the shift and narrowing of resonance lines in the photoluminescence spectrum. © *2002 MAIK "Nauka/Interperiodica".*

PACS numbers: 81.07.Vb; 68.65.Cd; 78.55.Cr

In recent years, interest has been shown in porous systems which can be used as matrices for the formation of new objects with reduced dimensionality [1]. One such idea is aimed at the formation of quantum wire networks through filling the voids in a porous dielectric matrix with a substance of different chemical composition having either a metallic (Bi [2]) or semiconducting (PbTe [1]) type of conduction. It has recently been suggested that the starting matrices may be fabricated not only from dielectric materials but also from porous undoped semiconductor materials, which are most often used in micro- and nanoelectronic devices. Since the dielectric properties of a skeletal matrix forming wire network play a crucial role in the transport phenomena, preference in choosing the matrix for experiment will, probably, be given to broad-gap semiconductors of the Si, GaAs, and InP type. However, attempts at the practical implementation of this idea face problems caused by considerable difficulties associated with the growth, inside the pores of the initial crystal, of conducting semiconductor wires with perfect crystal structure and, correspondingly, high-quality electric characteristics. The interpretation of the measurement results also offers problems because of the necessity of taking into account the influence of charged states at the well-developed surface of the porous structure on the characteristics of filling material.

In this work, we discuss an alternative method of fabricating quantum wire networks. The method is based on wire self-formation in the course of electrolytic etching of multilayer heteroepitaxial structures containing nanometer-thick layers with a two-dimensional electron gas. Heteroepitaxial multilayer quantum structures GaAs/InGaAs grown in the (100) plane and studied in detail in [3] were chosen as the starting crystal matrix. Electrolytic etching of this structure mainly goes on along the inclined planes of the {111} type [4] to form, at their intersections with the InGaAs layers, the network of wires with a high-mobility electron gas, whose dimensionality depends on the width of intersecting planes. Evidently, for certain etching regimes and rates, one can obtain networks of quasi-one-dimensional InGaAs quantum wires in the bulk of the GaAs matrix. The study of such structures is of interest because of the specific optical and transport properties [5] of the objects under discussion. At the same time, the method of testing the fabricated structures is quite important, because there must eventually be no question that the etching process results in the structure containing one-dimensional quantum conductors (may be, of a rather complex configuration).

The changes in the optical and, in particular, photoluminescence spectra and their analysis can serve as a configuration-independent criterion for the formation of a system of quantum wires in the plane of a two-dimensional InGaAs layer. This criterion was successfully applied in testing other low-dimensional objects. A luminescence line due to the recombination of two-dimensional charge carriers in the layers of the semiconductor structure is clearly seen at liquid nitrogen temperature. A change in its position and width can be used to trace the possible transformation of the electron spectrum upon reducing the dimensionality of the system during the course of electrochemical etching.

A periodic $In_xGa_{1-x}As/GaAs$ structure grown by MOCVD and containing double quantum wells of total thickness $d_1 = 2d_{qw} + d_b = (2 \times 5 + 5)$ nm in the $In_xGa_{1-x}As$ layers with an indium content (x) of about 25 at. % was chosen as a starting sample for investigation. The double quantum wells in the GaAs matrix were approximately 0.07 μm apart. The superlattice

contained a total of ten periods and had the electronic type of conduction. The initial photoluminescence spectrum of the quantum-sized InGaAs layers excited at temperature $T = 77$ K by a helium–neon laser is shown in Fig. 1 (curve *1*). The subsequent procedure of generating inclined planes, whose intersections with the planes of InGaAs layers should form a system of conducting quantum wires, consisted of the standard electrochemical etching in a solution of hydrofluoric acid and ethylene at current densities of 20–40 mA/cm^2 under UV illumination. Evidently, the pores develop progressively during the course of etching, so that the cross partitions become more and more thinner. This should be accompanied by the transformation of the electron spectrum and, in particular, by the reduction of its dimensionality because of the additional spatial confinement of two-dimensional electrons and holes in the (100) plane. In the photoluminescence spectra, the transition from a two-dimensional to an one-dimensional system must be accompanied by the corresponding transformation of the spectral lines. First of all, one should expect that the emission line will undergo a high-energy shift and its width will decrease because of an increase in the density of electronic states in the energy bands.

Typical spectral curves recorded before and after etching the sample for 60 min are presented in Fig. 1, where the above-mentioned transformations of the photoluminescence line are quite pronounced. The emission peak from the two-dimensional InGaAs layers undergoes a sizable shift to the short-wavelength region of the spectrum. The dependence of the line shift on the etching time is shown in Fig. 2a. Assuming that the wire cross-section is rectangular and using the simplest formula for the electron (hole) energy spectrum in the wire $E(n, k, p_z) = E_{g0} + p_z^2/2m_{e(h)} + \{\pi^2\hbar^2/2m_{e(h)}\}\{(n + 1/2)d_1^2 + (k + 1/2)d_2^2\}$, one obtains the following expression for the additional line shift caused by the additional spatial constraint (d_2) introduced in the (100) plane by etching: $\Delta E = \Delta E_e + \Delta E_h = \pi^2\hbar^2/2\,d_2^2\,(1/m_e + 1/m_h)$, where $m_{e(h)} = 0.06(0.4)m_0$ is the effective electron(hole) mass. The line shift $\Delta E \approx 30$ meV corresponds to the wire width $d_2 \approx 15$ nm.

The etching of a sample with strained InGaAs layers can, in principle, relieve a portion of elastic energy accumulated in the sample, thereby shifting the luminescence line to the long-wavelength region of the spectrum and, hence, slightly underestimating the wire width. However, X-ray diffraction measurements before and after the etching suggest that the elastic strain accumulated in the sample remains virtually unchanged; i.e., the layer deformation in the single crystal and in the porous structure remains at approximately the same level and has virtually the same effect on the characteristics of the electron energy spectrum in both systems.

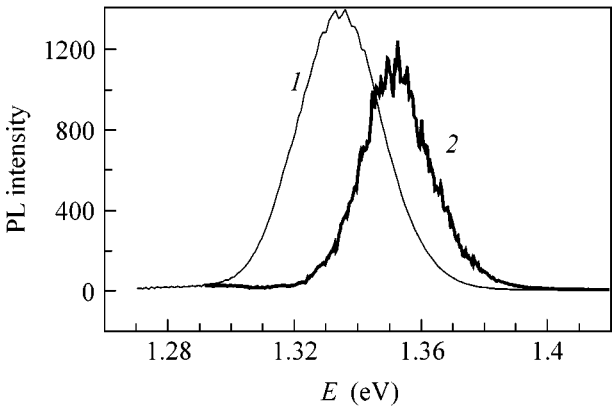

Fig. 1. Photoluminescence spectra recorded for the initial CP InGaAs/GaAs sample at $T = 77$ K (*1*) before and (*2*) after etching for 60 min.

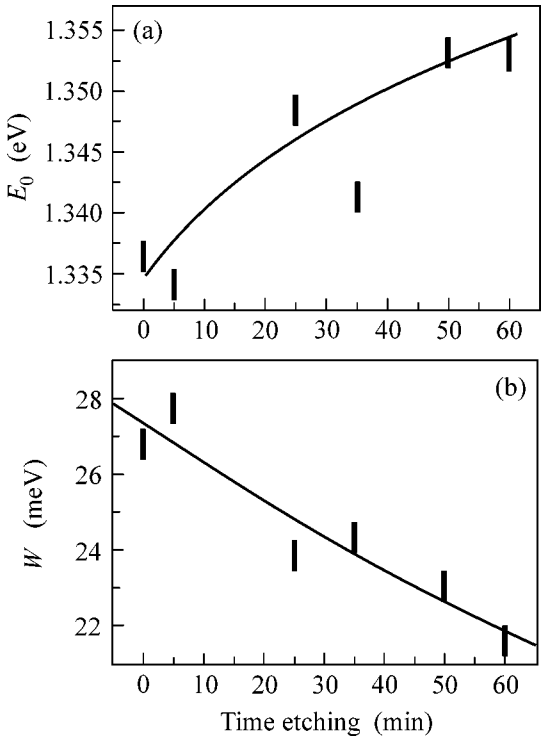

Fig. 2. (a) Position E_0 of the photoluminescence line maximum and (a) FWHM W of the line as functions of etching time.

The reduction of the dimensionality of the charge-carrier spectrum in a semiconductor and, in particular, the transition from a two-dimensional to a quasi-one-dimensional system should alter the density of energy states. In the structure with a two-dimensional electron gas, the energy dependence of the density of states is given by the expression $\rho(E) \sim (E - E_n)^{1/2}$. As the dimensionality of the electron spectrum is reduced by unity during the formation of the quantum wire net-

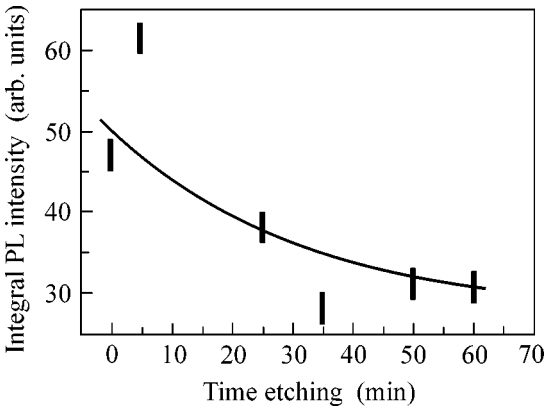

Fig. 3. Integrated photoluminescence line intensity vs. etching time.

work in the layers, the energy dependence of the density of states acquires the one-dimensional character and becomes steeper, namely, $\rho(E) \sim (E - E_{nk})^{-1/2}$. Here, E_n and E_{nk} are the subband edges in the quantum layer and quantum wire, respectively. The increase in the density of states near the band edges should bring about narrowing of luminescence lines, on the one hand, and an increase in the emission intensity, on the other, as is the case with quantum dots.

The line FWHM as a function of etching time is presented for the structure under study in Fig. 2b. It is worthy of note that a rather broad (~27 meV) initial resonance line *1* in Fig. 1 is Gaussian with a high accuracy. This suggests that the line width is caused not by the electronic processes but solely by the scatter of structure parameters (e.g., thickness of quantum well within one or several periods of the superlattice). The electrochemical etching of the sample and the formation of pores (generally, of various diameter) should enhance thickness inhomogeneity for the nanoobjects formed. This, in turn, should inevitably bring about additional broadening of the spectral lines. However, when etching the sample, we observed a monotonic decrease in the line width from 27 to 21 meV. This fact indicates that the influence of the additional spatial confinement caused by the formation of intersecting quantum wires in the sample is more pronounced than the influence of inhomogeneities that also appear upon etching.

The integrated photoluminescence line intensity as a function of etching time is shown in Fig. 3. The behavior of this curve is determined by two factors. On the one hand, the etching-induced deterioration of the surface mirror characteristics should depress the reflected laser signal and, as a result, enhance the fraction of absorbed power in the sample, thereby increasing the photoluminescence intensity [4]. On the other hand, a decrease in the volume of the active light-emitting layer because of its etching should reduce the emission intensity, as was observed in our case (Fig. 3).

In summary, the study of the photoluminescence spectra of the electrochemically etched multilayer heteroepitaxial InGaAs/GaAs structures with quantum wells has demonstrated that a network of quasi-one-dimensional conducting objects with the properties of quantum wires can arise through self-formation in the planes of InGaAs layers.

We are grateful to N.A. Alyabina for assistance in preparing samples, B.N. Zvonkov for providing us with the structures, and Prof. E.S. Dmidov (NNGU) for discussions. This work was supported by the Russian Foundation for Basic Research (project nos. 01-02-16778, 01-02-06232, 02-02-06577) and the Scientific and Technical Program “Physics of Solid-State Nanostructures.”

REFERENCES

1. V. N. Bogomolov, A. I. Zadorozhnyĭ, T. M. Pavlova, *et al.*, Pis’ma Zh. Éksp. Teor. Fiz. **31**, 406 (1980) [JETP Lett. **31**, 378 (1980)].
2. A. D. Grozaw and N. I. Leporda, Fiz. Tverd. Tela (St. Petersburg) **38**, 1924 (1996) [Phys. Solid State **38**, 1063 (1996)].
3. L. K. Orlov, N. L. Ivina, R. A. Rubtsova, *et al.*, Fiz. Tverd. Tela (St. Petersburg) **42**, 537 (2000) [Phys. Solid State **42**, 548 (2000)].
4. Yu. N. Buzynin, S. A. Gusev, Yu. N. Drozdov, *et al.*, Poverkhnost, No. 5, 40 (1996).
5. J. Voit, Rep. Prog. Phys. **58**, 977 (1995).

Translated by V. Sakun